2015

Simulation of a Regenerative Electromagnetic Vehicle Suspension

Fabio Tarantini
University of Windsor

Simulation of a Regenerative Electromagnetic Vehicle Suspension

By

Fabio Tarantini

A Thesis
Submitted to the Faculty of Graduate Studies
through the Department of Mechanical, Automotive and Materials Engineering
in Partial Fulfillment of the Requirements for
the Degree of Master of Applied Science
at the University of Windsor

Windsor, Ontario, Canada

2015

Simulation of a Regenerative Electromagnetic Vehicle Suspension

by

Fabio Tarantini

APPROVED BY:

_____

Narayan Kar
Department of Electrical & Computer Engineering

_____

Vesselin Stoilov
Department of Mechanical, Automotive & Materials Engineering

_____

Bruce Minaker, Advisor
Department of Mechanical, Automotive & Materials Engineering

August 14, 2015

DECLARATION OF ORIGINALITY

I hereby certify that I am the sole author of this thesis and that no part of this thesis has been published or submitted for publication.

I certify that, to the best of my knowledge, my thesis does not infringe upon anyone's copyright nor violate any proprietary rights and that any ideas, techniques, quotations, or any other material from the work of other people included in my thesis, published or otherwise, are fully acknowledged in accordance with the standard referencing practices. Furthermore, to the extent that I have included copyrighted material that surpasses the bounds of fair dealing within the meaning of the Canada Copyright Act, I certify that I have obtained a written permission from the copyright owner(s) to include such material(s) in my thesis and have included copies of such copyright clearances to my appendix.

I declare that this is a true copy of my thesis, including any final revisions, as approved by my thesis committee and the Graduate Studies office, and that this thesis has not been submitted for a higher degree to any other University or Institution.

ABSTRACT

In the last two decades, legislation that regulates carbon dioxide emissions are getting more and more stringent. In order to meet these regulations, fuel efficiency must be increased. This can be possible using devices that recover otherwise wasted energy. In this study, an electromagnetic regenerative shock absorber is analyzed. The device is capable of converting the vibrational energy, usually wasted as heat in conventional dampers, into electrical energy.

The objective of this work is to develop a Matlab® model of the system in order to evaluate the gain in terms of harvested energy. The dynamic performance of the selected regenerative shock absorber integrated in the suspension system is evaluated. This includes an investigation of the ride filtering capability of the apparatus in order to highlight the behaviour in terms of comfort and handling. The influence of road roughness and vehicle speed on the aforementioned outcomes are investigated.

DEDICATION

To my parents and my brother

ACKNOWLEDGEMENTS

This project is the result of a two year Double Degree Master program made possible only with the collaboration and organizational efforts of two universities, University of Windsor and Politecnico di Torino, and a prestigious industrial partner such as Fiat Chrysler Automobiles.

Therefore I would like to express my sincere appreciation to the persons who represent the aforementioned institutions and played a fundamental role in coordinating this ambitious program, Dr. Andrzej Sobiesiak from University of Windsor, Prof. Giovanni Belingardi from Politecnico di Torino, Edoardo Rabino from FCA Italy, and Mohammed Malik and Ishika Towfic from FCA Canada.

I would like to express my deepest gratitude to my academic advisor at the University of Windsor, Dr. Bruce Minaker, who has supervised my activities closely and supported me throughout the project.

I further want to thank my advisors from Politecnico di Torino, Prof. Nicola Amati and Prof. Andrea Tonoli, together with my industrial advisors, Patrizio Turco and Michele Ieluzzi from Centro Ricerche Fiat, and Jonathan Rener from Chrysler Technical Center, for their support and suggestions.

I am profoundly thankful to my older brother and my parents who always supported and encouraged me throughout my studies. Their words and their actions are always the greatest teaching.

Special thanks go to my girlfriend Elisa, for her patience and strength in supporting me despite my choices that severely tested our relationship.

Finally, I would like to thank my friends who shared this experience with me, Sergio, Biagio, Francesco, and Ivan, for the contribution that each of them added to this great year: optimism, wisdom, delicious meals, and “Nashville experience”.

TABLE OF CONTENTS

DECLARATION OF ORIGINALITY iii

ABSTRACT iv

DEDICATION v

ACKNOWLEDGEMENTS vi

LIST OF TABLES x

LIST OF FIGURES xi

LIST OF APPENDICES xvii

LIST OF ABBREVIATIONS xviii

NOMENCLATURE xx

1 INTRODUCTION 1

1.1 Objectives 3

1.2 Methodology 4

1.3 Thesis organization 4

2 LITERATURE REVIEW 6

2.1 Conventional shock absorbers 6

2.1.1 Double tube shock absorber 6

2.1.2 Mono tube shock absorber 8

2.1.3 Comparison between double and mono tube shock absorbers 8

2.1.4 Force-speed characteristic of conventional shock absorbers 9

2.2 Regenerative shock absorbers 10

2.2.1 Regenerative shock absorbers classification 11

2.2.2 Linear type shock absorber 12

2.2.3 Rotary type shock absorber 15

2.3 Basic principles of magnetic circuits 28
2.3.1 Flux $\boldsymbol{\phi}$ 28
2.3.2 Flux linkage 29
2.3.3 Magnetic structures with air gaps 30
2.3.4 Inductances 31
2.3.5 Faraday's Law....32
2.3.6 Permanent Magnets....33
2.4 Basic principles of electromechanical energy conversion 35
2.4.1 Basic structure....35
2.4.2 Basic principles of operation 36
2.4.3 Application of the basic principles: eddy current dampers....37
3 MODEL DESCRIPTION....41
3.1 Suspension description....41
3.1.1 Shock absorber description....43
3.1.2 Block diagram of the integrated model....44
3.2 Random road profiles generation 45
3.3 EoM....51
3.3.1 EoM input file....52
3.4 Electromagnetic damper....53
3.4.1 Electric charging circuit....56
3.4.2 Efficiencies and harvested power calculation....57
3.5 CO_2 saving evaluation....58
3.6 Road handling evaluation....59
3.7 Ride comfort evaluation....61
4 SIMULATION RESULTS AND DISCUSSION....63

4.1 Medium passenger car application 64
4.1.1 Input parameters 64
4.1.2 Equivalent resistance selection 65
4.1.3 Main parameter behaviour for fixed vehicle speed and road class 66
4.1.4 Road handling index 70
4.1.5 Ride comfort 73
4.1.6 Conversion efficiency, harvested power and CO_2 saving 77
4.2 SUV application 81
4.2.1 Road handling index 81
4.2.2 Ride comfort 82
4.2.3 Conversion efficiency, harvested power and CO_2 saving 83
5 CONCLUSIONS AND RECOMMENDATIONS 86
5.1 Conclusions 86
5.2 Recommendations 87
6 APPENDICES 88
6.1 Appendix A 88
6.1.1 EoM input file 88
6.2 Appendix B 95
6.2.1 Road handling index and ride comfort 95
REFERENCES 99
VITA AUCTORIS 103

LIST OF TABLES

Table 1.1-1: List of the values considered for the rough estimation of the energy dissipated in a conventional shock absorber 2
Table 2.3-1: Parameters of permanent magnet materials [21] 34
Table 3.2-1: ISO 8608 values of $G_d(n_0)$ and $G_d(\Omega_0)$ (n_0=0.1 cycles/m and Ω_0=1 rad/m) [29] 47
Table 3.2-2: k values for ISO 8608 road roughness classification [29] 50
Table 3.5-1: Values of the "consumption of effective power" $\boldsymbol{VPe}$ for different types of engine [38] 59
Table 3.5-2: Values of the conversion factor CF for petrol and diesel-type fuel [38] 59
Table 4.1-1: Values of the parameters used for the quarter car model 64
Table 4.1-2: List of the main parameters of the electromagnetic damper used in the simulations 64
Table 4.1-3: Harvested power, total efficiency, and CO_2 saving (vehicle speed 36 km/h, road class C-D) 69
Table 4.1-4: CO_2 savings for a gasoline engine equipped vehicle for the four classes considered 80
Table 4.1-5: CO_2 savings for a gasoline turbocharged engine equipped vehicle for the four classes considered 80
Table 4.1-6: CO_2 savings for a diesel engine equipped vehicle for the four classes considered 80
Table 4.2-1: Parameters used for the quarter car model for the SUV application 81
Table 4.2-2: CO_2 savings for a gasoline engine equipped vehicle for the four classes considered 85
Table 4.2-3: CO_2 savings for a gasoline turbocharged engine equipped vehicle for the four classes considered 85
Table 4.2-4: CO_2 savings for a diesel engine equipped vehicle for the four classes considered 85

LIST OF FIGURES

Figure 1.1-1: Rough estimate of the power dissipated by 4 conventional shock absorbers and potentially harvestable for 4 road profiles (according to the ISO 8608 Standard classification) 1
Figure 2.1-1: Hydraulic scheme of a double tube (left) and a mono tube (right) shock absorber [3] 7
Figure 2.1-2: Damping force-stroke diagram and damping force-speed diagram: a) progressive, b) linear, c) degressive [5] 9
Figure 2.2-1: Quarter-car model with viscous damper (left) and quarter-car model with electromagnetic harvester (right) [1] 11
Figure 2.2-2: Diagram of the electric shock absorber: A-A-axial (longitudinal) cross-section, B-B-perpendicular cross-section [4] 13
Figure 2.2-3: (a) Diagram of the linear electromagnetic shock absorber and (b) the cross section of the magnet assembly [8] 14
Figure 2.2-4: System layout of the pumping regenerative suspension [14] 16
Figure 2.2-5: The energy recovery unit dynamics model [14] 17
Figure 2.2-6: Overall structure of an integrated hydraulic actuator [14] 17
Figure 2.2-7: Force-displacement loops with different rod diameters (External load=15 Ohm, Input frequency=1.67 Hz, Displacement amplitude=50 mm) [14] .. 18
Figure 2.2-8: Force-velocity relationships with different electrical loads (Input frequency=1.67 Hz, displacement amplitude=50 mm) [14] 19
Figure 2.2-9: Hydraulic efficiency with different loads (input frequency=1.67 Hz, displacement amplitude=50 mm) and different frequencies (external load=15 Ω, displacement amplitude=50 mm) [14] 20
Figure 2.2-10: Overall structure of the rack-pinion-based regenerative shock absorber [16] 20
Figure 2.2-11: Dynamic modeling of the electromagnetic generator, where Re can be the equivalent resistance of the power charge circuit [16] 21
Figure 2.2-12: Control circuit for asymmetric characteristics [16] 23

Figure 2.2-13: Ball screw mechanism: rotating screw (left), rotating nut (right) [9] 23
Figure 2.2-14: Principle of motion rectifier for oscillating motion [17].....25
Figure 2.2-15: 3D model of the mechanical motion rectifier [17].....25
Figure 2.2-16: Damping loops for different external electrical loads under vibration input of 1.5 Hz and 5 mm amplitude [17].....26
Figure 2.2-17: Damping loops for different input frequencies with electrical load 106.6 Ω [17].....27
Figure 2.3-1: Toroid with flux Φ_m [20].....29
Figure 2.3-2: Simple magnetic structure with air gap [20].....30
Figure 2.3-3: Coil inductance [20].....31
Figure 2.3-4: Voltage polarity and direction of flux and current [20].....32
Figure 2.3-5: Normal and intrinsic hysteresis loops of a permanent magnet material [21].....33
Figure 2.3-6: Demagnetization curves for different permanent magnet materials [22].....34
Figure 2.4-1: Cross-section of the electric motor seen from one side [20].....35
Figure 2.4-2: Structure of a 2-pole (left) and 4-pole (right) machine [20] 36
Figure 2.4-3: Conductor moving in a magnetic field [20].....37
Figure 2.4-4: Sketch of a torsional damper (or an induction machine) [24].....38
Figure 3.1-1: Double wishbone suspension example [3].....41
Figure 3.1-2: Double wishbone suspension model in EoM.....42
Figure 3.1-3: Block diagram of the integrated model.....44
Figure 3.2-1: Random road profiles of 1km for four classes according to ISO 8608 classification 50
Figure 3.2-2: Random road profiles of 1km for three classes according to ISO 8608 classification 51
Figure 3.4-1: Dynamics modeling of the electromagnetic motor; *Re* is the equivalent resistance of the power charge circuit [16] 53
Figure 3.4-2: Schematization of the electric charging circuit [34] 56
Figure 3.4-3: Schematic of a buck-boost converter [35] 56

Figure 4.1-1: Force-to-speed characteristic of the electromagnetic damper for different values of equivalent resistance 65
Figure 4.1-2: Electrical efficiency as a function of equivalent resistance (vehicle speed=36 k/h, road roughness class=CD) 66
Figure 4.1-3: Random road profile of a C-D class of roughness 67
Figure 4.1-4: Relative velocity between the two ends of the shock absorber 67
Figure 4.1-5: Current induced into the generator coil 68
Figure 4.1-6: Dynamic tire/ground contact force [N] 68
Figure 4.1-7: Sprung mass weighted acceleration [m/s^2] 69
Figure 4.1-8: Output electrical energy over the equivalent resistance as a function of time 70
Figure 4.1-9: Road handling index as a function of vehicle speed for four classes of road roughness 71
Figure 4.1-10: Road handling index as a function of vehicle speed for A-B class road: comparison between the values obtained with the electromagnetic damper and a conventional one (1800 Ns/m) 71
Figure 4.1-11: Road handling index as a function of vehicle speed for B-C class road: comparison between the values obtained with the electromagnetic damper and a conventional one (1800 Ns/m) 72
Figure 4.1-12: Road handling index as a function of vehicle speed for C-D class road: comparison between the values obtained with the electromagnetic damper and a conventional one (1800 Ns/m) 73
Figure 4.1-13: Road handling index as a function of vehicle speed for D-E class road: comparison between the values obtained with the electromagnetic damper and a conventional one (1800 Ns/m) 73
Figure 4.1-14: Sprung masses weighted acceleration as a function of vehicle speed for four classes of road roughness 74
Figure 4.1-15: Sprung mass acceleration expressed in g units as a function of vehicle speed for four classes of road roughness 74

Figure 4.1-16: Sprung masses weighted acceleration as a function of vehicle speed for A-B class road: comparison between the values obtained with the electromagnetic damper and a conventional one (1800 Ns/m).....75
Figure 4.1-17: Sprung masses weighted acceleration as a function of vehicle speed for B-C class road: comparison between the values obtained with the electromagnetic damper and a conventional one (1800 Ns/m).....75
Figure 4.1-18: Sprung masses weighted acceleration as a function of vehicle speed for C-D class road: comparison between the values obtained with the electromagnetic damper and a conventional one (1800 Ns/m).....76
Figure 4.1-19: Sprung masses weighted acceleration as a function of vehicle speed for D-E class road: comparison between the values obtained with the electromagnetic damper and a conventional one (1800 Ns/m).....77
Figure 4.1-20: Total conversion efficiency as a function of vehicle speed for four classes of road roughness.....78
Figure 4.1-21: Harvested power as a function of vehicle speed for four classes of road roughness 78
Figure 4.1-22: CO_2 savings as a function of vehicle speed for the four classes considered for a gasoline turbocharged engine (four shock absorbers).....79
Figure 4.2-1: Road handling index as a function of vehicle speed for four classes of road roughness 82
Figure 4.2-2: Sprung masses weighted acceleration as a function of vehicle speed for four classes of road roughness 83
Figure 4.2-3: Sprung mass acceleration expressed in g units as a function of vehicle speed for four classes of road roughness 83
Figure 4.2-4: Total conversion efficiency as a function of vehicle speed for four classes of road roughness.....84
Figure 4.2-5: Harvested power as a function of vehicle speed for four classes of road roughness 84
Figure 6.1-1: Example of the definition of a ‘body’ type item: chassis 89
Figure 6.1-2: Definition of the ‘spring’ type item 90

Figure 6.1-3: Examples of the definition of ‘rigid_point’ type item: wheel bearing 91
Figure 6.1-4: Example of the definition of ‘flex_point’ type item: tire.....91
Figure 6.1-5: Example of the definition of ‘actuator’ type item: wheel actuator 92
Figure 6.1-6: Example of the definition of ‘sensor’ type item: body sensor 93
Figure 6.1-7: Definition of the sensor to measure the dynamic force between the tire and the ground 93
Figure 6.1-8: Complete model of the suspension in EoM 94
Figure 6.2-1: Road handling index as a function of vehicle speed for A-B class road: comparison between the values obtained with the electromagnetic damper and a conventional one (5000 Ns/m).....95
Figure 6.2-2: Road handling index as a function of vehicle speed for B-C class road: comparison between the values obtained with the electromagnetic damper and a conventional one (5000 Ns/m).....95
Figure 6.2-3: Road handling index as a function of vehicle speed for C-D class road: comparison between the values obtained with the electromagnetic damper and a conventional one (5000 Ns/m).....96
Figure 6.2-4: Road handling index as a function of vehicle speed for D-E class road: comparison between the values obtained with the electromagnetic damper and a conventional one (5000 Ns/m).....96
Figure 6.2-5: Sprung masses weighted acceleration as a function of vehicle speed for A-B class road: comparison between the values obtained with the electromagnetic damper and a conventional one (5000 Ns/m).....97
Figure 6.2-6: Sprung masses weighted acceleration as a function of vehicle speed for B-C class road: comparison between the values obtained with the electromagnetic damper and a conventional one (5000 Ns/m).....97
Figure 6.2-7: Sprung masses weighted acceleration as a function of vehicle speed for C-D class road: comparison between the values obtained with the electromagnetic damper and a conventional one (5000 Ns/m).....98

Figure 6.2-8: Sprung masses weighted acceleration as a function of vehicle speed for D-E class road: comparison between the values obtained with the electromagnetic damper and a conventional one (5000 Ns/m).....98

LIST OF APPENDICES

Appendix A ……. 88
Appendix B ……..…... 95

LIST OF ABBREVIATIONS

Abbreviations

3D	Three dimensional
AC	Alternating Current
CAD	Computer-Aided Design
CF	Conversion Factor
CO_2	Carbon dioxide
DC	Direct Current
DCM	Discontinuous Current Mode
emf	Electromotive force
EM	Electromagnetic
EoM	Equations of Motion
FCA	Fiat Chrysler Automobiles
g	Gravitational Acceleration
gCO_2	Grams of carbon dioxide
H	Henry
h	Hour
Hz	Hertz
ISO	International Organization for Standardization
J	Joule
kg	Kilogram
l	Liter
m	Meter
MMR	Mechanical Motion Rectifier
mph	Miles per Hour
N	Newton
ODE	Ordinary Differential Equation
PM	Permanent Magnet
PSD	Power Spectral Density
PWM	Pulse Width Modulation
QCM	Quarter Car Model
rad	Radian
rev	Revolution
RHI	Road Handling Index

RMS	Root Mean Square
rpm	Revolutions Per Minute
s	Second
SUV	Sport Utility Vehicle
V	Volt
W	Watt

NOMENCLATURE

Symbols

A_g	Air gap area
A_i	Amplitude of the harmonic function
a_{RMS}	RMS of the accelerations
B	Flux density
B_r	Remanent magnetic flux density
C_{eq}	Equivalent damping coefficient
d	Diameter of the coil
E_{diodes}	Energy dissipated by the diodes
Emech	Mechanical energy
E_{Re}	Energy on the external resistance
$F_{1,2}$	Lorentz force on the conductor of windings 1 and 2
f_q	Force on the charge
G_a	PSD of vertical accelerations
G_d	PSD of vertical displacements
H	Intensity of the magnetic field
h	Road profile vertical position
H_c	Coercive force
H_g	Intensity of the magnetic field in the air gap
i	Current
$i_{r1,2}$	Current flowing in the rotor coils 1,2
J	Moment of inertia of rotor
J_g	Rotation inertia of the gear transmission system
k	Class of road roughness
K_e	Back electromotive force constant
k_g	Transmission ratio from pinion gear to generator rotor
K_t	Torque constant
k_v	Viscous friction coefficient
l	Length of the conductor
L	Inductance
l_m	Mean path length
m	Number of phases

m_c	Mass of the moving casing
m_{eq}	Equivalent mass
m_r	Mass of the rack
m_t	Mass of translating parts
m_{tot}	Total mass of sprung and unsprung parts
N	Number of coils
n	Spatial frequency
n_0	Reference spatial frequency
p	Number of pole pairs
P_{diodes}	Power dissipated by the diodes
P_{harv}	Harvested power
P_{mech}	Mechanical power
P_{Re}	Power on the external resistance
q	Charge
$\Re$	Reluctance
R_e	External resistance
R_i	Internal resistance
S_{CO2}	CO_2 saving
T_{em}	Electromagnetic torque
v	Vehicle speed
V_{emf}	Electromotive force
$V_{Pe\text{-}D}$	Consumption of effective power (diesel engine)
$V_{Pe\text{-}P}$	Consumption of effective power (petrol engine)
$V_{Pe\text{-}PT}$	Consumption of effective power (petrol-turbo engine)
V_γ	Voltage drop
W_{max}	Maximum magnetic energy

Greek Symbols

Λ_m	Permanent magnets produced flux amplitude
η_{BS}	Ball screw efficiency
$\eta_{DC/DC}$	DC/DC converter efficiency
η_H	Hydraulic efficiency
η_{alt}	Alternator efficiency
η_{conv}	Total conversion efficiency

η_e	Electrical efficiency
η_g	Transmission efficiency
$\lambda_{r1,2}$	Total magnetic flux linked to coils 1,2
λ_{rs0}	Magnetic flux of the rotor linked to the rotor
$\lambda_{rs1,2}$	Stator magnet flux linked to coil 1,2
μ_0	Permeability of air
μ_m	Permeability of a generic material
Δx_t	Tire extra displacement due to dynamic loads
Δn	Frequency interval
τ	Ball screw transmission ratio
Ω	Angular spatial frequency
ω	Rotational velocity
Ω_0	Reference angular spatial frequency
θ	Rotation angle
λ	Flux linkage
φ	Phase angle
ϕ	Flux

1 INTRODUCTION

The reduction of the pollutant emissions into the environment is one of the biggest concerns of automotive industry. Legislation that regulates vehicles emissions are indeed becoming increasingly stringent due to the growing anxiety of governments about environmental pollution. In particular, attention is focused on carbon dioxide, mainly responsible for the greenhouse effect. As the emission of this pollutant is directly related to vehicle fuel consumption, car makers are directing their efforts toward the reduction of fuel consumption of their products. In order to do that, different strategies can be applied: reduction of engine size, increase of alternative fuels employment, reduction of the weight of vehicle components, and recovery of otherwise dissipated energy.

Looking into the latter strategy, regenerative shock absorbers appear to be a good solution to recycle the vibrational energy otherwise wasted into heat, as occurs in conventional dampers. In fact, in traditional shock absorbers the vibrational energy due to road irregularities or to vehicle roll and pitch is dissipated into heat due to the flow of fluid through small orifices. From the analysis conducted in the literature [1], three factors influence the harvestable power the most: road roughness, vehicle speed and tire stiffness. Other vehicle parameters, like spring stiffness, damping coefficient, sprung and unsprung masses have little influence on the power that can be recovered.

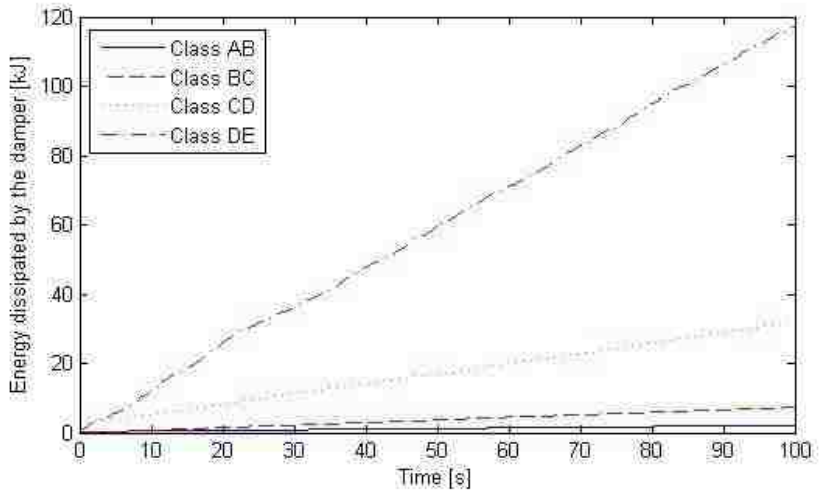

Figure 1.1-1: Rough estimate of the power dissipated by 4 conventional shock absorbers and potentially harvestable for 4 road profiles (according to the ISO 8608 Standard classification)

An estimate of the energy dissipated by four conventional dampers and potentially harvestable is plotted in Figure 1.1-1. The computation is conducted for four road profiles of increasing roughness, considering average values for a medium passenger car, reported in Table 1.1-1.

Table 1.1-1: List of the values considered for the rough estimation of the energy dissipated in a conventional shock absorber

Sprung mass	450 kg
Unsprung mass	40 kg
Spring stiffness	15000 N/m
Tire stiffness	150000 N/m
Damping coefficient	2000 Ns/m
Vehicle speed	36 km/h

The goal of regenerative suspensions is to recover the vibrational energy, converting it into electrical energy that can be used to recharge the battery. This can lead to a larger driving range, if electric vehicles are considered, or to a reduction in carbon dioxide emissions, due to the lower usage of the alternator, if conventional internal combustion engine vehicles are taken into account. Moreover, electromagnetic shock absorbers show several advantages compared to the standard hydraulic solution, for instance, small sensitivity to environmental parameters such as temperature and ageing, and larger bandwidth [2]. In addition, due to the electromagnetic nature of these devices, they allow a relatively easy implementation of active control.

Although it is a promising solution, there are still many challenges that must be faced before considering its introduction in mass production vehicles. The obstacles are mostly related to the fact that conventional shock absorbers guarantee good performance while having low cost. As regenerative shock absorbers have a higher cost when compared to traditional ones, the gain in terms of harvested power has to be sufficient to justify the on-vehicle implementation of this kind of system. Moreover, another concern that emerges from the literature is related to the weight to performance ratio of electromagnetic shock absorbers, which in most of the cases exceeds the range of acceptable values.

In order to assess the performance of the apparatus and the possible carbon dioxide emissions reduction, it is fundamental to simulate the behaviour of the device. Simulation

is a strategic action in the early design stages in order to direct the selection of the proper design strategy among the several available alternatives.

The simulation of the electromagnetic shock absorber is thus provided in this thesis. In particular, the electrical machine considered in the analysis is a rotational permanent magnet brushless motor where the linear motion of the damper is converted into rotation through a ball screw mechanism.

1.1 Objectives

The first step of the project is to provide a summary of the state of the art of the regenerative suspension technologies, giving a classification of the available solutions, highlighting advantages and disadvantages of each of them.

The main part of the project is aimed at developing a model of the regenerative electromagnetic vehicle suspension in order to evaluate the possible benefits in terms of harvested energy. The electrical energy produced by the conversion of the kinetic energy due to suspension excitement is assessed. Once it is stored in the battery of a vehicle equipped with a conventional internal combustion engine, it results in a decrease in fuel consumption. In particular the CO_2 emission reduction is evaluated.

The effects of different parameters on the harvested energy will be analyzed. Based on the eight classes of road roughness of the ISO 8608 standard, the dependence of different road profiles on the converted energy is evaluated. The recovered energy variation with respect to vehicle speed is considered.

The dynamic performance of the selected regenerative shock absorber integrated in the suspension system is evaluated. This includes the investigation of the ride filtering capability of the apparatus in order to highlight the effect of the installation of the suspension on ride comfort and road handling.

Moreover, the analysis is conducted for two types of vehicle: a medium size passenger car and a SUV. Considerations on the influence of the parameters of each vehicle on the electromagnetic shock absorber performance and thus on the recollected energy are done.

1.2 Methodology

The aforementioned model is developed using Matlab® in order to guarantee the maximum software flexibility, thus the possibility to integrate it in a global virtual vehicle model. A multi-body Quarter Car Model (QCM) is built using EoM code, an equations of motion generator for mechanical systems developed by the Vehicle Dynamics and Control Research Group at the University of Windsor. The employment of this tool combined with the use of Matlab allows the modeling of different suspension structures or energy conversion system without many difficulties.

The multi-body quarter-car linear model is integrated with the dynamic model of the regenerative damper. The model is intended to have as inputs the vehicle speed and the road profile roughness class. The latter datum is used to generate a random road profile according to the ISO 8608 Standards. The generated profile and the vehicle speed are the actual inputs of the multi-body QCM implemented using EoM. This part of the model provides as output all the data necessary for the evaluation of the ride comfort and road handling performance. In addition, relative displacement and velocity of the ends of the damper are provided in order to be the input of the dynamic model of the electromagnetic shock absorber. The damper dynamic model provides two outputs: the reaction torque that is fed back into the main multi-body QCM, and the harvested energy.

1.3 Thesis organization

The thesis is organized in the chapters listed below:

- *Chapter 2:* contains the results of the literature review performed by the author. Firstly, a summary of the state of the art of the regenerative suspension technologies is provided. A theoretical background on the electromagnetism fundamentals is given;
- *Chapter 3:* the system selected for the project is described. A detailed description of the way in which the suspension is implemented in Matlab and how the desired outputs are obtained is provided;

- *Chapter 4:* the simulations conducted for both the considered cases are explained. The inputs selected for both the application cases are shown and the results obtained are presented and discussed;
- *Chapter 5:* the conclusions and the findings of the research are outlined and summarized; some recommendations are presented.

2 LITERATURE REVIEW

2.1 Conventional shock absorbers

In order to understand the origin of the potentially harvestable energy by means of the system considered in this work, a brief introduction on traditional shock absorbers and the way in which they dissipate vibrational energy is provided in this section.

The shock absorbers used today are mostly hydraulic, thus the damping force is obtained with a piston by squeezing a certain amount of oil through small orifices controlled by valves. The flow through the orifice occurs, at a given area of the flow cross section, with a certain pressure drop that is almost proportional to the flow rate. Shock absorbers can be classified as of the structural or conventional non-structural type, according to their capacity to support loads perpendicular to the piston rod [3]. In conventional shock absorbers the only load comes from the internal pressure that loads the piston rod. Transverse forces could also be applied; they cause an increase in hysteresis and additional stress on the piston bar. This situation occurs due to the change of inclination of the shock absorber because of the stroke of the suspension.

2.1.1 Double tube shock absorber

Figure 2.1-1 shows a scheme useful to understand the operation of a hydraulic shock absorber on the left. The upper part is fixed to the sprung mass, the lower to the unsprung mass. The suspension, during its stroke, moves the piston rod 1 and the piston 2 inside the cylinder 3. The volumes marked with broken lines A, B and C are filled with oil. Due to its incompressibility, a certain flow rate of oil is squeezed by the piston motion from the chamber A to chamber B, through valves V_1 and V_2. The damping force is generated from this flow. The valves V_1 and V_2 are outlined as check valves; it is thus possible to have different a damping coefficient during the compression (valve V_1) and the extension strokes (valve V_2). The oil pressure generated by friction losses through the valves must be maintained by the seal 4 in order to avoid oil leakage, with the disadvantages that this seal causes a certain friction and suspension hysteresis.

The penetration and the extraction of the piston rod must be accompanied by the displacement of an oil volume equal to that occupied or freed by the rod. The volume C provides this function through the check valves V_3 and V_4, communicating with the volumes A and B.

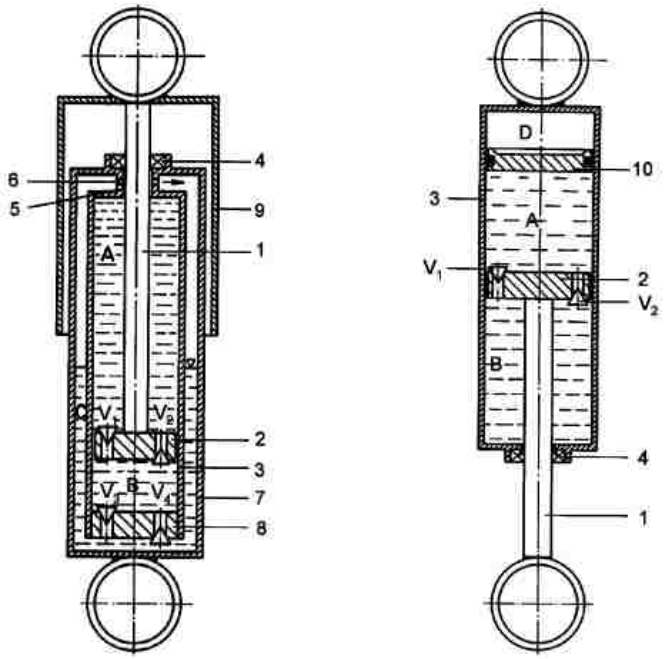

Figure 2.1-1: Hydraulic scheme of a double tube (left) and a mono tube (right) shock absorber [3]

The type of system described is also called *double tube* because of the presence of the double outside cylinder. According to this layout two chambers containing oil (inner and outer) are present. The piston with the valves assembly enters in the inner chamber, while another valves assembly divides the inner from the outer chamber.

In the lower part of the outer chamber, pressurized gas compensates for the oil volume variation created by the piston motion, avoiding cavitation near the valves, where pressure drops are present.

According to the direction of flow, valve assemblies have different functions. During the extension phase, the piston valves control the damping force, while the lower valves allow the compensatory flow between the inner and the outer chamber. On the other hand, during the compression phase, the lower valves have the damping function, while those on the piston allow an almost free flow. Some of the orifices are closed by pre-

loaded valves that open when the pressure drop exceeds a certain limit, thus limiting the damping force for high compression or extension speeds.

2.1.2 Mono tube shock absorber

The scheme on the right in Figure 2.1-1 is of a second type of shock absorber, called *mono tube*. In this kind of shock absorber, only two chambers are present, outlined as A and B in the figure. The valve assembly on piston 2, with rod 1, controls the damping force in both directions. The check valve V_1 controls the compression force, while V_2 controls the extension force. A volume of pressurized gas D is separated from the oil through the floating piston 10. The gas volume compensates for the oil volume variations due to piston rod motion. The pressure in chamber D applies a non-negligible force to the suspension, in parallel to the coil spring.

2.1.3 Comparison between double and mono tube shock absorbers

The two kind of shock absorber described have several advantages and disadvantages. The double tube shock absorbers feature the following advantages:

- Possibility to tune the ride characteristic according to the position of the piston;
- More rapid adjustment to changing road and weight condition than mono tube shock absorber;
- Control is enhanced without sacrificing driving comfort.

On the other hand, they have the disadvantages that can be only mounted in one direction.

The mono tube type shock absorbers exhibit the following advantages:

- Easy to tailor to specific application due to the fact that larger piston diameter allows low working pressures;
- Can be mounted in both orientations, for instance upside down in order to reduce the unsprung weight;
- May run cooler due to the fact that heat is dissipated directly via the outer tube that is exposed to air.

However the mono tube shock absorbers have several disadvantages:

- They are longer than the double tube shock absorbers;

- The outer tube, that acts as a guide cylinder for the piston, is susceptible to external damage [4];
- Increase of pressure on the piston rod seal, with potential leakages and increased hysteresis.

2.1.4 Force-speed characteristic of conventional shock absorbers

The performance of the shock absorbers can be described using the force-speed characteristics as showed in Figure 2.1-2. The right side characteristics show graphically how the damping force exerted on the piston of the shock absorber depends on the speed of the piston itself. The left side characteristics show the damping force developed at a particular position of the piston for the operation at a particular value of the stroke.

The damping force of a shock absorber depends on the speed at which the two fixing points are pulled or pushed together.

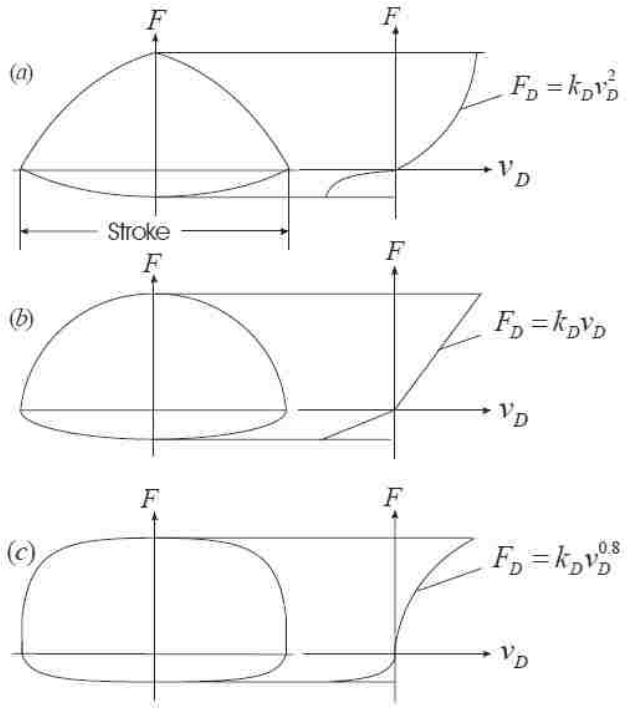

Figure 2.1-2: Damping force-stroke diagram and damping force-speed diagram: a) progressive, b) linear, c) degressive [5]

The characteristic curve of the damping force versus speed can be classified, with reference to its shape, as:

- Progressive, when the derivative of force with respect to extension or compression speed increases with speed;
- Linear, when the derivative is almost constant, but usually with different values in compression and extension;
- Degressive, when the derivative decreases with speed.

The derivative of the force with respect to speed is also called the damping coefficient. According to the Boursier De Carbon theory, a constant damping coefficient is ideal for performance. A progressive characteristic could be suitable to improve the handling quality of a high performance car, to the detriment of comfort, while a degressive one can improve comfort on rough roads, where suspension stroke speed can be high [3].
In general, the force-speed characteristics can be described by the equation:

$$F_D = k_D {v_D}^n \tag{2.1}$$

where:

- for $n > 1$ progressive curve;
- for $n = 1$ linear curve;
- for $n < 1$ degressive curve.

2.2 Regenerative shock absorbers

There are several kinds of technology by which the kinetic energy dissipated into heat in conventional shock absorber can be recovered. In this section, different types of regenerative shock absorbers, devices that convert the kinetic energy into electric one, are described.
Conventional shock absorbers are replaced in vehicle suspensions by regenerative ones in order to produce electrical energy, exploiting different principles that are mentioned in this chapter. The recovered electricity is inserted in the electric system of the vehicle in order to recharge the battery. If the system is implemented in hybrid or electric vehicles, it can lead to an increase in the driving range of the vehicles themselves. If it is installed in conventional internal combustion engine vehicles, the regenerative shock absorber decreases the usage of the alternator, thus implying a reduction in fuel consumption and therefore carbon dioxide emissions.

Regenerative shock absorbers, thanks to the fact that the damping force is produced by an electric motor that guarantees high flexibility, have the advantages that can be possibly utilized with an easy implementation in three different working modes:

- passive, where the regenerative shock absorber has a fixed damping force-relative velocity characteristics;
- semi-active, where the regenerative shock absorber has a variable damping force-relative velocity characteristics;
- active damping, where the regenerative shock absorber is used as an actuator.

The first obstacle for the spread of active suspensions in passenger cars is the high demand in terms of electrical power; the problem can be solved using regenerative shock absorbers to properly recycle and store the vibration energy in order to reduce the energy cost for active suspension control [6].

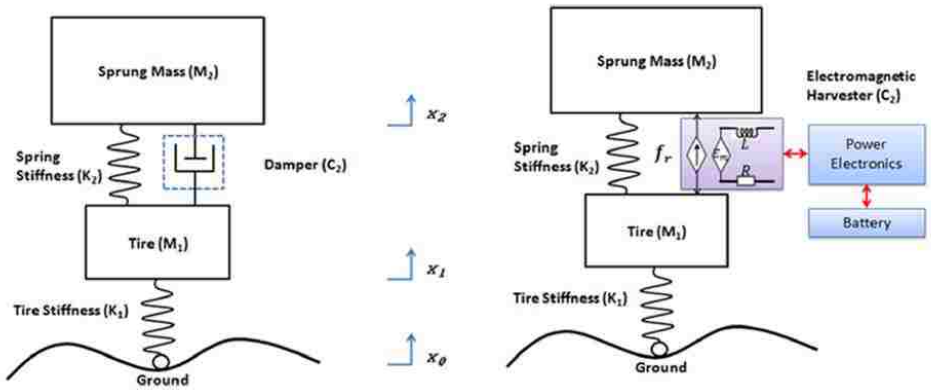

Figure 2.2-1: Quarter-car model with viscous damper (left) and quarter-car model with electromagnetic harvester (right) [1]

2.2.1 Regenerative shock absorbers classification

Many researchers explored different principles and designs of regenerative vehicle shock absorbers that can be classified, according to the type of motion used as input for the conversion, in [7]:

- Linear type shock absorber that generates the power from the relative linear motion between magnets and coils;

- Rotary type shock absorber in which the linear motion is mechanically or hydraulically transformed into rotary motion and hence, by means of an electrical machine, into electrical power.

In the second category, a further distinction can be made:

- Rotary type shock absorber directly coupled with the electrical machine (usually a reverse DC motor or an AC rectified generator);
- Rotary type shock absorber with mechanical or hydraulic motion rectification and then the electrical machine (again a reverse DC motor or an AC rectified generator).

In the former case, the electrical power is an AC type thus the output current has to be rectified with the implied power losses. In the latter configuration, the DC motor (generator) is mechanically or hydraulically forced to rotate in just one direction and the electrical rectification can be avoided due to the DC output current. It must be noted that, even for this latter case, a dedicated DC/DC converter has to be used in the conversion system in order to adapt the voltage level between the harvester output and the battery input.

2.2.2 Linear type shock absorber

In this section, the regenerative shock absorber in the configuration of a linear generator is considered. This mechanism converts the kinetic energy of suspension vibration between the wheel and the sprung mass into useful electrical power thanks to the interaction between magnets and coils in relative motion.

The shock absorber consists mainly of a magnet assembly and a coil assembly.

Paz [4] conducted a study on this type of system and the different configurations that can be implemented for vehicle suspensions. Considering the topology of the system, one of the two assemblies has to be shorter than the other in order to ensure the unchangeable active length of the machine. This implies a reduction in the efficiency of the system. Only linear generators with a short coil assembly are considered in [4] since a longer one makes the machine heavier and more costly.

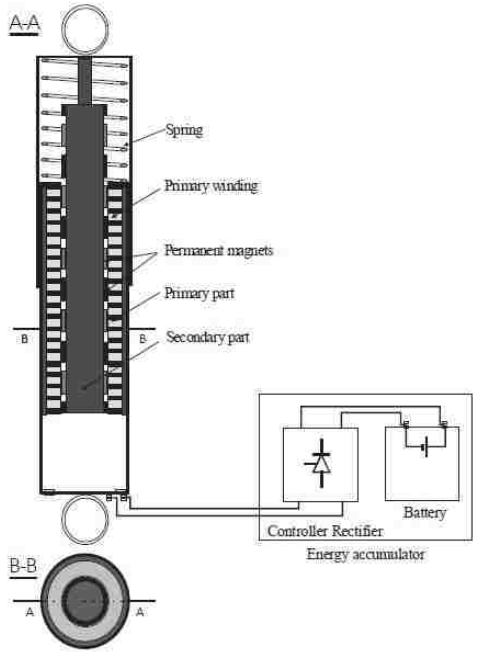

Figure 2.2-2: Diagram of the electric shock absorber: A-A-axial (longitudinal) cross-section, B-B-perpendicular cross-section [4]

The author classified the designs according to:

- Mutual position of primary (three-phase winding) and secondary (permanent magnets) part;
- Presence or absence of slots to accommodate the coils in the primary part;
- Solution used to attach the permanent magnets in the secondary part (buried or surface mounted).

The results of the study show that permanent magnets rotors are preferable with respect to wound-coil rotors and that a primary part shorter than the secondary one reduces the power loss. Among the different possible configurations, the best solution for the shock absorber seems to be a generator with a shorter external primary part, the coils placed in the slots and the secondary part with surface mounted permanent magnets, as showed in Figure 2.2-2.

The permanent magnets considered in [4] are made of neodymium-iron-boron (FeNdB).

Through the use of a Matlab-Simulink program, the system is simulated under dynamic conditions. The model considers the presence of a switch in order to connect the output terminals of the rectifier directly to the battery only if the generated voltage is higher than

the battery voltage. If it is smaller or equal to the battery voltage, the switch makes the current flow through a shunt resistor in order to obtain the correct value of damping.

The efficiency of the conversion from vibrational to electrical energy calculated for this system is around 40%.

2.2.2.1 System improvement

In order to increase the efficiency and simultaneously reduce the weight of the considered system, high magnetically permeable materials can be used in a more efficient way. In the study conducted by Zuo at al. [8], the magnet assembly considered is made of ring-shaped permanent magnets (FeNdB) and ring-shaped high magnetically permeable spacers stacked on a rod of high reluctance material (aluminum 7075). The spacers are made of 1018 steel ($\mu=875\times10^{-6}$ Hm^{-1}). The magnets are arranged with like-poles of adjacent magnets facing each other to redirect the magnetic flux in the radial direction as shown in Figure 2.2-3. In order to reduce the reluctance of the magnetic loops, thus increasing the magnetic flux density in the coils, a concentric outer cylinder of high magnetically permeable material in used (this solution increases the power density by 56%).

The mass of a full-scale regenerative shock absorber is estimated to be of 28 kg [8].

The authors conducted an analysis of the magnetic field using the finite element method in order to guide the design optimization.

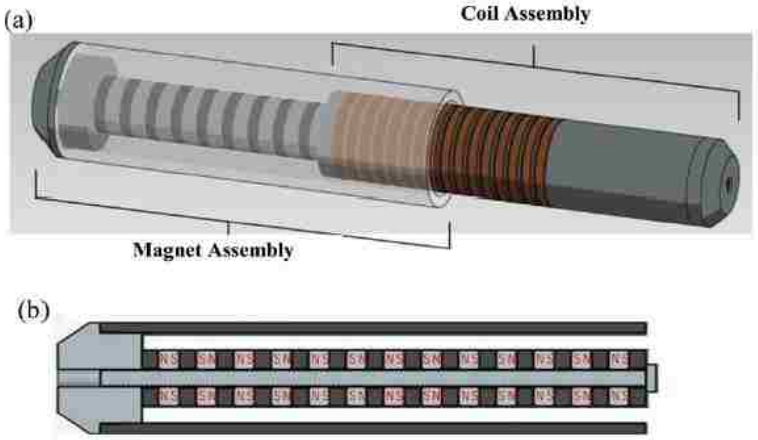

Figure 2.2-3: (a) Diagram of the linear electromagnetic shock absorber and (b) the cross section of the magnet assembly [8]

In [8], the authors created a theoretical model to analytically characterize the waveforms and the regenerated power of the harvester for different amplitudes, frequencies, equilibrium positions and design parameters.

By analyzing road driving condition of a typical highway road profiles and assuming a vehicle speed of 20 m/s (45 mph), the authors concluded that the range of vertical velocity for a shock absorber is 0.2-0.6 m/s. According to this consideration, the experiments were run at 10 Hz, which corresponds to a vertical velocity (RMS) of 0.25 m/s (thus in the correct velocity range). Therefore, the performance of a full-scale regenerative shock absorber was evaluated. The total power potentially harvestable was calculated to be 16-64 W at 0.25-0.5 m/s RMS suspension velocity. In order to calculate the actual power, the efficiency of the harvesting power electronics needs to be considered.

The research indicates that the waveform of the regenerated voltage depend on excitation frequency, amplitude and equilibrium position but does not necessarily have the same frequency as the excitation. Moreover, the voltage waveform of the individual coil depends on the equilibrium position but the total power does not depend on it. The largest value of the regenerated power is obtained at a frequency around the resonance of the vibrating system.

2.2.3 Rotary type shock absorber

In this type of shock absorber, the linear motion between the ends of the damper is converted into rotational motion of the rotor of an electrical machine using different mechanisms. They can be either mechanical or hydraulic.

The rotary solution is usually preferred according to the fact that the linear motors, although appearing to be an immediate solution for vibration damping, do not meet the requirements in terms of size and damping necessary for vehicle applications [9] [10]. Moreover, the linear electric motors are not as well studied as rotational electric motors.

According to the type of transmission chosen, the proper power electronics is implemented in order to make the output voltage suitable for charging the battery.

2.2.3.1 Hydraulic motion conversion

The system described in this section features a combined mechanical-electromagnetic-hydraulic structure that combines the flexibility of liquid with the high efficiency of electromagnetic energy-regeneration [11] [12] [13].

The considered electrohydraulic regenerative suspension can create unidirectional flow that drives the pump and thus the electric generator to produce electrical power in an efficient way. It allows the proper asymmetric compression/extension damping force ratio that is needed by traditional vehicles [14].

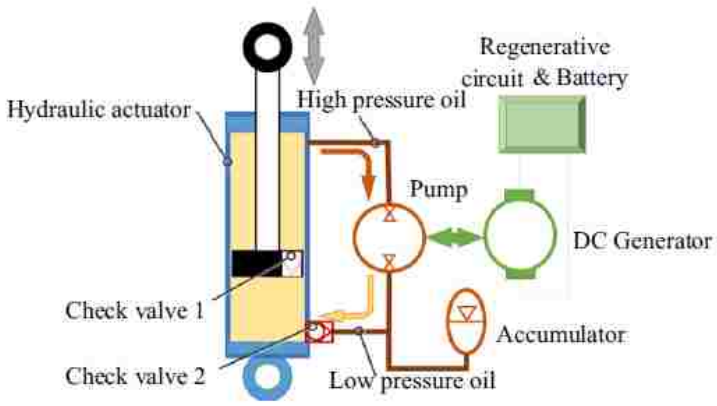

Figure 2.2-4: System layout of the pumping regenerative suspension [14]

The system that is shown in Figure 2.2-4 is composed by a hydraulic actuator, a hydraulic pump, a DC generator, an accumulator, two check valves, and a regenerative circuit.

The working principle of the considered system is:

- During the extension, the check valve 1 is closed and the check valve 2 is open, and the rod chamber's high pressure oil flows into hydraulic pump and drives it. The low pressure oil flows into the rodless chamber through the check valve 2, while the accumulator compensates the cavity due to the piston rod extraction;
- During the compression stroke, the check valve 1 is open and the check valve 2 is closed, and then the rodless chamber oil flows into the rod chamber through the check valve 1. Due to the fact that the rod chamber cross sectional area is smaller than the rodless chamber cross sectional area, the high pressure oil overflows into the hydraulic pump and drives it, and the low pressure oil from the hydraulic pump flows back into the accumulator.

According to this working principle, the hydraulic pump rotates unidirectionally both in compression and extension and so does the generator as shown in Figure 2.2-5. The damping force can be adjusted by changing the generator external circuit load.

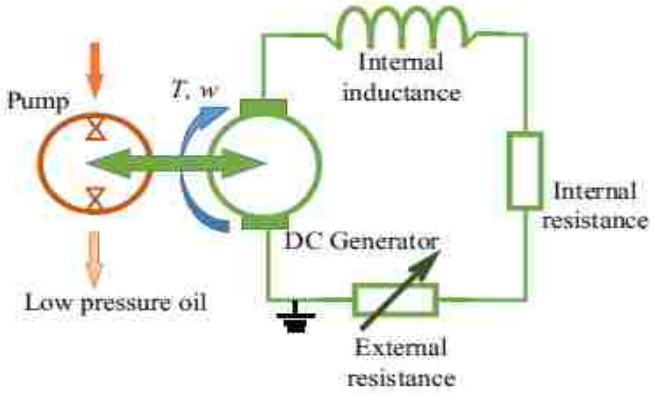

Figure 2.2-5: The energy recovery unit dynamics model [14]

The shock absorber described in this section can be developed from a traditional double tube shock absorber as shown in Figure 2.2-6. The check valve 1 and 2 are replaced by the piston valve and the base valve, respectively, and an additional tube is coaxially arranged outside of the working cylinder. The oil can flow out of the rod chamber through the orifice and the additional tube, and a gas reservoir in the upper part of the container tube is the accumulator. In this way the actuator can provide constant one-way oil for the hydraulic pump.

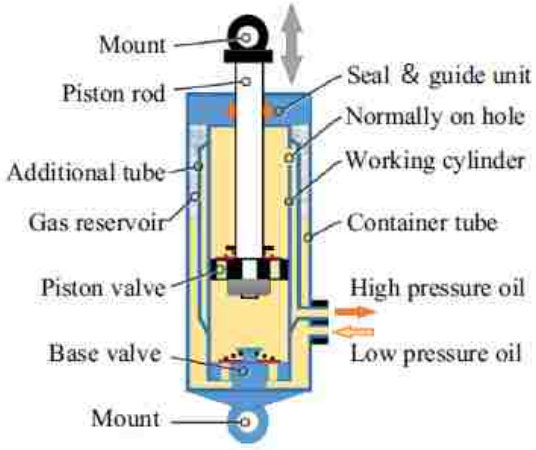

Figure 2.2-6: Overall structure of an integrated hydraulic actuator [14]

The design of the system described in [14] is based on the shock absorber of a medium size SUV. The electric machine considered is a brushless DC motor that works as a

generator, integrated with the hydraulic pump shaft. As a result, the unit for the energy recovery is compact and highly efficient [13].

The system illustrated has the advantage that different jounce/rebound damping forces ratios can be obtained by changing the flow ratio in jounce/rebound process. This can be achieved by adjusting the ratio of rod diameter and working cylinder diameter. These two parameters determine the damping force if external load, pump capacity, and input rod velocity are known [15] [16]. Different loops can be obtained only by adjusting the rod diameter as shown in Figure 2.2-7.

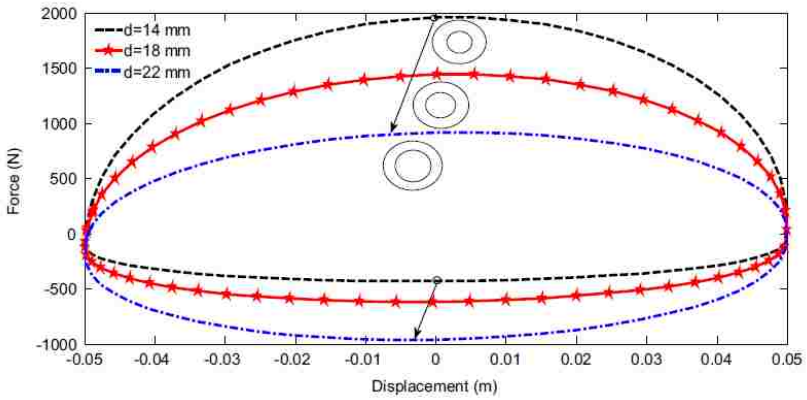

Figure 2.2-7: Force-displacement loops with different rod diameters (External load=15 Ohm, Input frequency=1.67 Hz, Displacement amplitude=50 mm) [14]

The model presented in [14] shows that the pump capacity directly influences the DC generator rotation speed, and therefore the generated power. The selection of the right pump capacity is influenced by the limits in terms of rotation speed of the generator (usually from 2000 rpm to 6500 rpm). The larger the pump capacity, the lower the rotation speed of the electric generator and thus the output electrical power. It also must be noted that the power generated in the rebound phase is bigger than the one in the jounce phase due to the higher oil flow rate in the former case.

As far as the influence of the input frequency on the damping force and the regenerated power is concerned, they both increase with increasing frequency. This is due to the fact that the higher input frequency can provide a larger flow rate that makes the generator rotate faster and finally obtain a larger damping force and a higher output power peak.

Regenerated power and damping force are directly affected by the external electrical load [8] [15] [16], as shown in Figure 2.2-8. A proper value must be chosen in order to obtain a suitable damping characteristic.

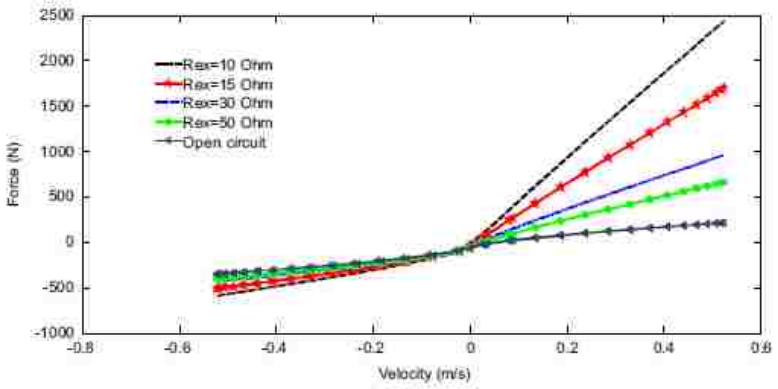

Figure 2.2-8: Force-velocity relationships with different electrical loads (Input frequency=1.67 Hz, displacement amplitude=50 mm) [14]

In order to establish the merits of the system considered, the energy conversion efficiency must be evaluated. The total efficiency of this regenerative suspension contains both the hydraulic and the electrical efficiency. The electrical efficiency can reach a relatively high level due to the low internal resistance of the generator. The hydraulic efficiency can be calculated from the area of the force-displacement loops under open circuit (S_{open}, energy dissipated by the hydraulic system) and the target external load (S_{target}) [14]:

$$\eta_H = \frac{(S_{target} - S_{open})}{S_{target}} \tag{2.2}$$

where the numerator is the energy transmitted into the oil kinetic energy.

The plot in Figure 2.2-9 shows the hydraulic efficiency for different external electrical loads and frequencies. It is clear that the efficiency decreases with the decrease of the load. In the case considered, with an input frequency of 1.67 Hz and an electrical load of 15 Ω, that can provide the proper compression/extension damping force for the vehicle considered, the hydraulic efficiency is up to 73.2% [14].

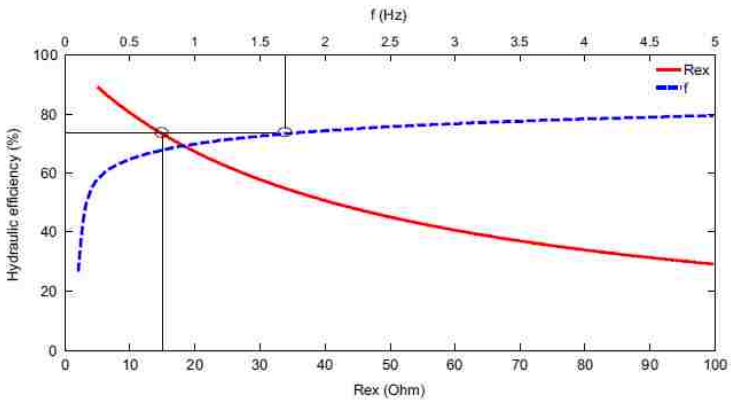

Figure 2.2-9: Hydraulic efficiency with different loads (input frequency=1.67 Hz, displacement amplitude=50 mm) and different frequencies (external load=15 Ω, displacement amplitude=50 mm) [14]

From [11] [13] [14], it can be concluded that an increase in the electrical load can lead to relatively high energy conversion efficiency. On the contrary, this also leads to a low value of the damping force, that is usually accompanied by a reduction of road handling performance. Thus, a trade-off between regenerative efficiency and suspension performance must be considered in the selection of the external electrical load.

2.2.3.2 Mechanical motion conversion

Other mechanisms can also be adopted in order to convert linear motion into rotary motion. The most commonly used systems are ball-screw and rack and pinion mechanisms that convert the motion into rotational and maintain the oscillatory behaviour typical of the suspension vertical motion. In order to obtain a unidirectional motion, systems like the mechanical motion rectifier (MMR) described in [17] can be implemented.

Firstly the rack-pinion-based shock absorber will be considered [16].

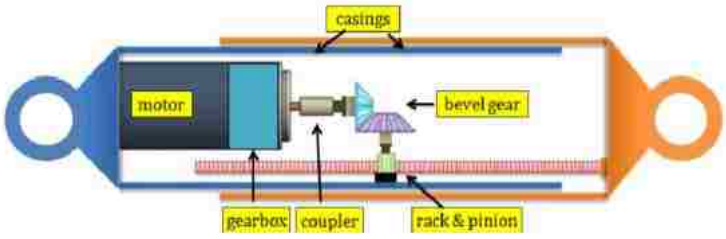

Figure 2.2-10: Overall structure of the rack-pinion-based regenerative shock absorber [16]

The base principle of this type of regenerative shock absorber is shown in Figure 2.2-10. The system is made of rack and pinion, bevel gears, planetary gears, and the electrical machine. The electric generator assembly is mounted on a cylinder, and the outer

cylinder is used to enclose the system. The rack is connected with the end of the outer cylinder and drives the pinion gear when there is a relative motion between the two ends of the damper. Through the bevel gears, the rotational motion of the pinion gear is transferred by 90º to the rotational motion of the electrical machine. The planetary gears are used to magnify the motion, and a DC motor is used as a generator.

Also Li *et al.* [18] studied and built a rack and pinion-based shock absorber, but the prototype is not applicable on conventional passenger due to the large outside diameter (reduced to 72 mm in [16]). In order to reduce the large backlash impacts and friction forces in the transmission, in [16] a roller is used to guide the rack on the opposite side of the pinion gears. Moreover, a Teflon ring is put between the inner and the outer cylinders in order to further reduce the friction forces.

One of the critical points in the design of this type of regenerative shock absorber is the selection of gears that can remarkably affect the overall performance. A higher transmission ratio results in a higher damping coefficient but has the drawback to reduce the transmission efficiency. On the contrary, a smaller transmission ratio guarantees higher transmission efficiency associated with a better compactness, but with less expected damping coefficient. According to these considerations, the selection of gears is a compromise between performance, efficiency, and compactness.

An additional aspect to be checked is the failure that can occur in the bevel and rack and pinion gears.

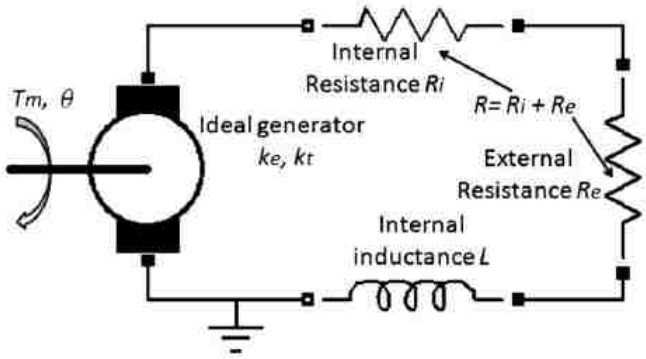

Figure 2.2-11: Dynamic modeling of the electromagnetic generator, where Re can be the equivalent resistance of the power charge circuit [16]

The generator can be modeled as in Figure 2.2-11, where *Ri* and *L* are the internal resistance and inductance of the motor respectively. The resistance of the external load or

charging circuit is *Re*. In fact it is useful to note that the charging circuit with a dc/dc converter can be modeled as a pure resistor *Re* controlled with pulse width modulation (PWM) under moderate assumptions, as will be discussed later.

The equivalent damping coefficient of the considered system is [16]:

$$C_{eq} = \frac{{k_g}^2 k_e k_t}{r^2 \eta_g R} + k_v \tag{2.3}$$

It is clear that the damping is influenced by the generator constant k_e and k_t, the transmission ratio k_g from the pinion gear to the generator rotor, the loop resistance $R = r_i + R_e$, and the viscous friction coefficient k_v between the inner and the outer cylinder. r and η_g are pinion radius and the efficiency of the transmission respectively. Thus the damping coefficient can be controlled with the resistance R_e of external load or charging circuit.

The whole system can be viewed as the equivalent mass m_{eq} and a damper with damping coefficient C_{eq} in series, where m_{eq} is:

$$m_{eq} = \frac{J_g + \frac{J_m {k_g}^2}{\eta_g}}{r^2} + (m_r + m_c) \tag{2.4}$$

where J_g is the rotation inertia of the gear transmission system from the pinion gear to the generator rotor; m_r and m_c are the masses of the rack and the moving casing.

It is interesting to note that asymmetric damping coefficients, that are extremely important in vehicle suspension in order to guarantee a good performance, can be obtained by shunting the regenerative shock absorber with different electric loads during the jounce and rebound motions. A simple circuit like the one shown in Figure 2.2-12 can be built in order to achieve the asymmetry, considering that the upward and downward motions will generate voltages with opposite polarities in the DC generator. In this way the regenerative damper can act like a conventional hydraulic shock absorber.

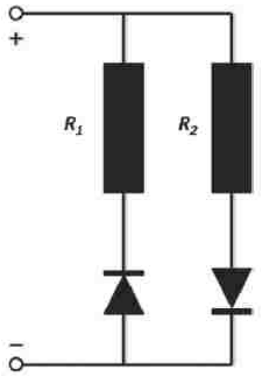

Figure 2.2-12: Control circuit for asymmetric characteristics [16]

As far as the mechanical efficiency is concerned, it varies from 33% to 63% according to the different vibration frequencies and different electrical loads. The maximum value of mechanical efficiency is obtained for input frequencies around 1 Hz, while it decreases at high frequencies.

Finally, a total energy conversion efficiency of up to 56% has been obtained using a prototype of the system under an input vibration with amplitude of 30 mm, frequency 0.5 Hz, and 94 Ohm external load.

Using the mentioned prototype on a smooth road with a vehicle speed of 48 km/h, a peak power of 67.5 W and an average power of 19.2 W can be obtained (considering four energy-harvesting shock absorbers) [16].

A mechanism that can reduce the backlash typical of a rack and pinion system is the ball screw. Different configurations of this system can be implemented. Two of them are shown in Figure 2.2-13.

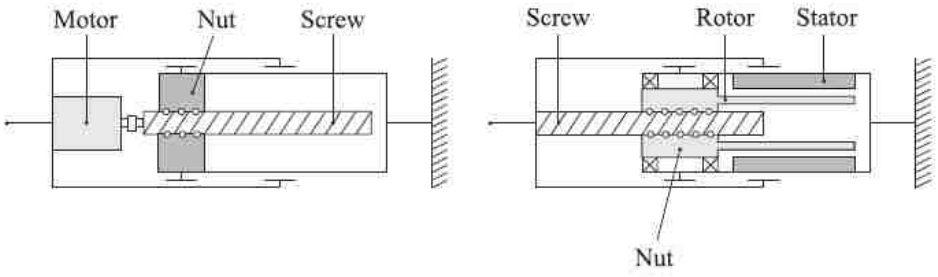

Figure 2.2-13: Ball screw mechanism: rotating screw (left), rotating nut (right) [9]

In the arrangement shown on the left, the screw can rotate and is coupled with the rotor of the electrical machine, while in the one shown on the right, the screw is fixed and the nut,

coupled with the rotor, can rotate. This latter configuration is preferred concerning the dimensions, due to the fact that it allows lower overall mass and rotor inertia [9]. Zhang *et al.* [19] conducted experimental tests on a ball screw based suspension and found that that it can achieve good performance of shock isolation from road excitation at low frequencies, but ride performance at high frequencies is worse than that of a passive suspension.

2.2.3.2.1 Mechanical motion rectifier

The rack and pinion solution described so far is improved in [17]. A new solution is proposed by the authors in order to solve the problems caused by the irregular oscillation of the motion mechanism, such as low mechanical reliability and bad vibration performance. In fact, the bidirectional oscillation causes a large impact force, backlash and friction in the transmission system, causing fatigue or even failure. In addition, the bidirectional oscillating motion produces an irregular AC voltage. In order to charge the batteries, the voltage needs to be commutated with an electrical rectifier, in which the forward voltage of diodes unavoidably reduces the circuit efficiency.

The authors in [17] proposed a mechanical motion rectifier that converts bidirectional motion into unidirectional motion, as the hydraulic system described in Section 2.2.3.1. It is worth to note that the system does not substitute an electrical voltage rectifier. Nevertheless it can significantly improve reliability by reducing impact forces and increase efficiency by decreasing the influence of friction. It also enables the electrical generator to rotate unidirectionally at relatively steady speed with higher energy efficiency. The working principle of the motion rectifier is showed in Figure 2.2-14. Two working modes can be defined: positive mode and negative mode. The components of the motion rectifier that allow the switching from one mode to the other are two one-way roller clutches which transmit rotation only in one direction and drive the motion in two different routes. This allows the shaft of the motor and the planetary gear to always move in one direction.

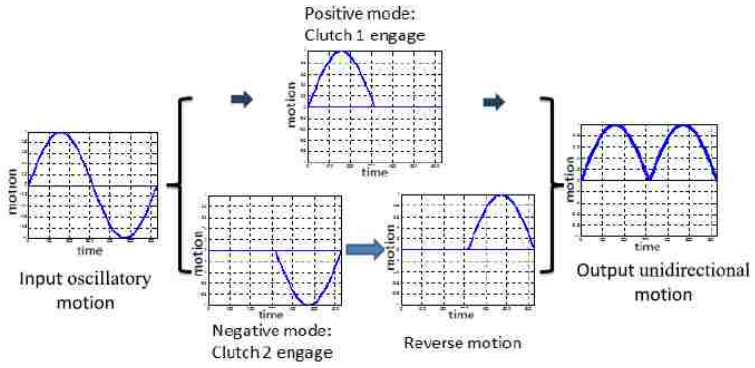

Figure 2.2-14: Principle of motion rectifier for oscillating motion [17]

The system that works with the mentioned modes has to be sufficiently compact, thus the motion transmission needs to be well organized to fit into the existing space of the shock absorber.

The number of gears pairs and shafts needs to be as low as possible in order to improve the mechanical efficiency.

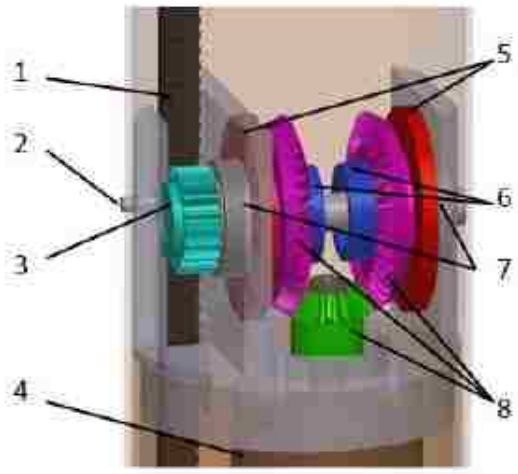

1 rack
2 roller
3 pinion
4 planetary gears and motor
5 thrust bearings
6 roller clutches
7 ball bearings
8 bevel gears

Figure 2.2-15: 3D model of the mechanical motion rectifier [17]

As is shown in Figure 2.2-15, the mechanism is composed of a pair of rack and pinions, one shaft and three bevel gears. Two roller clutches (blue) are mounted between the shaft (gray) and the two larger bevel gears (purple), which are always engaged with the small bevel gear (green). The bevel gears can be of the same size or of different size in order to give an additional transmission ratio.

When the rack moves up and down, the pinion and the shaft rotate in clockwise and counterclockwise directions. Due to the engagement of the one-way roller clutches, at

any instant only one of the two large bevel gears will be engaged and be driven by the shaft while the other will be disengaged. These two large bevel gears will be driven in opposite directions by the shaft. They are on two opposite sides of the small bevel gear (that is coupled with the generator) that will be always driven by either the left or right bevel gear and will rotate in one direction no matter whether the rack goes up or down.

Due to the fact that the regenerative shock absorber involves both mechanical and electrical domains, it is better to transfer the mechanical elements into equivalent electrical elements in order to analyze the system. In this way the system can be model by making an analogy between a mechanical motion rectifier and an electrical voltage rectifier (even if it is not just a substitute for an electrical voltage rectifier).

Based on the circuit-based modeling method, a Matlab/Simulink simulation was conducted.

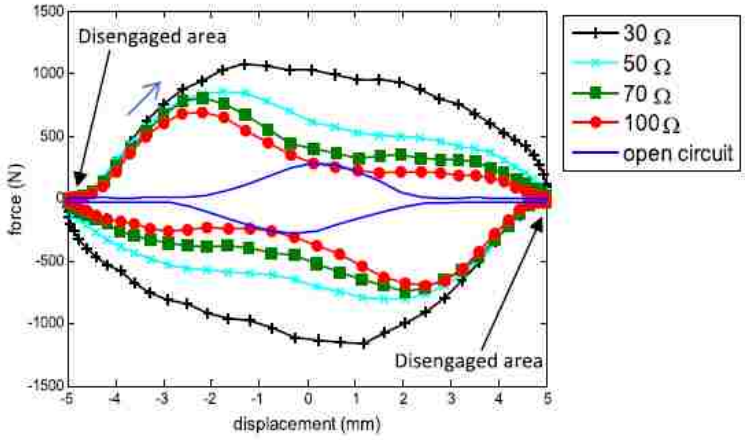

Figure 2.2-16: Damping loops for different external electrical loads under vibration input of 1.5 Hz and 5 mm amplitude [17]

The force-displacement damping loops under harmonic excitations are shown in Figure 2.2-16. The area in the loop indicates the mechanical work output of the shock absorber in one cycle. When there is no resistor connected (open circuit), the damping loop area is contributed by mechanical loss such as frictions.

The performance of the shock absorber at different frequencies is also investigated in [17], as shown in Figure 2.2-17.

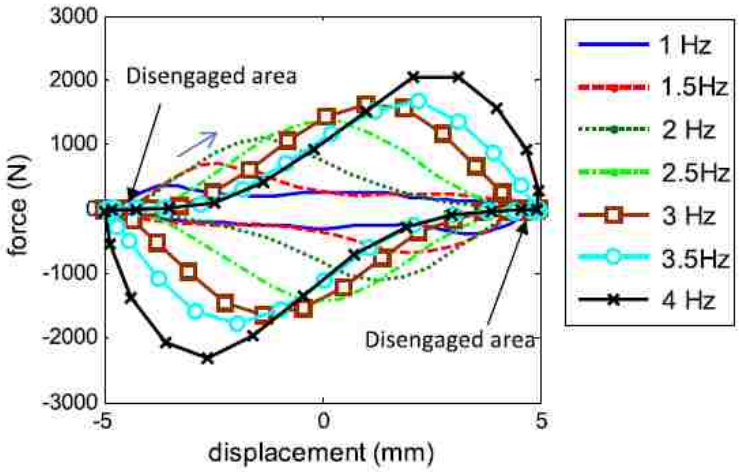

Figure 2.2-17: Damping loops for different input frequencies with electrical load 106.6 Ω [17].

As far as the electrical power is concerned, peak powers of 62.9 W and 104.3 W, and average powers of 25.6 W and 40.4 W can be harvested with an input of 3 Hz and 5 mm displacement on 100 Ω and 30 Ω electrical loads respectively.

The total efficiency of the system can be decomposed into the electrical and mechanical efficiency. The electrical efficiency is the ratio of power on the external electrical load to the total electrical power. The electrical efficiency for the prototype considered in [17] is 82% and 94% for electrical resistance of 30 Ω and 100 Ω respectively.

The mechanical efficiency under 1.5 Hz and 5 mm amplitude vibration is around 60%. It can be noted that it increases when the electrical resistance decreases. It is also important to highlight that the mechanical efficiency tends to increase with increasing vibration frequency. The efficiency rises until it reaches a steady value around 62% in the prototype considered.

The efficiency of the system considered is significantly improved at higher frequency (15-30%) if compared to a conventional regenerative shock absorber in oscillatory rotation. The feasibility of the prototype is also verified by the author by a road test, in which 15.4 W power is obtained at 15 mph on a smooth paved road.

2.3 Basic principles of magnetic circuits

The basic principle of the regenerative shock absorber is the conversion of mechanical energy into electrical energy. This is made possible due to the utilization of a particular electric machine: permanent magnet brushless DC motor. In order to understand the functioning of this type of electrical machine, some basic principles about magnetic circuits are first introduced.

When a current *i* flows through a conductor, a magnetic field with a direction dependent on the current direction is produced. The intensity *H* of the magnetic field produced by current-carrying conductors can be computed using Ampere's Law that states that the line (contour) integral of the magnetic field intensity along any closed path equals the total current enclosed by this path [20].

$$\oint Hdl = \sum i \tag{2.5}$$

The scalar *H* is the component of the magnetic field intensity in the direction of *dl* along the closed path. The flux density *B* (expressed in Tesla), at any instant of time *t* for a given *H*-field, depends on the permeability of the material on which the field is acting. If air is considered:

$$B = \mu_0 H \tag{2.6}$$

where $\mu_0 = 4\pi \times 10^{-7}\ \left[\frac{Henries}{m}\right]$ is the permeability of air.

The permeability μ_m of a material is expressed in terms of the permeability μ_r relative to the permeability of air:

$$\mu_m = \mu_r \mu_0 \tag{2.7}$$

In ferromagnetic materials, the μ_m can be several thousand times larger than the μ_0.

2.3.1 Flux ϕ

As shown in the toroidal-shaped magnetic core surrounded by a coil in Figure 2.3-1, magnetic flux lines form closed paths. In order to compute the flux in the toroid, a circular area A_m in a plane perpendicular to the direction of the flux lines has to be selected.

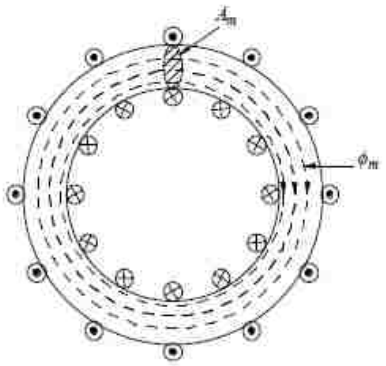

Figure 2.3-1: Toroid with flux Φ_m [20]

Assuming a uniform H_m and a uniform flux-density B_m throughout the core cross-section, the following relation holds:

$$B_m = \mu_m \frac{Ni}{l_m} \tag{2.8}$$

where B_m is the density of flux lines in the core, l_m the mean path length, N the number of coils and i the current flowing in the conductor.

Therefore the flux expressed in $[Wb]$ is:

$$\phi_m = B_m A_m \tag{2.9}$$

Substituting Eq. (2.8) into Eq. (2.9):

$$\phi_m = A_m \left(\mu_m \frac{Ni}{l_m}\right) = \frac{Ni}{\left(\frac{l_m}{A_m \mu_m}\right)} \tag{2.10}$$

The term in brackets at the denominator is the reluctance of the magnetic core expressed in $[A/Wb]$.

2.3.2 Flux linkage

A flux linkage λ can be defined if all turns of a coil are linked in the same flux ϕ [20]:

$$\lambda = N\phi \tag{2.11}$$

2.3.3 Magnetic structures with air gaps

In an electrical machine, the flux lines have to cross the air gaps twice. In order to study the effect of air gaps, the simple magnetic structure in Figure 2.3-2 is considered. It consists of an *N*-turn coil on a magnetic core made up of iron.

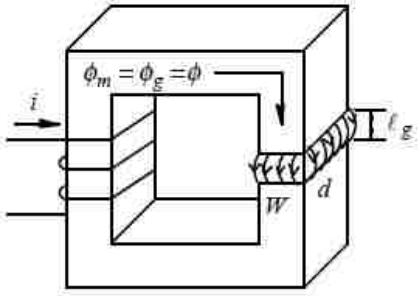

Figure 2.3-2: Simple magnetic structure with air gap [20]

The aim is to establish a desired magnetic field in the air gap of length l_g by controlling the coil current i. Assuming the magnetic field intensity H_m uniform along the mean path length l_m, denoting the magnetic field intensity in the air gap as H_g, from the Ampere's Law, the following equation holds [20]:

$$H_m l_m + H_g l_g = Ni \tag{2.12}$$

Applying Eq. (2.6) and Eq. (2.8), Eq. (2.12) can be written as:

$$\frac{B_m}{\mu_m} l_m + \frac{B_g}{\mu_0} l_g = Ni \tag{2.13}$$

Due to the fact that flux lines form closed paths, the flux in any perpendicular cross-sectional area in the core is the same as that crossing the air gap, thus:

$$\phi = B_m A_m = B_g A_g \tag{2.14}$$

The flux lines bulge slightly around the air gap, as shown in Figure 2.3-2; this is called the fringing effect, which can be considered by estimating the air gap area A_g, which is done by increasing each dimension in Figure 2.3-2 by the length of the air gap:

$$A_g = (W + l_g)(d + l_g) \tag{2.15}$$

Substituting flux density from Eq. (2.14) into Eq. (2.13),

$$\phi\left(\frac{l_m}{A_m\mu_m}+\frac{l_g}{A_g\mu_0}\right)=Ni \tag{2.16}$$

The two terms in the parenthesis equal the reluctance of the core and of the air gap. Thus the reluctance of the whole structure in the path of the flux lines is the sum of the two reluctances:

$$\Re = \Re_m + \Re_g \tag{2.17}$$

Substituting Eq. (2.17) into Eq. (2.16), where the ampere-turns Ni equals the applied mmf F,

$$\phi = \frac{F}{\Re} \tag{2.18}$$

2.3.4 Inductances

At any instant of time, the flux linkage λ_m of the coil in Figure 2.3-3 is related to the current i by the inductance L_m:

$$\lambda_m = L_m i \tag{2.19}$$

The inductance L_m is constant if the core material is in its linear operating region. Thus the coil inductance in the linear magnetic region is:

$$L_m = \frac{N^2}{\Re_m} = \frac{N^2}{\left(\frac{l_m}{\mu_m A_m}\right)} \tag{2.20}$$

So it is clear that the inductance is a property of the magnetic circuit as long as the operation is in the linear range of the magnetic material (where μ_m is constant).

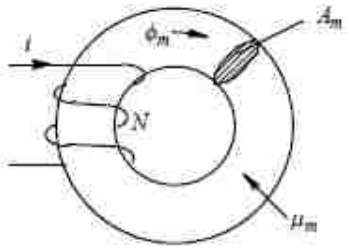

Figure 2.3-3: Coil inductance [20]

2.3.5 Faraday's Law

The relation introduced so far between the electrical quantity i and the magnetic quantities ϕ, H, λ and B hold under static conditions as well as at any instant when these quantity are varying with time. Under time-varying conditions Faraday's Law, referred to the coil in Figure 2.3-4, states that the time-rate of change of flux-linkage equals the voltage (emf) across the coil at any instant [20]:

$$e(t) = \frac{d}{dt}\lambda(t) = N\frac{d}{dt}\phi(t) \tag{2.21}$$

assuming that all flux lines link all N-turns such that $\lambda = N\phi$.

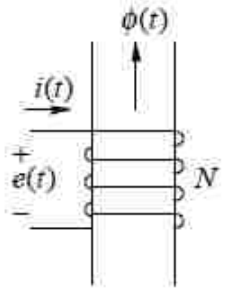

Figure 2.3-4: Voltage polarity and direction of flux and current [20]

Considering the Ampere's Law, the coil flux linkage can be expressed in terms of its inductance and current:

$$\lambda(t) = Li(t) \tag{2.22}$$

Assuming that $\lambda(t) = N\phi(t)$, and plugging it into Eq. (2.22):

$$\phi(t) = \frac{L}{N}i(t) \tag{2.23}$$

Thus substituting Eq. (2.23) into Eq. (2.21):

$$e(t) = N\frac{d\phi}{dt} = L\frac{di}{dt} \tag{2.24}$$

2.3.6 Permanent Magnets

In many electric machines, especially in smaller ratings, permanent magnets are used. Their utilization is linked to the fact that they provide a "free" source of flux, that otherwise has to be created by current-carrying windings with the related losses (i^2R). They can guarantee higher efficiency and higher power density.

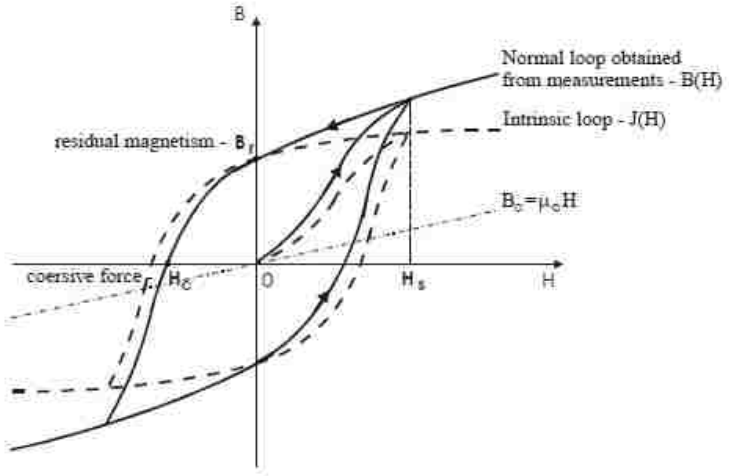

Figure 2.3-5: Normal and intrinsic hysteresis loops of a permanent magnet material [21]

A permanent magnet can be described by its *B-H* curve, which has a wide hysteresis loop, as shown in Figure 2.3-5. For permanent magnets, the most important part of the *B-H* curve is the demagnetization curve, the part included in the second quadrant. There are two significant points on the demagnetization curve. One point at *H=0* where the magnetic flux density is equal to B_r (remanent magnetic flux density or remanence) and the other point is H_c (*B=0*) where a reverse magnetic field intensity is applied to a magnetized permanent magnet (coercive force or coercitivity).

The saturation magnetic flux density B_{sat} corresponds to high values of magnetic field intensity when an increase in the applied magnetic field does not produce any significant effect on the magnetic flux density.

The maximum magnetic energy per unit produced by a permanent magnet is the maximum energy density per volume, thus:

$$W_{max} = \frac{(B \cdot H)_{max}}{2} \qquad [J/m^3] \tag{2.25}$$

The permanent magnet materials used in electric machines are:

- Alnico (*Al, Ni, Co, Fe*);
- Ferrites (ceramics);
- Rare-earth materials.

The properties of the listed materials are reported in Table 2.3-1.

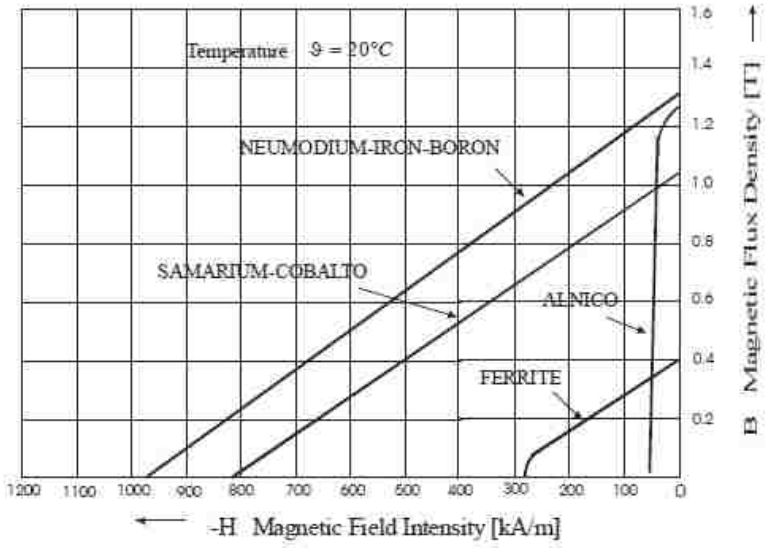

Figure 2.3-6: Demagnetization curves for different permanent magnet materials [22]

In Figure 2.3-6 the demagnetization curves of the permanent magnet materials mentioned are reported; samarium-cobalt (*SmCo*) and neodymium-iron-boron (*Nd-Fe-B*) are two examples of rare-earth materials.

Table 2.3-1: Parameters of permanent magnet materials [21]

Material	$(\boldsymbol{B \cdot H})_{\boldsymbol{max}}$ $[\boldsymbol{kJ/m^3}]$	$\boldsymbol{B}$ $[\boldsymbol{T}]$	$\boldsymbol{H_c}$ $[\boldsymbol{kA/m}]$
Ceramics	27-35	0.4	240
Alnico	70-85	1.1	130
Rare earth magnets:			
• $SmCo_5$	160-200	0.9-1.0	660-750
• Sm_2Co_{17}	205-240	1.04-1.12	760-820
• *Nd-Fe-B*	190-385	1.0-1.4	760-980

The previously listed PM materials are reported in order of appearance in the electric machine industry. The latest to be introduced are rare earths PMs. The first generation is based on the composition $SmCo_5$, and has high remanent flux density, high coercive force, a linear demagnetization curve, and a low temperature coefficient. The

disadvantages for this material are related to the high cost, due to the supply restriction of samarium and cobalt.

In order to reduce the cost issue, a second generation of rare earths has been discovered with neodymium and iron. *Nd-Fe-B* magnets have better properties compared to first generation magnets but have the disadvantages that they are susceptible to corrosion and that their demagnetization curves depend on temperature. A degradation of the properties of the permanent magnets occurs with the increase of temperature, and they vanish completely at Curie temperature.

2.4 Basic principles of electromechanical energy conversion

Electric machines used as motors convert electrical power input into mechanical output. The same machines can be operated entirely as generators. In this section only rotating machines will be considered, but the same fundamental principles can be applied to linear machines.

2.4.1 Basic structure

Electric machines are usually described by considering a cross-section perpendicular to the shaft axis, as shown in Figure 2.4-1. The machines have a stationary part, called stator, and a rotating part, called rotor, separated by an air gap, so that the rotor can rotate freely on a shaft, supported by bearings.

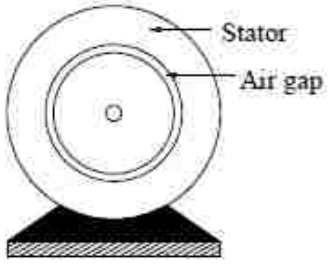

Figure 2.4-1: Cross-section of the electric motor seen from one side [20]

Both the rotor and the stator are made up of high permeability ferromagnetic materials and the value of the air gap is as small as possible (typical value is about 1 mm for machines with ratings under 10 kW).

In Figure 2.4-2 (on the left), the distribution of the flux produced by the stator is shown for a 2-pole machine where the field distribution corresponds to a combination of a single north pole and a single south pole. Usually there are more than two poles, for instance 4 or 6. In Figure 2.4-2 (on the right), the flux distribution for a 4-pole machine is shown.
Due to the symmetry of the machine along the air gap, just one pole pair consisting of adjacent north and south pole can be considered. The same considerations and calculations can be done for the other pole pairs.

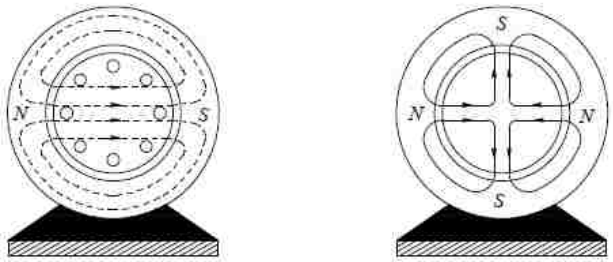

Figure 2.4-2: Structure of a 2-pole (left) and 4-pole (right) machine [20]

2.4.2 Basic principles of operation

There are two principles that govern the operation of electrical machines in the conversion between electric energy and mechanical work [23]:

- When a conductor moves in a magnetic field, voltage is induced in the conductor;
- When a current-carrying conductor is placed in a magnetic field, the conductor experiences a mechanical force.

The two effects occur simultaneously whenever energy conversion takes place from electrical to mechanical or vice versa.
A conductor of length *l*, carrying a current *i* and subjected to an externally established magnetic field of uniform flux density *B* perpendicular to the conductor length is considered. Due to the electromagnetic interaction between the external magnetic field and the conductor current, a force f_{em} is exerted on the conductor, where:

$$f_{em} = Bil \tag{2.26}$$

The direction of the force is perpendicular of the directions of both *i* and B.

If a conductor of length l is moving to the right at a speed u, as shown in Figure 2.4-3, and there is a B-field uniform and perpendicularly directed into the paper plane, the induced emf at any instant of time is:

$$e = Blu \tag{2.27}$$

In order to establish the polarity of the induced emf, the force due to the conductor motion on a charge q can be written as:

$$f_q = q(\mathbf{u} \times \mathbf{B}) \tag{2.28}$$

Considering that **u** and **B** are orthogonal to each other, as shown in Figure 2.4-3 on the right, the force on a positive charge is upward, downward if a negative charge (electron) is considered.

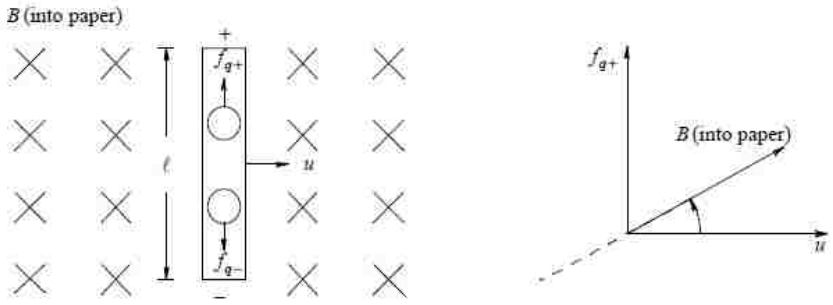

Figure 2.4-3: Conductor moving in a magnetic field [20]

The induced emf considered is independent of the current flowing in it if a closed path is provided. In that case, the voltage across the conductor will be the emf of Eq. (2.28) minus the voltage drop across the resistance and the inductance of the conductor.

2.4.3 Application of the basic principles: eddy current dampers

The principles explained so far are exploited in electrical machines like the one considered in this work to perform the mechanical to electrical energy conversion. These machines, according to their suitable characteristics, i.e. that the force that they exert is proportional to the relative speed between rotor and stator, can be used as dampers, as in the present application. As a matter of fact, according to Faraday's Law, a conductor that moves in a magnetic field is subjected to a voltage, known as back electromotive force. Shunting the conductor by a resistance, the back electromotive force induces a current in the conductor that interacts with the magnetic field. This generates a Lorentz's force that

counteracts the relative motion between stator and rotor. In the PM brushless DC motor considered in this work, the magnetic field is generated by means of permanent magnets placed on the rotor [24].

The relationships that allow the calculation of the reaction torque starting from the relative angular velocity are reported in this section. In order to do that, the general case of the sketch of Figure 2.4-4 is taken into consideration. It is a torsional damper with a single pole pair. A constant magnetic flux density **B** is generated by the stator (by permanent magnets or current driven electromagnets) and two orthogonal windings are placed on the rotor. The angular speed of the rotor is given as input.

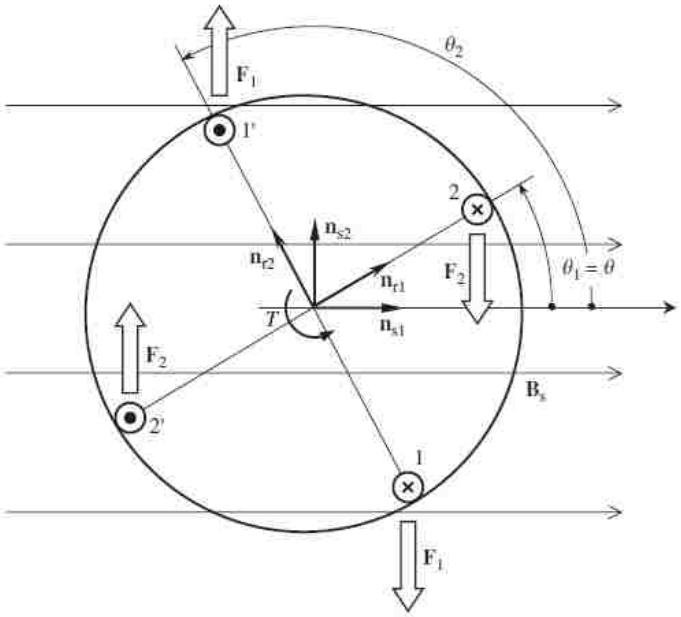

Figure 2.4-4: Sketch of a torsional damper (or an induction machine) [24]

The angles θ_1 of vector $\mathbf{n}_{r1}$ (normal to the winding 1,1') and θ_2 of vector $\mathbf{n}_{r2}$ (normal to the winding 2,2') are considered with respect to the direction of **B**. Being the two winding orthogonal, the following relations hold:

$$\begin{aligned} \theta_1(t) &= \theta(t) \\ \theta_2(t) &= \theta(t) + \pi/2 \end{aligned} \tag{2.29}$$

where $\theta(t)$ is the rotation angle.

The total magnetic flux λ_{r1} and λ_{r2} is due to the self–inductance L_r and the stator magnetic field (i=1,2 according to the considered winding) [24]:

$$\lambda_{ri} = L_r i_{ri} + \lambda_{rsi} \tag{2.30}$$

where:

$$\lambda_{rsi} = \int_{Si} \mathbf{B} \cdot \mathbf{n} dS = Nld\mathbf{B} \cdot \mathbf{n}_{ri} = BNld \cos\theta_i \tag{2.31}$$

(*N* is the number of coils, *l* is the rotor length, *d* is the diameter, S_1 and S_2 are the surface delimited by the two windings).

The rotor fluxes, which depend on the rotor rotation, can thus be computed, by substituting Eq. (2.29) into Eq. (2.31):

$$\begin{aligned} \lambda_{rs1} &= \lambda_{rs0} \cos\theta_1 = \lambda_{rs0} \cos\theta \\ \lambda_{rs2} &= \lambda_{rs0} \cos\theta_2 = -\lambda_{rs0} \sin\theta \end{aligned} \tag{2.32}$$

where $\lambda_{rs0} = BNld$ is the maximum magnetic flux linked by each winding.

According to the Kirchhoff's voltage law, the currents induced in the windings due to the electromotive force can be calculated [24]:

$$\frac{d\lambda_{ri}}{dt} + R_r i_{ri} = 0 \tag{2.33}$$

where R_r is the resistance of the rotor.

Plugging Eqs. (2.30) and (2.32) into Eq. (2.33), the following equations for the calculation of the induced current can be obtained:

$$\begin{aligned} L_r \frac{di_{r1}}{dt} + R_r i_{r1} &= \lambda_{rs0} \sin\theta\dot{\theta} \\ L_r \frac{di_{r2}}{dt} + R_r i_{r2} &= \lambda_{rs0} \cos\theta\dot{\theta} \end{aligned} \tag{2.34}$$

The currents calculated by Eqs. (2.34) interact with the stator magnetic field and generate the Lorentz forces $\mathbf{F}_i$ on the conductors. Being the magnetic field perpendicular the conductors:

$$F_i = BNli_{ri} \tag{2.35}$$

Thus the electromagnetic torque T_{em} is:

$$T_{em} = -F_1 d \sin\theta - F_2 d \cos\theta = -\lambda_{rs0}(i_{r1} \sin\theta + i_{r2} \cos\theta) \quad \textbf{(2.36)}$$

The torque can be also considered as the following vector product:

$$T_{em} = -\mathbf{i}_r \times \lambda_{rs0} \quad \textbf{(2.37)}$$

where $\mathbf{i}_r = i_{r1}\mathbf{n}_{r1} + i_{r2}\mathbf{n}_{r2}$ is the current vector.

The stator magnetic flux λ_{rs0} can be considered as the torque constant of the electric machine. This torque, which is dependent on the relative velocity between rotor and stator, is opposite to the direction of their relative rotation. This characteristic makes them suitable for the application considered in this work. The basic principles described in this section for a general torsional damper are also valid for the PM brushless DC motor considered in this thesis, as discussed in Section 3.4.

3 MODEL DESCRIPTION

This chapter is dedicated to the description of the suspension analyzed in this work and the way in which it is modeled in Matlab. First, the description of the system is given, providing the type of suspension considered, and the type of regenerative shock absorber chosen. Then, the attention focuses on the code developed in order to simulate the described system. The way in which the outcomes stated in the first chapter are obtained is clearly shown; data needed as input are explicitly specified.

3.1 Suspension description

In this section, a general description of the suspension analyzed in this work is provided. Moreover, the characteristics of the regenerative shock absorber chosen for the project are described.

The suspension structure considered is the one of a double wishbone suspension type. As shown in Figure 3.1-1, there are two kinds of double wishbone suspension: the high type on the left that is suitable for front wheel drive cars with transversal powertrain, and the low type on the right that can be applied to longitudinal powertrain.

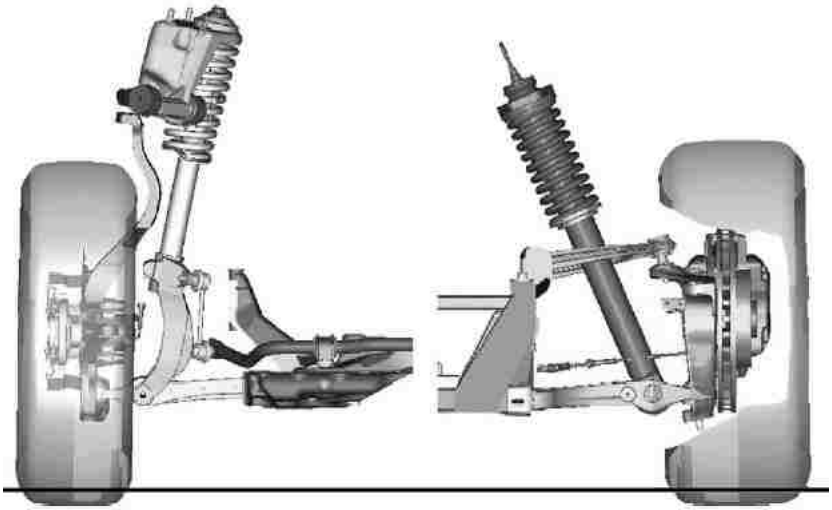

Figure 3.1-1: Double wishbone suspension example [3]

In this project a low type double wishbone suspension is considered, but other suspension structures can be relatively easily implemented, thanks to the high flexibility of the software used.

The suspension elements are:

- Upper A-arm;
- Lower A-arm;
- Upright;
- Tie-rod;
- Spring;
- Shock absorber.

The ends of the spring and the shock absorber are connected to the chassis and to the lower A-arm outboard end. The upright has the function to connect the outboard end of the arms, the tie-rod, and to carry the wheel. The tie-rod has the purpose to guarantee the steering capabilities, even if it is considered fixed in this project. The elements described are assembled to form the suspension structure shown in Figure 3.1-2.

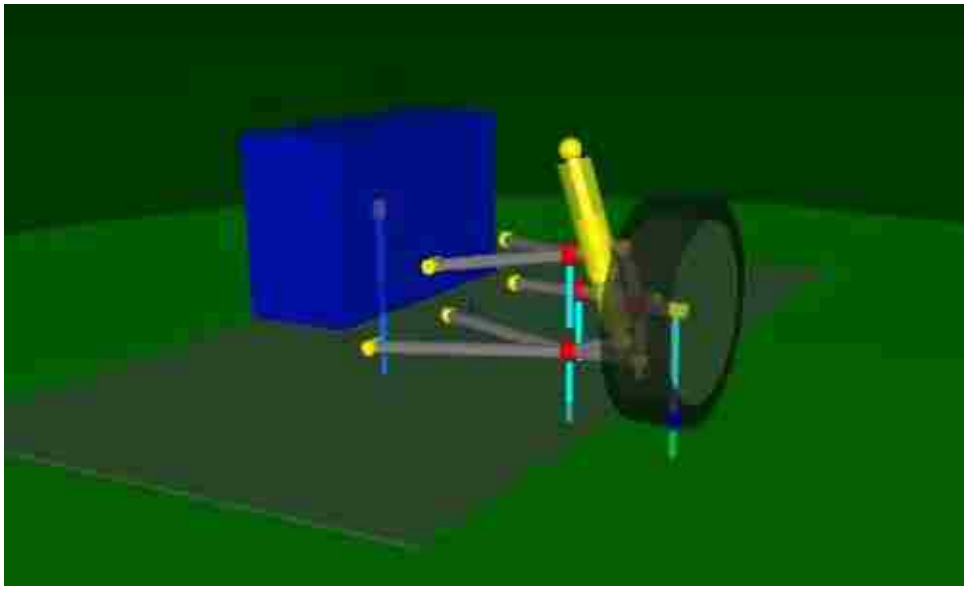

Figure 3.1-2: Double wishbone suspension model in EoM

3.1.1 Shock absorber description

In this section, the configuration of the regenerative shock absorber chosen for this study is described. The damper taken into consideration exploits a rotational electric permanent magnet (PM) machine for the mechanical to electrical energy conversion, in particular a PM brushless DC motor.

In order to implement this type of electric machine, the rotational electric motor is connected to a ball screw mechanism that converts the linear motion into rotational one. The choice of this solution is linked to the fact that the linear solution has to be avoided, due to the weight issues that characterize PM linear motors [25]. This is due to the fact that, while in a rotational motor all the magnetic and conductor material is always active during the operation, in linear motors only a portion of it is working on each phase. This means that, for fixed performance, a higher amount of magnetic and conductor material is needed. For this reason, this mechanism effectively cannot guarantee the proper damping to weight ratio necessary for its on-vehicle application. Moreover, the rotational motor is selected in order to take advantage of the more consolidated design practice and of the higher technological background of this type of machine with respect to the linear one [26].

For the conversion from linear to rotational motion, the ball screw is selected because it shows less backlash and friction issues compared to the rack and pinion system, which is the main alternative for this task. As stated in Section 2.2.3.2, there are two types of ball screw: one in which the screw can rotate while it is attached to the rotor of the motor and one in which the screw is fixed and the nut rotates with the rotor. The second solution is preferable because of the smaller dimensions and mass, thus rotor inertia.

The reason of the use of a PM brushless DC motor lies in the working principles of this kind of machine, based on the interaction between the conductor and the stator in relative motion. According to Faraday's Law, indeed, the relative motion between the rotor and the stator determines an electric field in the conductor. The latter induces a current that interacts with the magnetic field. Lorentz forces that oppose the relative motion are generated due to the interaction between the current-carrying conductor and the magnetic field. This characteristic of the PM brushless DC motor, i.e. that the reaction force is

proportional to the relative rotational speed, makes them suitable for their utilization as shock absorbers in automotive suspension [24].

Moreover, by using the proper power electronics, the converted energy can be regulated and stored into the car battery. In order to do that, the voltage is first rectified by means of a full-wave rectifier and then regulated using a DC-DC converter. In particular a buck-boost converter is used. It allows input voltages that are both lower and higher than the battery voltage to be regulated to the proper value in order to recharge the battery, as will be described in Section 3.4.1.

Finally, assuming that the power recovered from the vibration and stored into the battery does not have to be produced by the alternator anymore, there is a certain amount of mechanical power that does not have to be delivered to the alternator by the engine. This directly leads to a reduction in the fuel consumption and thus in the carbon dioxide (CO_2) emissions, for the same amount of mechanical power delivered to drive the vehicle.

3.1.2 Block diagram of the integrated model

The structure of the model is described in this section. As shown in Figure 3.1-3, the multi-body quarter car model developed with EoM tool (discussed in Section 3.3) is integrated with the dynamic model of the electromagnetic damper.

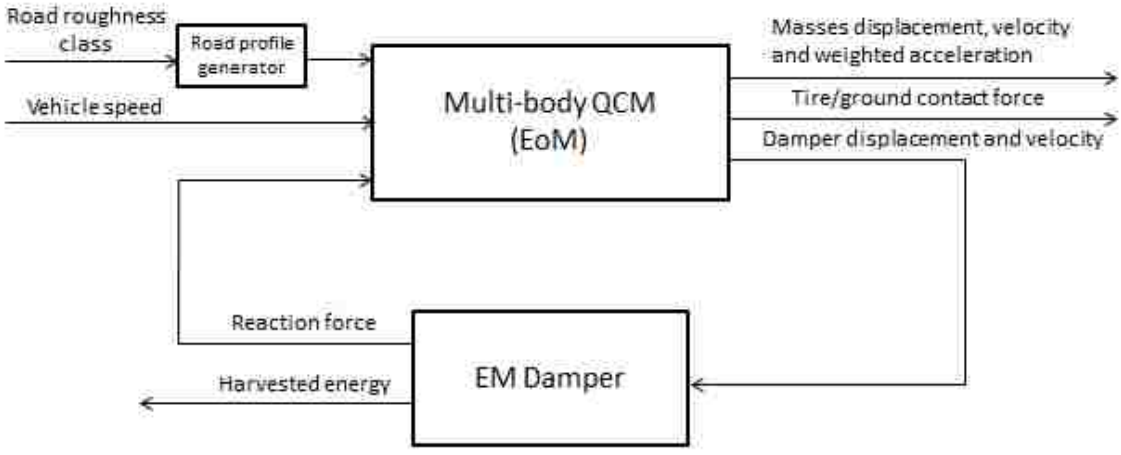

Figure 3.1-3: Block diagram of the integrated model

Once the model is set up, the user can basically select two inputs:

- The class of road roughness that needs to be analyzed;
- The vehicle speed.

The inserted class of road roughness is used to generate a random road profile according to the ISO 8606 Standard. The generated profile is actually the input (with vehicle speed) of the multi-body QCM that, by means of the equations of motion computed by EoM code, solves dynamically for the following outputs:

- Sprung mass displacement, velocity and frequency weighted acceleration;
- Tire/ground dynamic contact force;
- Relative displacement and velocity between shock absorber ends.

The latter output is introduced as input into the electromagnetic (EM) damper dynamic model. This part of the model, according to laws that regulate the behaviour of the electric machine taken into consideration, computes dynamically the following parameters:

- The reaction force exerted by the shock absorber;
- The recovered electric energy.

The reaction force computed in the EM damper model is fed back into the main multi-body QCM, as shown in Figure 3.1-3.
Finally, knowing the recovered energy, assuming that the harvested amount does not need to be produced by the alternator, and considering the alternator and the thermal engine average efficiency, the CO_2 emission reduction is computed.

3.2 Random road profiles generation

Suspensions are excited due to three reasons:

- Pitch due to vehicle acceleration and braking;
- Roll due to vehicle cornering;
- Road irregularities.

Among these causes, road irregularities are the most responsible for suspension movement. For this reason, in this work only road roughness is considered as input for the tire movement, and thus the shock absorber jounce and rebound.

In order to do that, a uniform way to define the roughness of the road profiles used as input has to be considered. In this study, the ISO 8608 Standard is taken as a reference for the classification and the generation of road profiles. The use of this standard is based on the assumption that a given road has equal statistical properties everywhere along a section to be classified. Thus, the road surface is a combination of a large number of longer and shorter periodic bumps with different amplitudes. The combination is the same whichever road section is considered [27]. The ISO 8608 Standard provides the methodologies to be applied in order to generate the road surface profile, by implementing two different procedures from data measured on site [28]. In the first one, the description of the road roughness profile is provided through the calculation of the power spectral density (PSD) of vertical displacements G_d as a function of both spatial frequency n ($n=\Omega/2\pi$ [cycles/m]) and angular spatial frequency Ω. The $G_d(n)$ and $G_d(\Omega)$ are plotted on the ordinate as a function of n and Ω in a log-log scale.

The other procedure is based on the calculation of the power spectral density of the accelerations $G_a(n)$ and $G_a(\Omega)$ of the profile in terms of slope variation of the road surface per unit of covered distance.

It is easy to pass from the first to the second method and vice versa, due to the fact that the power spectral density of vertical displacements G_d and of accelerations G_a are related by the following equations [29]:

$$G_a(n) = (2\pi n)^4 \cdot G_d(n)$$
$$G_a(\Omega) = \Omega^4 \cdot G_d(\Omega) \quad \textbf{(3.1)}$$

The Standard considered, in order to easily compare different road roughness profiles, provides a classification that is based on their PSD, calculated in correspondence of a standard value of spatial frequency (n_0=0.1 cycles/m) and angular spatial frequency (Ω_0=1 rad/m).

Table 3.2-1: ISO 8608 values of $G_d(n_0)$ and $G_d(\Omega_0)$ (n_0=0.1 cycles/m and Ω_0=1 rad/m) [29]

Road class	$G_d(n_0)(10^{-6}\ m^3)$		$G_d(\Omega_0)(10^{-6}\ m^3)$	
	Lower limit	Upper limit	Lower limit	Upper limit
A (very good)	-	32	-	2
B (good)	32	128	2	8
C (average)	128	512	8	32
D (poor)	512	2048	32	128
E (very poor)	2048	8192	128	512
F	8192	32768	512	2048
G	32768	131072	2048	8192
H	131072	-	8192	-

Eight classes of roads can be identified (from class A to class H) considering the values of $G_d(n_0)$ and $G_d(\Omega_0)$ established in ISO 8608 Standard and reported in Table 3.2-1. Looking at the value in the table, it is clear that class A includes roads that have the lowest degree of roughness possible while roads included in class H are the ones with the highest degree of roughness, so the poorest from the quality point of view. In order to have a rough and quick estimation of the roughness quality, it can be assumed that new roadway layers, such as asphalt or concrete layers have good or even very good roughness quality, old not maintained roadway layers have medium roughness, and roadway layers made of cobblestones or similar have from medium to very poor roughness quality [30].

If the class of a real roughness profile has to be identified this procedure has to be followed:

- The power spectral density of the real profile has to be calculated in correspondence of the of the reference spatial frequency and angular spatial frequency;
- The obtained values have to be compared with the limit values defined in the ISO 8608 Standard and shown in Table 3.2-1 in order to identify the class.

The Standard provides the following equations to define the roughness profile of the road surface [29]:

$$G_d(n) = G_d(n_0) \cdot \left(\frac{n}{n_0}\right)^{-2}$$

$$G_d(\Omega) = G_d(\Omega_0) \cdot \left(\frac{\Omega}{\Omega_0}\right)^{-2} \quad \textbf{(3.2)}$$

For real applications, random artificial road profiles, in agreement with the classification proposed by the ISO 8608 Standard, can be generated from a stochastic representation, in terms of the function of the PSD of vertical displacement.

Considering a continuous road profile, for a fixed value of the spatial frequency n, within a frequency band Δn, the following expression can be used in order to calculate the PSD function for the spatial frequency considered [29]:

$$G_d(n) = \lim_{\Delta n \to 0} \frac{{\Psi_x}^2}{\Delta n} \quad \textbf{(3.3)}$$

where ${\Psi_x}^2$ is the mean square value of the component of the signal for the spatial frequency n, within the frequency Δn.

The road profile signal is described as a sequence of elevation points uniformly spaced. If the length of the road profile L and the sampling interval B are considered, the maximum theoretical sampling spatial frequency $n_{max} = 1/B$ can be defined. The discretized spatial frequency values n_i are equally spaced of an interval $\Delta n = 1/L$, within the frequency domain, and the generic value n_i can be regarded as $i \cdot \Delta n$. By so doing, Eq. (3.3) can be written in the following discrete form:

$$G_d(n_i) = \frac{{\Psi_x}^2(n_i, \Delta n)}{\Delta n} = \frac{{\Psi_x}^2(i \cdot \Delta n, \Delta n)}{\Delta n} \quad \textbf{(3.4)}$$

(the index *i* varies in the interval [0 , $N=n_{max}/\Delta n$]).

The road profile can be described using a simple harmonic function as shown in the following expression:

$$h(x) = A_i \cos(2\pi \cdot n_i \cdot x + \varphi) = A_i \cos(2\pi \cdot i \cdot \Delta n \cdot x + \varphi) \quad \textbf{(3.5)}$$

where A_i is the amplitude, n_i is the spatial frequency and φ is the phase angle.

It can be demonstrated that the mean square value ${\Psi_x}^2$ of this harmonic signal is [29]:

$$ {\Psi_x}^2 = \frac{{A_i}^2}{2} \tag{3.6} $$

Thus substituting the previous equation into Eq. (3.4):

$$ G_d(n_i) = \frac{{\Psi_x}^2(n_i)}{\Delta n} = \frac{{A_i}^2}{2 \cdot \Delta n} \tag{3.7} $$

According to the literature [31], if the PSD function of vertical displacement is known, it is possible to generate a random road profile by using Eq. (3.7) considering a random phase angle φ_i that follows a uniform probabilistic distribution in the range [0,2π].
By so doing, the random road profile can be generated according to the following expression:

$$ \begin{aligned} h(x) &= \sum_{i=0}^{N} A_i \cos(2\pi \cdot n_i \cdot x + \varphi_i) = \\ &= \sum_{i=0}^{N} \sqrt{2 \cdot \Delta n \cdot G_d(i \cdot \Delta n)} \cdot \cos(2\pi \cdot i \cdot \Delta n \cdot x + \varphi_i) \end{aligned} \tag{3.8} $$

If the Eq. (3.2) is substituted into the previous one, a random artificial road profile can be generated, according to the ISO 8608 Standard:

$$ h(x) = \sum_{i=0}^{N} \sqrt{\Delta n} \cdot 2^k \cdot 10^{-3} \cdot \left(\frac{n_0}{i \cdot \Delta n}\right) \cos(2\pi \cdot i \cdot \Delta n \cdot x + \varphi_i) \tag{3.9} $$

Where x is the abscissa, thus the horizontal position along the road profile and varies from 0 to L, Δn=1/L, n_{max}=1/B, N=n_{max}/Δn=L/B, n_0=0.1 cycles/m, φ_i is a random phase angle that follows a uniform probabilistic distribution in the interval [0,2π], and k is the index that has to be varied in order to select the wanted road profile roughness class; it can assume integers from 3 to 9, that correspond to the profile from class A to class H (see Table 3.2-2). Actually, choosing an integer between 3 and 9, the limiting road profile between two classes is shown in Table 3.2-2.

Table 3.2-2: k values for ISO 8608 road roughness classification [29]

Road class		k
Upper limit	Lower limit	
A	B	3
B	C	4
C	D	5
D	E	6
E	F	7
F	G	8
G	H	9

In the following graphs, seven road profiles of a length of 1000 meters are plotted according to the seven values of the index k (reported in the previous Table). For sake of clarity, the first four road profiles are plotted in Figure 3.2-1 while the other three profiles are plotted in Figure 3.2-2. It has to be noted that the two plots have different range of values in the ordinate. This can lead to confusion in the reader but it is necessary in order to have a clear visualization of the road profile, due to the big difference between the values of the first and the last classes.

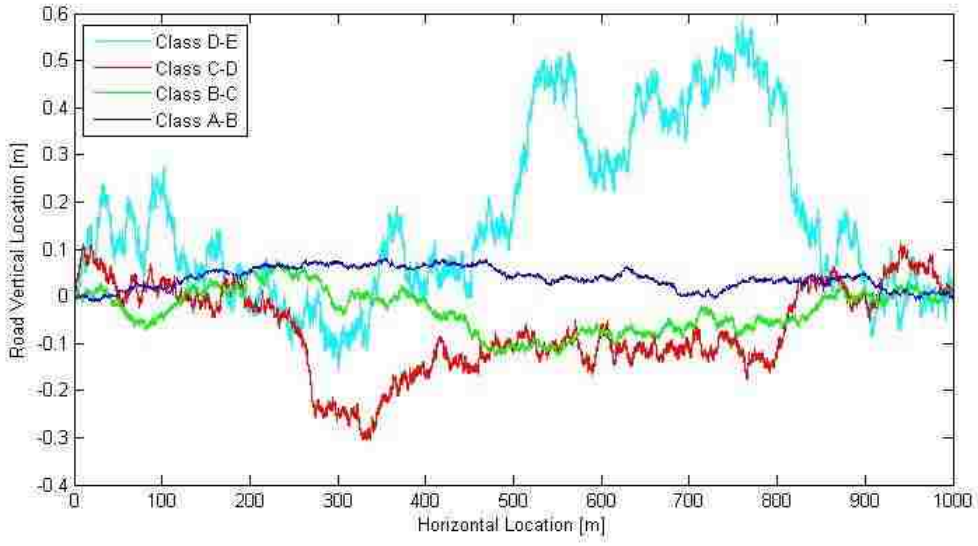

Figure 3.2-1: Random road profiles of 1km for four classes according to ISO 8608 classification

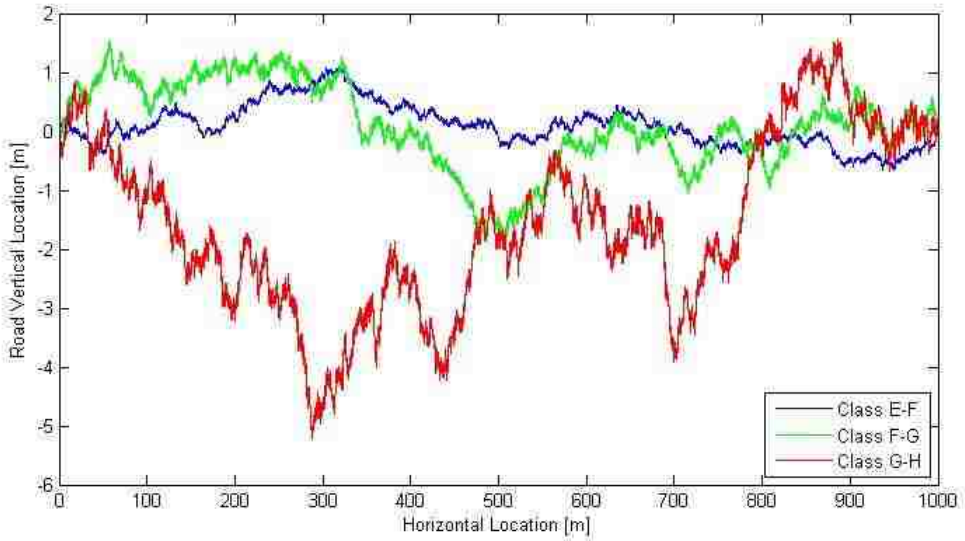

Figure 3.2-2: Random road profiles of 1km for three classes according to ISO 8608 classification

3.3 EoM

The main tool used in this project for the simulation of the suspension behaviour is EoM. EoM (Equations of Motion) is a tool developed by the Vehicle Dynamics and Control Research Group at the University of Windsor and it can be used to generate the linear or linearized equations of motion for mechanical systems. It can generate the equations of motion for a three dimensional mechanism composed of rigid bodies, and coupled by either rigid or flexible connectors.

The equations of motion generated are linearized and the EoM code gives as output the descriptor state space form of these equations, as shown below:

$$E\dot{x}(t) = Ax(t) + Bu(t)$$
$$y(t) = Cx(t) + Du(t) \quad \textbf{(3.10)}$$

where:

- $t \in \mathbb{R}$ is the time;
- $x(t) \in \mathbb{R}^n$ is the state vector;

- $u(t) \in \mathbb{R}^m$ is the input or control;
- $y(t) \in \mathbb{R}^p$ is the output;

- $A \in \mathbb{R}^{n \times n}$ is the dynamics matrix;
- $B \in \mathbb{R}^{n \times m}$ is the input matrix;
- $C \in \mathbb{R}^{p \times n}$ is the output or sensor matrix;
- $D \in \mathbb{R}^{p \times m}$ is the feedthrough matrix.

Thus using the EoM software it is possible to generate the equations of motion of the multi-body quarter car model, considering also the masses of the components of the system.

The code allows a high degree of flexibility. More or less complicate structures can be built using this code, defining an input file as described in the next section.

3.3.1 EoM input file

In order reproduce the model of the suspension considered in the EoM code, an input file is built. The file contains the definitions of each element that composes the suspension structure. All the rigid bodies are defined, together with the rigid and flexible connections that link them. Rigid points, yellow colored in Figure 3.1-2, represent the connections between the bodies. They have different shapes according to the number of forces and moments that they carry, thus depending on the degrees of freedom. Cylindrical ones allow 4 or 1 degrees of freedom. In particular, the connections between the upright and wheel, and between chassis and ground allow only a degree of freedom. The spherical shaped constraints instead transmit three forces. A flexible version of the rigid points just described is defined in order to model the tire. The stiffness and its direction are set.

Two actuators are defined in order to stand for the forces exerted on the system by the electromagnetic damper and by the road profile. Every addition of an actuator to the system corresponds to the addition of a column in the input matrix u of the state space equations described in Section 3.3. Finally, sensors are inserted in order to obtain the desired outputs described in Section 3.1.2. The addition of a sensor corresponds to the

addition of a row in the output matrix y, thus also in the sensor matrix C and in the feedthrough matrix D.

A detailed description of the way in which every item of the system is defined in the input file is provided in Appendix A.

3.4 Electromagnetic damper

This section is dedicated to the modeling of the electrical motor used as generator.

The excitation due to the road irregularities causes the ends of the shock absorber to move with respect to each other with a relative velocity *v*. The linear velocity is then converted into rotational velocity ω by means of the ball screw mechanism, with a transmission ratio τ [rad/m]. The rotational velocity is the input for the electrical generator dynamic model.

As shown in Figure 3.4-1, the generator can be modeled as an equivalent electric circuit that comprises an ideal generator, the internal resistance R_i and inductance L of the machine. The terminals of the modeled machine are shunted by a resistance R_e that accounts for the shunt resistance, if a non-regenerative electromagnetic damper is considered, or for the equivalent resistance of the electrical charging circuit, if a regenerative electromagnetic shock absorber is evaluated [16]. It is important to note that the electrical charging circuit, as described in Section 3.4.1, can be regarded as a pure resistor under moderate assumption.

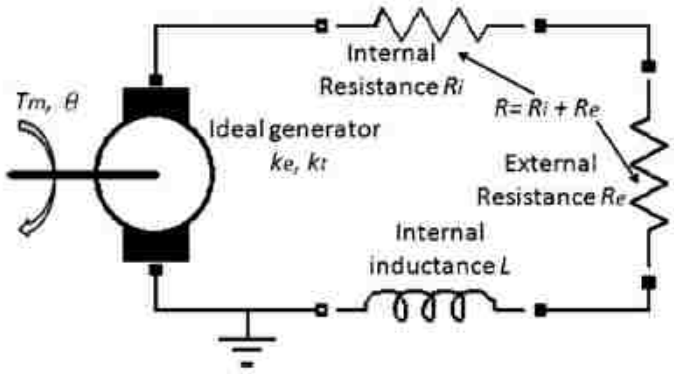

Figure 3.4-1: Dynamics modeling of the electromagnetic motor; *Re* is the equivalent resistance of the power charge circuit [16]

Applying the Kirchhoff's Voltage Law, the equation that holds for this circuit can be written:

$$V_{emf} - L\frac{di}{dt} - i(R_i + R_e) = 0 \tag{3.11}$$

The back electromotive force V_{emf} is directly related to the rotational velocity ω (and thus to the relative linear velocity) by means of the following relation:

$$V_{emf} = K_e\omega \tag{3.12}$$

where the coefficient K_e is the back electromotive force constant of the generator.
Using the Eq. (3.11) and Eq. (3.12), the electric current i induced into the generator coil is computed. This current will produce the electromechanical torque T_{em}, which counteracts the relative motion, according to the following relationship:

$$T_{em} = K_t i \tag{3.13}$$

where the coefficient K_t is the torque constant of the machine.
In the case of a brushless motor with a sinusoidal electromotive force, the back emf constant K_e and the torque constant K_t are dependent on the number of pole pairs p and on the amplitude Λ_m of the flux produced by the permanent magnets of the rotor and linked by the stator windings, according to the following relationship [26]:

$$K_t = \frac{m}{2}p\Lambda_m$$
$$K_e = p\Lambda_m \tag{3.14}$$

where m is the number of phases of the machine. In the case of a three phase machine the torque constant K_t has to be multiplied by a factor 3/2. This is due to the fact that the torque depends on the phase current and in a three phase machine there are three active phases.
A parameter that significantly influences the dynamic behaviour of the electrical machine is the rotor inertia. Although it can be regarded as a capacitor in equivalent circuits [32], in this work, it is considered as a mechanical parameter. The effect of inertia has been taken into account considering the moment of inertia of the rotating parts J that includes

both the rotor of the electric machine and the screw. The following relationship is used to compute the equivalent inertia [2]:

$$m_{eq} = \tau^2 J + m_t \tag{3.15}$$

where m_t is the mass of the translating parts and τ is the ball screw transmission ratio.

In order to perform in Matlab the calculation of the current induced in the coil, according to Eq. (3.11), the function *ode45* is used. This is a solver of ordinary differential equations (ODEs) with a medium level of accuracy that uses a variable time step.
The function that contains the electromagnetic damper model, the time interval desired, and the initial conditions are inserted as input of the *ode45* solver. It gives as outputs the time vector and a matrix containing, in the time interval considered, the values of the state variables and of the four following parameters computed in the electromagnetic damper model:

- Instant input mechanical energy, computed integrating over time the following equation:

$$\frac{dE_{mech}}{dt} = T_{em} \cdot \omega \tag{3.16}$$

- The induced current, computed solving Eq. (3.11);
- Instant output electrical energy (i.e. the energy on the resistor R_e of the circuit in Figure 3.4-1), calculated considering the value of the computed current and of the equivalent resistance R_e, thus integrating the following equation:

$$\frac{dE_{R_e}}{dt} = i^2 \cdot R_e \tag{3.17}$$

- Instant energy dissipated by the diodes of the voltage rectifier, assuming a constant voltage drop V_γ (1.1 V, selected according to the operating conditions) across the diode, computed integrating the following equation [33]:

$$\frac{dE_{diodes}}{dt} = 2 \cdot i \cdot V_\gamma \tag{3.18}$$

The mechanical input power P_{mech}, the electrical output power P_{Re}, and the power P_{diodes} dissipated by the diodes of the rectifier are thus computed dividing the respective value of energy by the considered time interval.

3.4.1 Electric charging circuit

The schematic of the electric charging circuit is shown in Figure 3.4-2. The voltage *V* that corresponds to the voltage across the external resistance R_e of Figure 3.4-1 is rectified by means of a two-halfwave rectifier.

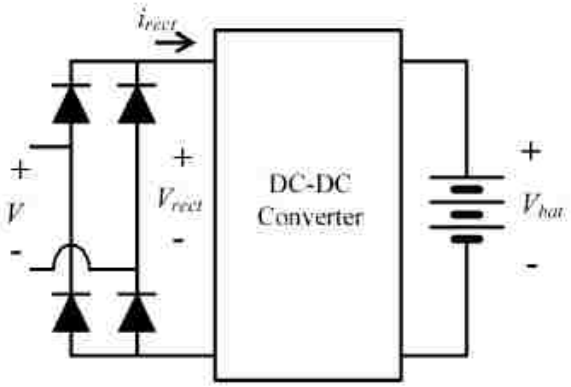

Figure 3.4-2: Schematization of the electric charging circuit [34]

The rectified voltage is then regulated by means of a DC-DC converter in order to be suitable for battery charging. In particular, the converter used for this application is a buck-boost converter, as shown in Figure 3.4-3. Using this device, simultaneous vibration control and energy harvesting are achieved. Moreover, the converter allows the input voltage to be either lower or higher than the battery voltage.

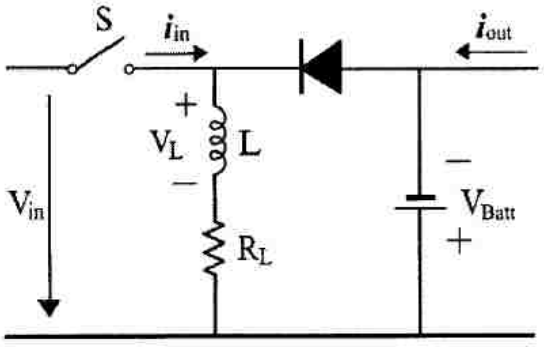

Figure 3.4-3: Schematic of a buck-boost converter [35]

As previously stated, it has been found in the literature that the buck-boost DC-DC converter can be regarded as a pure resistor if the assumption that it works in

discontinuous current mode (DCM) holds [35] [34] [36]. The equivalent resistance is related to the duty cycle and switching frequency of the pulse width modulation (PWD) of the switch. In order to increase the efficiency of the device, the output voltage of the two-halfwave rectifier may be smoothed by considering an input capacitor before the buck-boost converter.

3.4.2 Efficiencies and harvested power calculation

The section is dedicated to the calculation of the efficiencies and, finally, of the harvestable power based on the values of power computed with the procedures described so far and on the assumptions considered. First, the electrical efficiency η_e, i.e. the efficiency of the mechanical to electrical conversion by means of the PM brushless DC motor, can be calculated considering the electrical output power P_{Re} and the mechanical power P_{mech} computed as described in Section 3.4:

$$\eta_e = \frac{P_{Re}}{P_{mech} \cdot \eta_{BS}} \tag{3.19}$$

where η_{BS} is the coefficient that accounts for the ball screw mechanism efficiency. This efficiency is assumed to be 0.9 according to the average values found [37].

As it will be shown in Chapter 4, the value of the electrical efficiency η_e strongly depends on the value of the external resistance R_e, being the electrical output power the power on the resistance itself. The higher the resistance, the lower the electrical output power. This does not lead to a lower electrical efficiency, but on the contrary to an increment of η_e due to the increase of the ratio between the amount of power over the equivalent resistance and the amount of power dissipated in the rest of the circuit.

The harvested power can be computed using the following equation that considers the electrical output power P_{Re}, the power P_{diodes} dissipated by the diodes of the voltage rectifier that are always in conduction, as shown in Section 3.4, and the DC-DC converter efficiency $\eta_{DC/DC}$:

$$P_{harv} = \eta_{DC/DC} \cdot (P_{Re} - P_{diodes}) \tag{3.20}$$

Considering that the DC-DC converter efficiency $\eta_{DC/DC}$ varies slightly according to operating conditions, an average value of efficiency (0.92) is assumed in these calculations [38] [7].

Finally, the total energy conversion efficiency η_{conv} can be computed. It is a fundamental index to evaluate the harvester performance and can be calculated as the ratio between the energy recovered into the battery and the input mechanical power:

$$\eta_{conv} = \frac{P_{harv}}{P_{mech}} \tag{3.21}$$

3.5 CO_2 saving evaluation

In the previous section, the procedure followed for the computation of the harvested power has been shown. In this section, the method used to calculate the reduction of CO_2 emissions due to the implementation of the system analyzed in this project is reported.

It can be assumed that the power recovered into the battery does not need to be produced by the car alternator anymore. Because the alternator is powered by the engine, the recovery of a certain amount of power implies that the same quantity of mechanical power does not have to be produced by the engine. This leads to a reduction in the fuel consumption, thus to a decrease of the CO_2 emission in the environment.

In order to compute the CO_2 saving, the following parameters are taken into account [38]:

- The "consumption of effective power" V_{Pe} that describes the reduced fuel consumption with a reduction of the required power at a particular point of the engine map and represents the marginal engine efficiency. This parameter can be considered constant and nearly independent from engine speed if low engine loads are considered. The values of the "consumption of effective power" are reported in Table 3.5-1 for different types of engine.
- The efficiency η_{alt} of the alternator [38] [39]:

$$\eta_{alt} = 0.67 \tag{3.22}$$

- The conversion factor CF, in order to perform the conversion from (l/100km) to (gCO_2/km). The values that CF assumes for petrol and diesel type engines are shown in Table 3.5-2.

Table 3.5-1: Values of the "consumption of effective power" V_{Pe} for different types of engine [38]

Type of engine	V_{Pe} $[l/kWh]$
Petrol (V_{Pe-P})	0.264
Petrol Turbo (V_{Pe-PT})	0.280
Diesel (V_{Pe-D})	0.220

Table 3.5-2: Values of the conversion factor CF for petrol and diesel-type fuel [38]

Type of fuel	Conversion Factor [100 g/l]
Petrol (CF_P)	23.3 (=2330 gCO_2/l)
Diesel (CF_D)	26.4 (=2640 gCO_2/l)

Considering the listed parameters, the CO_2 saving S_{CO_2} expressed in [g/km] can be calculated according to the formula shown below:

$$S_{CO_2} = \frac{P_{harv} \cdot V_{Pe} \cdot CF}{\eta_{alt} \cdot v} \tag{3.23}$$

where v is the vehicle speed considered for the simulation.

3.6 Road handling evaluation

The study of the performance of the suspension includes the assessment of the road handling behaviour due to the implementation of the regenerative shock absorber considered into the analyzed suspension system. It is clear that if the wheel is subjected to severe vibrations, the contact force between the tire and the ground may be not sufficient or the wheel can even lose contact with the ground. Both cases can possibly cause the vehicle to lose control during steering, propulsion, or braking, compromising safety. For this reason road handling is considered a fundamental performance index [1].

The road handling depends on the dynamic and static contact force between the tire and ground. When the car is moving, the total tire/ground contact force is composed of:

- Static load: the force acting on the tire due to the weight of sprung and unsprung masses;
- Dynamic loads: the forces due to the additional displacement of the wheel that occurs when the car is moving.

At high dynamic force, it is more difficult to safely handle the vehicle. It is clear that, when the ratio of dynamic and static contact forces is equal or greater than 1, the wheel will lose ground contact.

According to these considerations, the road handling index is defined as the ratio between dynamic loads and static load:

$$RHI = \frac{k_t \cdot \Delta x_t}{m_{tot} \cdot g} \tag{3.24}$$

where:

- k_t is the tire stiffness;
- Δx_t is the additional tire compression due to the action of dynamic loads;
- m_{tot} is the sum of sprung and unsprung masses;
- g is the gravitational acceleration.

Because the road profiles are randomly generated, the road handling can be evaluated with a statistical quantity, which is the root mean square (RMS) value of the dynamic/static force between the tire and the ground.

In order to compute the road handling index, the following procedure is carried out. A virtual sensor is implemented, in order to measure the tire displacement due to the action of the dynamic forces. The sensor is defined as shown in Figure 6.1-7. The difference between this sensor with respect to the one described in Appendix A lies in the addition of the field ‘actuator’ that includes the road profile in the calculation of the tire displacement. Moreover, defining the field ‘gain’, it is possible to directly obtain the value of the dynamic loads as output.

With the output obtained from the sensor just described, the ratio between dynamic forces and static force is calculated and finally the root mean square value of this ratio is computed.

3.7 Ride comfort evaluation

In order to have a complete assessment of the performance of the regenerative shock absorber considered, the evaluation of the effect on ride comfort of the use of this type of system is needed. Clearly, in this work, the study of comfort is limited to the characterization of the vibration experienced by the occupants of the vehicle, without considering any other factor such as seating configuration etc.

The study of human vibration is divided into two subsets: hand/arm vibration, and whole body vibration [40]. The second subset is analyzed in this study. Moreover, the effect of the seats is not considered, removing a degree of freedom from the system; by so doing it is assumed that the occupant is subjected to the same acceleration of the sprung mass.

Additionally, in order to simplify the study, it is limited to the vertical-axis vibration of the driver, which is the dominant direction of vibration in most cases.

It is clear that ride comfort is subjective to human perception. Different physiological systems experience different vibration sensitivities. In addition, the perception of comfort is largely dependent on the expectation of the occupant or the activity in which the occupant is engaged. Experts in the field of human vibration are far from agreement in several areas but they all agree that it is not possible to establish a direct connection between vibrations and the manifestation of physiological symptoms [40]. It is just possible to suggest that a given exposure is more likely to result in the manifestation of some symptoms than others, but an absolute causal relationship between vibration and particular symptoms cannot be established.

There are several national standards (e.g., British Standard, European Directive) that have the intent to provide guidelines for the study of human whole body vibration. Among these, the most widely accepted standard is ISO 2631.

The international standard ISO 2631 specifies a method of evaluation of the effect of exposure to vibration on humans by weighting the root mean square (RMS) acceleration of the sprung mass (thus of the occupant) with human vibration sensitivity curves [41].
In order to use the weighting curves, it is necessary to make a good approximation of them using stable rational transfer functions of the form:

$$W(s) = \frac{b_m s^m + \cdots b_1 s + b_0}{s^n + \cdots a_1 s + a_0} \tag{3.25}$$

Zuo and Nayfeh [41] approximated the ISO 2631 weighting curve for vertical vibration by the following low order filter:

$$H_{2631}(s) = \frac{80.03s^2 + 989s + 0.02108}{s^3 + 78.92s^2 + 2412s + 5614} \tag{3.26}$$

In order to implement this filter in Matlab the 'tf' function is used. This function creates a continuous-time transfer function. Using the 'lsim' function, the time history of the acceleration of the sprung mass is filtered according to the low order filter of Eq. (3.26). Then the root mean square of the weighted values of the accelerations is computed, according to the well-known following expression:

$$a_{RMS} = \sqrt{\frac{({a_1}^2 + {a_2}^2 + \cdots + {a_n}^2)}{n}} \tag{3.27}$$

4 SIMULATION RESULTS AND DISCUSSION

In this chapter, the description of the simulations that are run and the results obtained are shown. The simulations are conducted for two possible applications of the electromagnetic regenerative suspension proposed in this project: on a medium size passenger car and on a SUV.

The input data used to setup the simulation are presented, followed by the results obtained using the methodologies explained in Chapter 3 and the analysis of the outcomes. The dependence of the desired outcomes on the main parameters that influence them is studied. In particular, the influence on road handling, ride comfort, and CO_2 emission reduction of the variation of vehicle speed and road roughness is analyzed. The influence of tire stiffness (that directly affects the three main outcomes proposed) is purposely not studied as it is considered a fixed parameter for a given car segment. Nevertheless the model allows the possibility to perform also this type of analysis.

The obtained results in the order in which they are presented in the chapter are listed below:

- Force-speed characteristics of the electromagnetic shock absorber for different values of equivalent resistance;
- Electrical efficiency as a function of equivalent resistance;
- Behaviour of some of the main parameters involved (damper relative speed, induced current) for a fixed vehicle speed and class of road profile roughness;
- Road handling index as a function of vehicle speed and class of road roughness;
- Weighted acceleration of the sprung mass as a function of vehicle speed and class of road roughness;
- Harvested power and CO_2 emission reduction as a function of vehicle speed and class of road roughness;
- Total conversion efficiency as a function of vehicle speed and class of road roughness.

All the listed outcomes are presented for the medium size passenger car application and then the results of the last four points also for the SUV application.

4.1 Medium passenger car application

4.1.1 Input parameters

The section is dedicated to the presentation of the parameters of the quarter car model and of the electromechanical damper used in the simulation. In Table 4.1-1, the values of masses and stiffness considered for the simulation of the suspension for the medium passenger car application are reported.

Table 4.1-1: Values of the parameters used for the quarter car model

Main parameters of the quarter car model		
Sprung mass	450	kg
Unsprung mass	30	kg
Spring stiffness	30	kN/m
Tire stiffness	150	kN/m

The system, as it is described in Section 3.1, with the values of mass and stiffness listed in the previous table, presents the following values of natural frequency: 1.0348 Hz and 9.6272 Hz.

The values of the parameters of the electromechanical damper considered for the simulations, based on the studies conducted by Amati *et al.* [2] [26], are listed in Table 4.1-2 showed below.

Table 4.1-2: List of the main parameters of the electromagnetic damper used in the simulations

Main parameters of the electromagnetic damper			
Type of motor		PM brushless DC motor	
Magnetic material type		NdFB	N42 grade
Internal resistance	R	3.65	Ω
Inductance	L	0.0109	H
Torque constant	K_t	1.242	Nm/A
Back emf constant	K_e	0.828	Vs/rad
Screw pitch	$1/\tau$	30	mm/rev
Moment of inertia of rotor	J	101	kg mm^2
Equivalent mass	m_{eq}	28.1	kg

The mass of the system, calculated by Amati *et al.* using a CAD model, is estimated to be of 5 kg. Moreover, the authors provided a detailed procedure for the design of the electromechanical damper [2].

4.1.2 Equivalent resistance selection

Taking into account the circuit shown in Section 3.4, it is clear that the force-to-speed characteristic of the device is strongly dependent on the value of the equivalent resistance. The behaviour of this characteristic for different values of equivalent resistance is plotted in Figure 4.1-1. As expected, higher values of equivalent resistance correspond to lower level of damping.

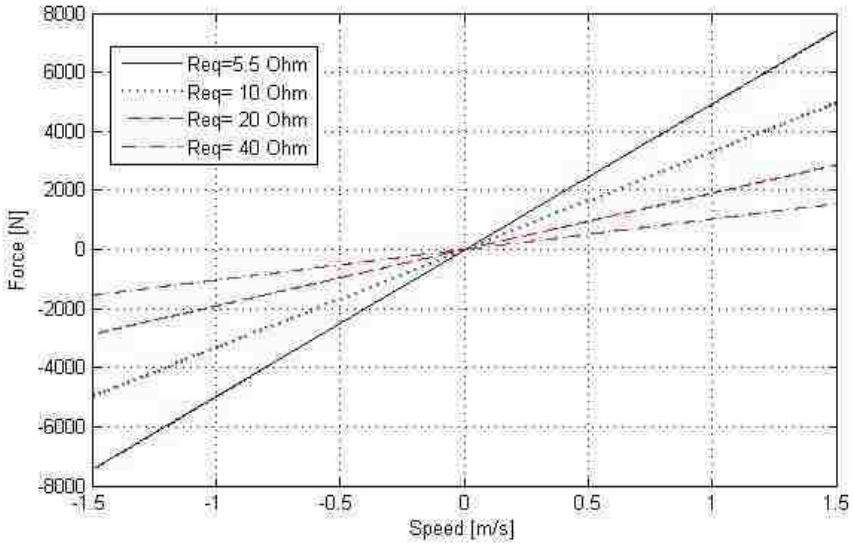

Figure 4.1-1: Force-to-speed characteristic of the electromagnetic damper for different values of equivalent resistance

In addition, it has to be noted that the value of the equivalent resistance has also a strong influence on the efficiency of the mechanical-to-electrical conversion calculated as the output electrical power on the equivalent resistance over the input mechanical power of the electrical machine. The electrical efficiency as a function of the equivalent resistance, calculated in the case of fixed vehicle speed (36 km/h) and road profile roughness (class C-D), considered as an average case, is plotted in Figure 4.1-2.

Considering that a damping coefficient of 1800 Ns/m is requested for the application taken into consideration, the selected value of the equivalent resistance is 20 Ω.

According to the plot shown in Figure 4.1-2, it corresponds to an electrical efficiency $\eta_e = 0.6$.

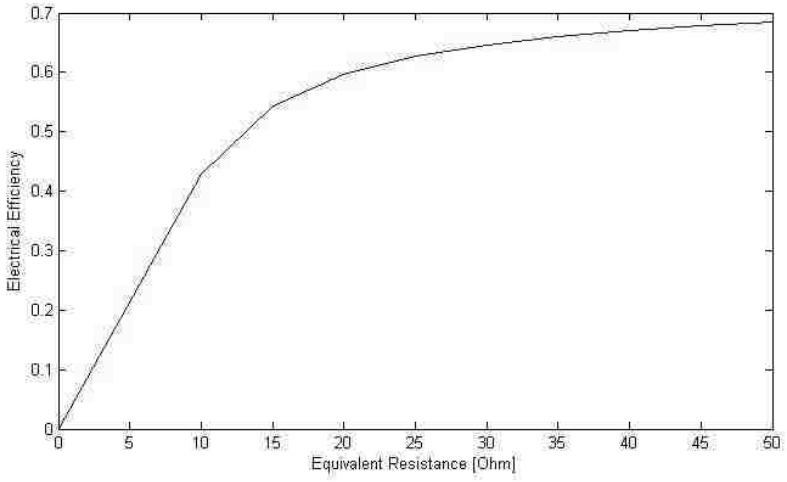

Figure 4.1-2: Electrical efficiency as a function of equivalent resistance (vehicle speed=36 k/h, road roughness class=CD)

4.1.3 Main parameter behaviour for fixed vehicle speed and road class

The section is dedicated to the presentation of some of the main parameters involved in the calculation of the desired output for a single case in which vehicle speed and class of road roughness are fixed. The detailed description of the behaviour of each parameter for fixed values of the two main inputs is reported in order to make the reader conscious of the way in which the final outcomes, which will be shown in the following section as a function of speed and road class, are computed. An average case is selected in order to be indicative of the behaviour of the shown parameters. The chosen values are:

- Vehicle speed: 36 km/h;
- Class of road roughness: C-D.

According to the road class selection, the road profile shown in Figure 4.1-3 is considered as input for the suspension movement.

The presented road profile causes the ends of the shock absorber to move one with respect to the other with the relative velocity that is plotted in Figure 4.1-4. For the class of roughness selected for this simulation, the shock absorber relative speed does not exceed 0.5 m/s.

The back electromotive force has the same trend of the shock absorber relative velocity shown in Figure 4.1-4, according to the relations presented in Section 3.4.

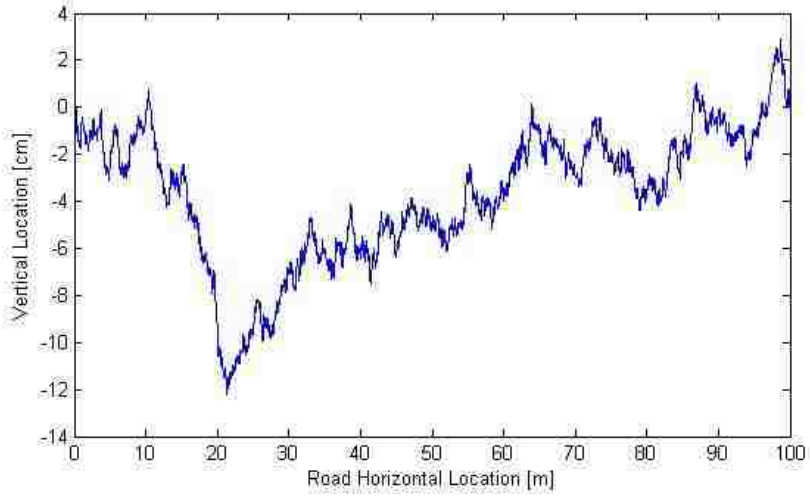

Figure 4.1-3: Random road profile of a C-D class of roughness

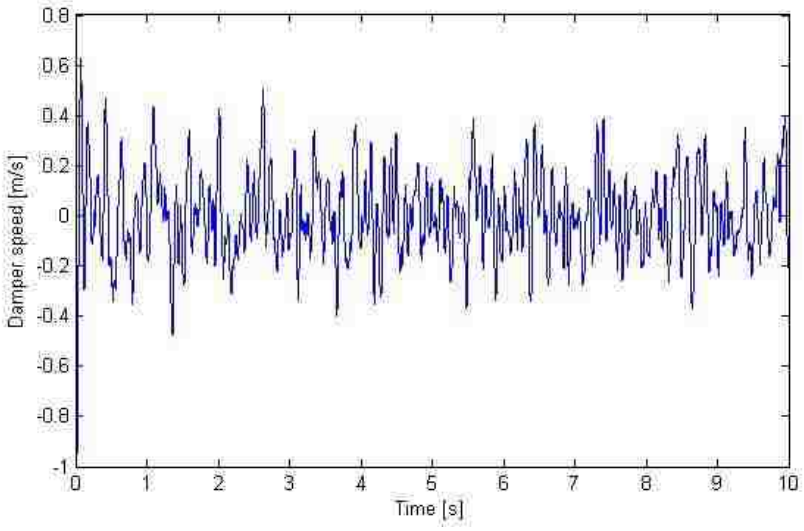

Figure 4.1-4: Relative velocity between the two ends of the shock absorber

As the back electromotive force is calculated, the induced current can be computed solving the differential equation (3.11). The values obtained by this calculation are shown in the plot of Figure 4.1-5.

The trends of the reaction torque exerted by the electrical machine and thus of the force exerted by the shock absorber are the same as the one of the current and thus are not reported in this context.

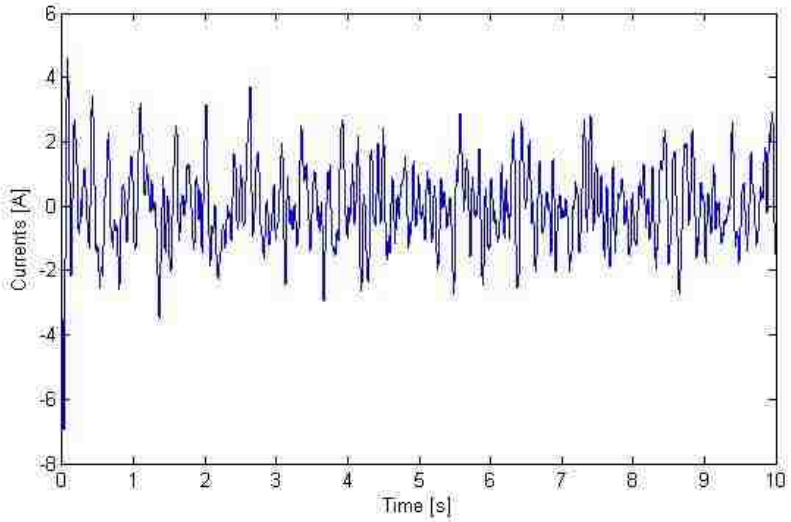

Figure 4.1-5: Current induced into the generator coil

In order to assess the road handling for these particular conditions, the dynamic tire/ground contact force is plotted. According to the explanations given in Section 3.6, the root mean square (RMS) value of the ratio between dynamic and static tire/ground force can be computed in order to obtain the road handling index. This is made possible by the fact that the road profile is randomly generated.

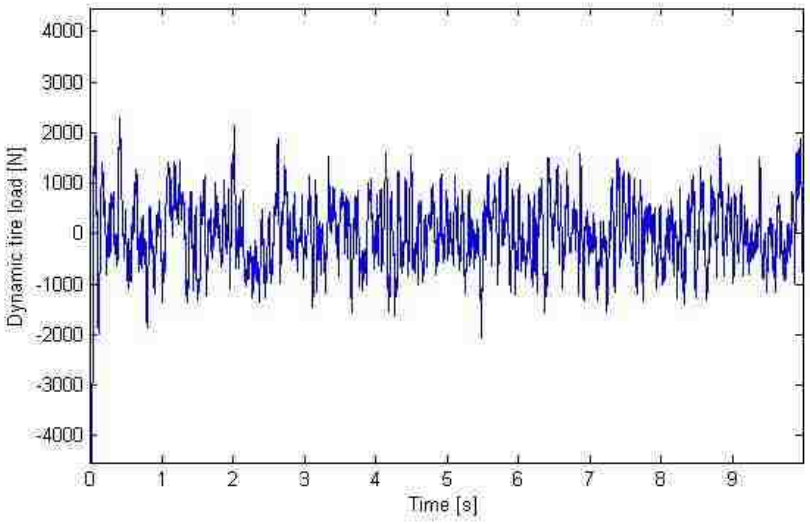

Figure 4.1-6: Dynamic tire/ground contact force [N]

The value of the road handling index calculated for this case is 0.1479. It has to be noted that this value is well below the threshold 1, which means the detachment of the tire from the ground. This observation could have been done by looking at the plot of the dynamic

tire/ground force of Figure 4.1-6 where it can be noted that the maximum values of force rarely exceed 2000 N, which is less than half of the static load (sum of sprung and unsprung masses times the gravitational acceleration).

For the evaluation of the ride comfort, the acceleration of the sprung mass over the time is recorded. These values are weighted with human vibration sensitivity curves and the plot in Figure 4.1-7 is obtained. The RMS is then computed for the same considerations done for the road handling index and 0.972 m/s^2 is obtained.

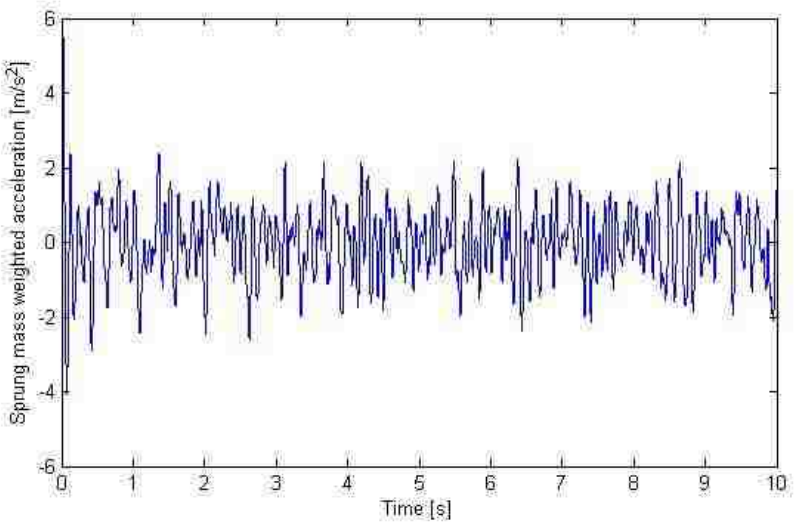

Figure 4.1-7: Sprung mass weighted acceleration [m/s^2]

Finally, with the ultimate aim to compute the CO_2 emissions reduction, the output electrical energy on the equivalent resistance is plotted as a function of time in Figure 4.1-8. The average power, calculated dividing the maximum energy value by the time interval, is 30.38 W. Following the procedure described in Section 3.4.2 and 3.5, the values of harvested power, total conversion efficiency, and CO_2 saving are computed and reported in Table 4.1-3.

Table 4.1-3: Harvested power, total efficiency, and CO_2 saving (vehicle speed 36 km/h, road class C-D)

Harvested power	25.84	W
Total conversion efficiency	0.479	
CO_2 emission reduction	2.79	gCO_2/km

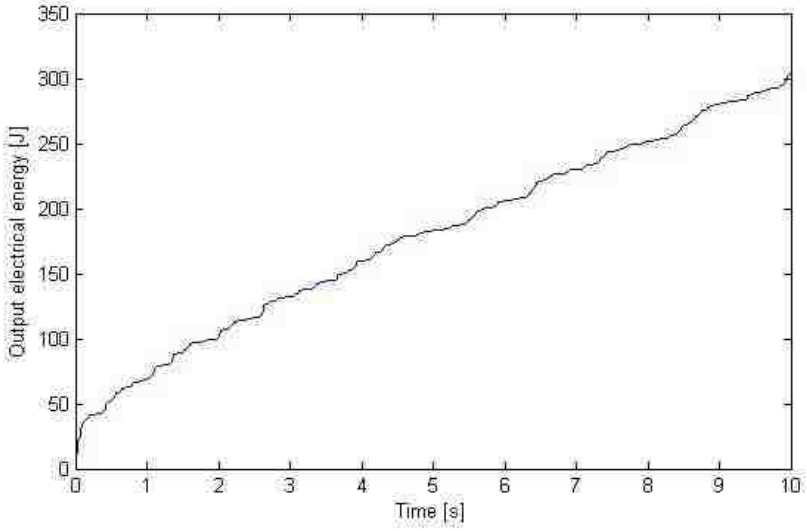

Figure 4.1-8: Output electrical energy over the equivalent resistance as a function of time

4.1.4 Road handling index

The section is dedicated to the presentation of the results obtained in the computation of the road handling index (RHI), following the procedure explained in Section 3.6. The simulations are conducted for 20 different values of vehicle speed, in the range 0–144 km/h. From now on only the results obtained for the first four classes of road roughness will be shown because they are considered the most meaningful according to the actual road profiles.

In Figure 4.1-9, the obtained values of the road handling index for the classes from A-B to D-E are plotted. It is evident that the index, which is the RMS of the ratio of the tire dynamic over tire static forces, increases as the vehicle speed increases. The same tendency can be noted for the increase of the roughness of the road. This means that, as expected, the higher the speed or the rougher the road, the higher is the risk to have the detachment of the tire from the ground with the related issues in terms of handling and safety. Nevertheless, it has to be underlined that, even at the maximum speed and for the higher class of road roughness considered in the simulation, the value of the road handling index is well below 1, which corresponds to dynamic force equal to static, thus the limit value for the detachment of the tire from the ground.

In order to better understand the values shown in Figure 4.1-9, the results obtained per each class of roughness as a function of speed are compared to the values obtained performing the same analysis but considering a conventional shock absorber with a linear damping coefficient of 1800 Ns/m. It has to be clear that higher RHI denotes worse handling performance. In addition, it must be underlined that the model generates a new random road profile for each point that is present in the plots shown below. This explains the variable behaviour of the plotted parameters.

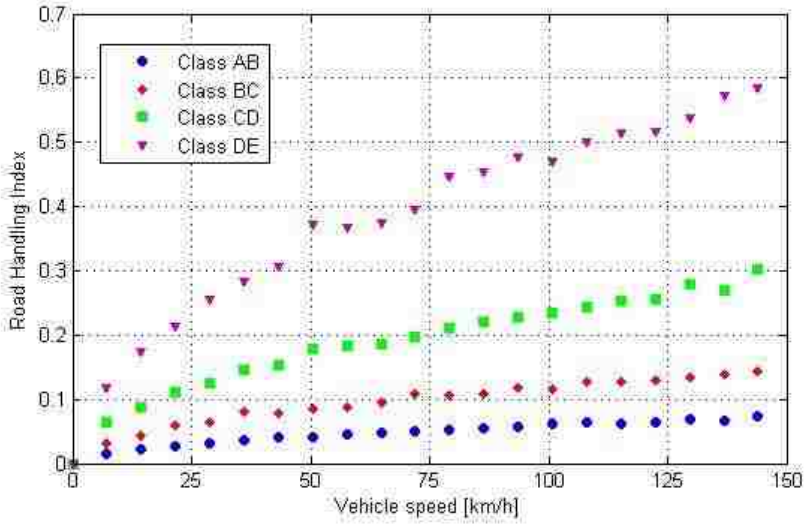

Figure 4.1-9: Road handling index as a function of vehicle speed for four classes of road roughness

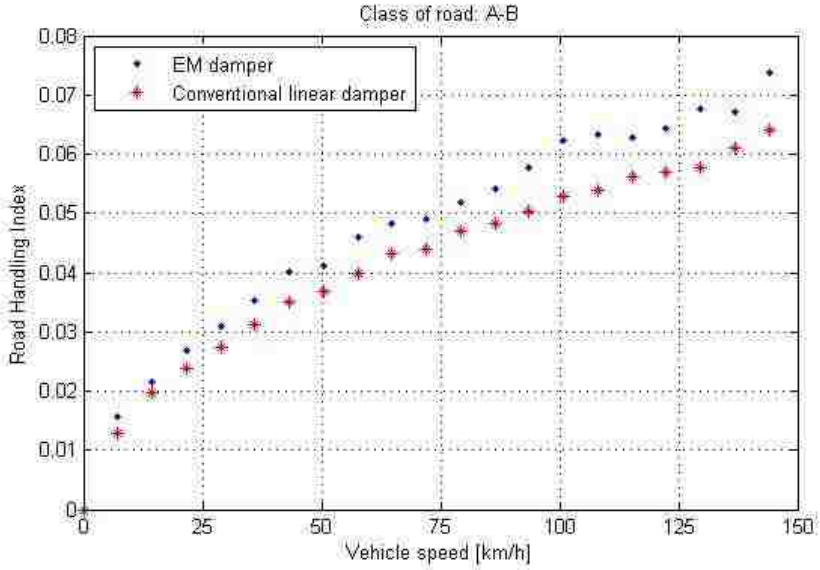

Figure 4.1-10: Road handling index as a function of vehicle speed for A-B class road: comparison between the values obtained with the electromagnetic damper and a conventional one (1800 Ns/m)

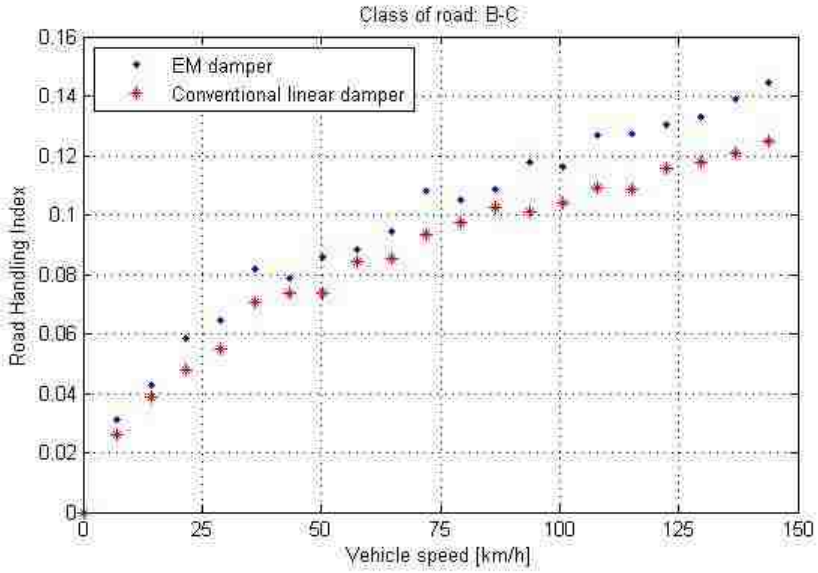

Figure 4.1-11: Road handling index as a function of vehicle speed for B-C class road: comparison between the values obtained with the electromagnetic damper and a conventional one (1800 Ns/m)

Keeping in mind this consideration, Figure 4.1-10-13 show that the implementation of the regenerative shock absorbers results in a slight worsening of the handling performance.

Referring to the plot in Figure 4.1-10, regarding the RHI for the A-B class, the suspension equipped with the electromagnetic damper appears to have 13.7% less handling performance with respect to the suspension equipped with the linear conventional damper. The value is calculated by averaging the percentages of the difference between the two RHIs with respect to the index calculated for the conventional damper.

Performing the same evaluation for the other three cases, the gap of performance between the two shock absorbers decreases slightly with the increment of the road roughness. As a matter of fact a performance deterioration of 13.6%, 13.0%, and 12.8% is calculated for the B-C, C-D, and D-E classes respectively. In conclusion, according to the RHI, the use of the electromagnetic shock absorber causes an average worsening of the suspension performance of 13.3%.

The main reason of the deterioration of the performance in the case of the electromagnetic shock absorber installation is related to the inertia of the rotating parts that compose the EM damper. This leads to higher dynamic forces at the tire/ground contact, thus to the decrease of the road handling.

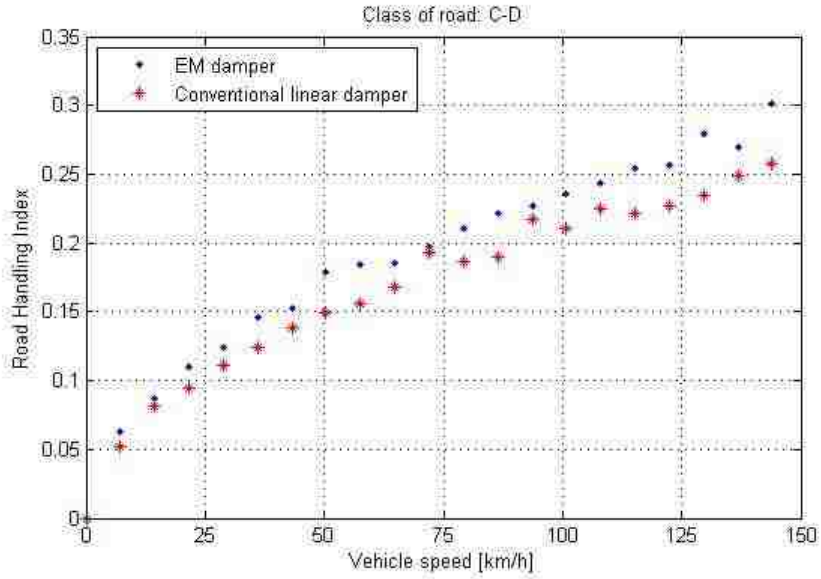

Figure 4.1-12: Road handling index as a function of vehicle speed for C-D class road: comparison between the values obtained with the electromagnetic damper and a conventional one (1800 Ns/m)

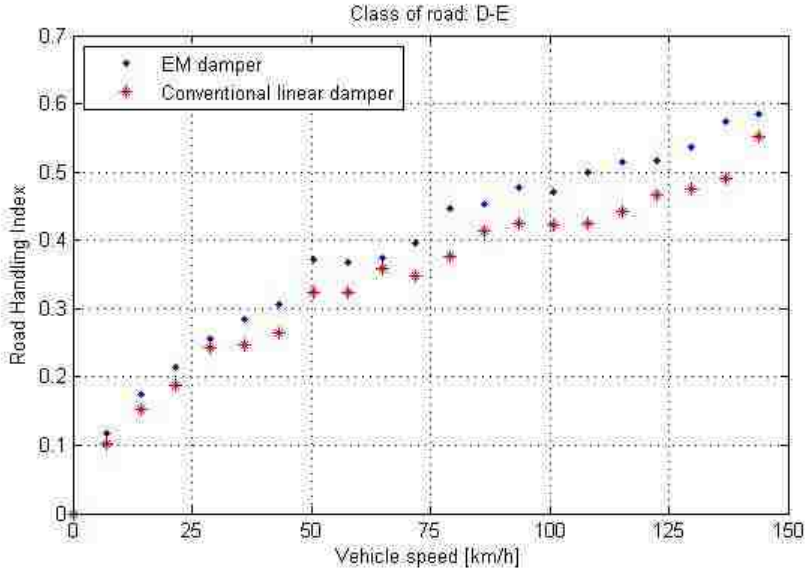

Figure 4.1-13: Road handling index as a function of vehicle speed for D-E class road: comparison between the values obtained with the electromagnetic damper and a conventional one (1800 Ns/m)

4.1.5 Ride comfort

In this section the results obtained for the ride comfort analysis are reported. The procedure described in Section 3.7 is followed and the simulations are run for the same condition already explained in the previous section: 20 speeds in the range 0 - 144 km/h and the first four classes of roughness.

In Figure 4.1-14, the RMS of the accelerations of the sprung mass (i.e. of the occupants under the assumption that they are is subjected to the same acceleration of the sprung mass) weighted by the human vibration sensitivity curves are plotted. It can be noticed that the plot has basically the same trend of the RHI shown in Figure 4.1-9 and the same considerations can be done. As expected, the level of comfort decreases with the increase of vehicle speed and road roughness.

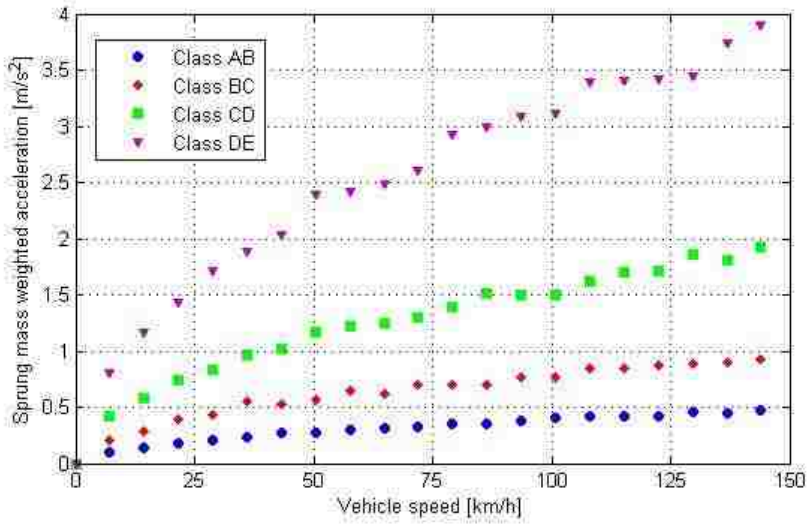

Figure 4.1-14: Sprung masses weighted acceleration as a function of vehicle speed for four classes of road roughness

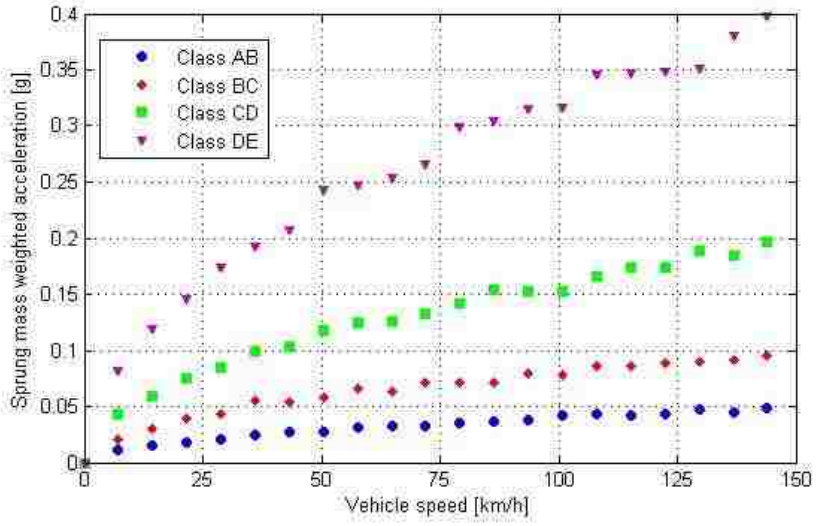

Figure 4.1-15: Sprung mass acceleration expressed in g units as a function of vehicle speed for four classes of road roughness

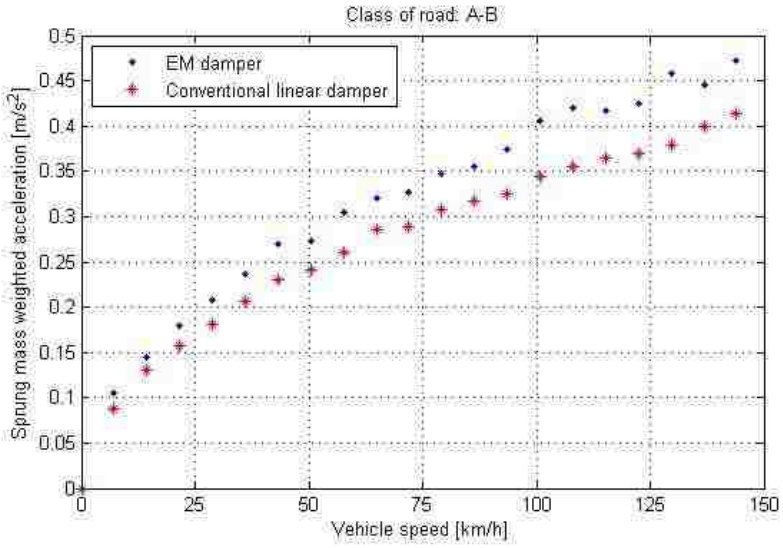

Figure 4.1-16: Sprung masses weighted acceleration as a function of vehicle speed for A-B class road: comparison between the values obtained with the electromagnetic damper and a conventional one (1800 Ns/m)

Moreover, in order to have a more direct understanding of the magnitude of the accelerations involved in the discussion, they are also plotted in Figure 4.1-15 in g units. Considering the magnitude of the sprung mass weighted accelerations, the direct comparison between the values obtained using the electromagnetic shock absorber and those obtained using the conventional linear damper is performed for each class of road roughness, in order to assess the difference in performance of the two solutions.

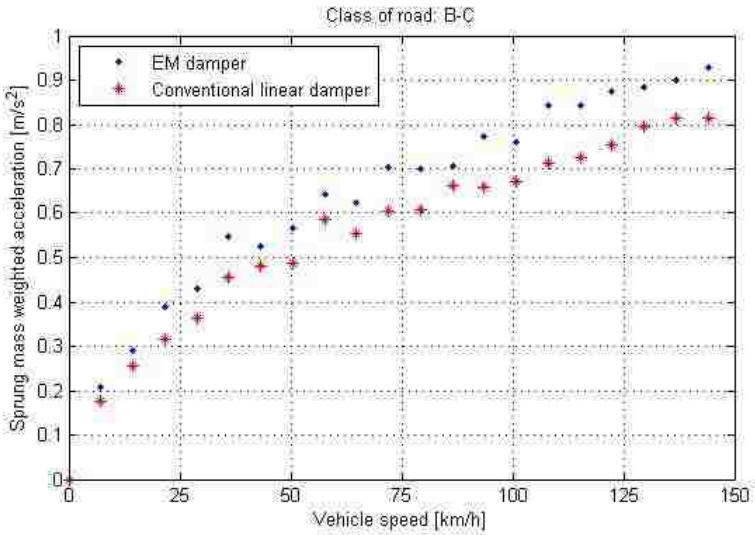

Figure 4.1-17: Sprung masses weighted acceleration as a function of vehicle speed for B-C class road: comparison between the values obtained with the electromagnetic damper and a conventional one (1800 Ns/m)

Performing the same analysis conducted for the road handling index, and remembering that the results are affected by the variation due to the randomness of the generated road profiles, it can be stated that the decrease of the ride comfort level by implementing the electromagnetic shock absorber essentially follows the trend observed for the RHI.

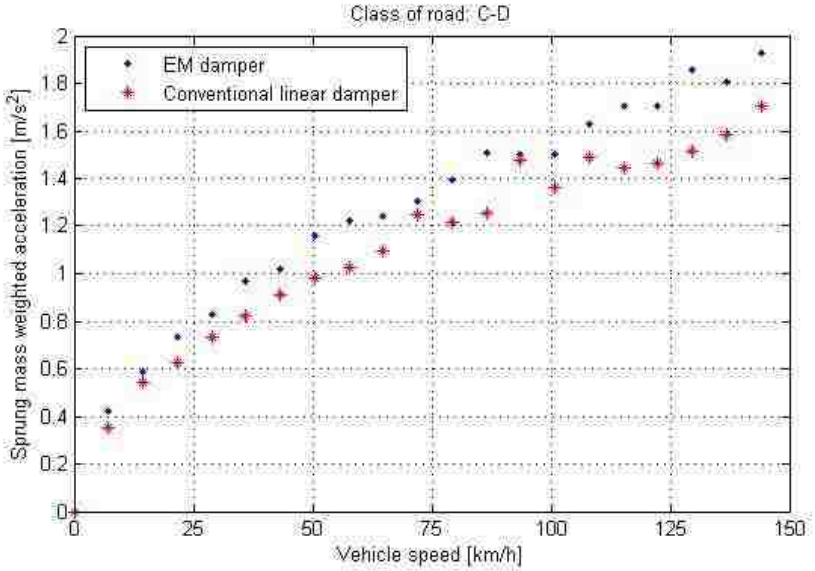

Figure 4.1-18: Sprung masses weighted acceleration as a function of vehicle speed for C-D class road: comparison between the values obtained with the electromagnetic damper and a conventional one (1800 Ns/m)

The percentage value of increase of the sprung mass acceleration for the electromagnetic damper with respect to the acceleration for the linear damper (taken as reference) slightly decreases as the road become rougher. The ride comfort performance decreases of 14.9% for the A-B class, 14.7% for the B-C class, 14.1% for the C-D class, and 13.9% for the D-E class. The average value of deterioration of the suspension ride comfort performance is calculated to be 14.4%. Again, the reason for the decreased performance of the suspension provided with the electromagnetic damper has to be assigned mainly to the high value of the equivalent mass due to the inertia of the rotating parts of the shock absorber.

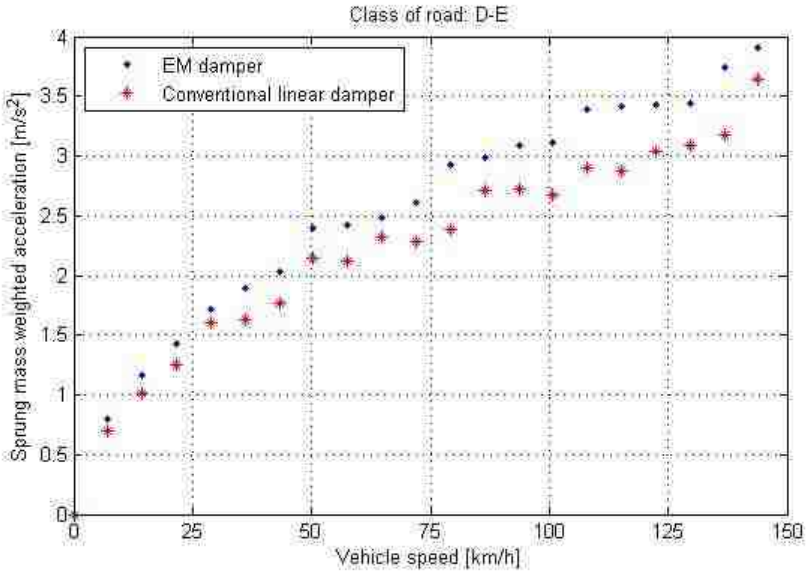

Figure 4.1-19: Sprung masses weighted acceleration as a function of vehicle speed for D-E class road: comparison between the values obtained with the electromagnetic damper and a conventional one (1800 Ns/m)

4.1.6 Conversion efficiency, harvested power and CO_2 saving

In this section, the results obtained for total conversion efficiency, power recovered in the battery and CO_2 emissions reduction are presented. The simulations are run for the same vehicle speed interval and the same classes considered in the previous section.

The results obtained for the total conversion efficiency, calculated as the ratio between the harvested power and the input mechanical power, are plotted in Figure 4.1-20 as a function of vehicle speed. It is clear that the efficiency gets higher (up to 51%) for increasing values of road roughness. Moreover, it can be noted that there is a speed threshold over which it is almost independent from the vehicle speed. This threshold gets lower with the increase of the road roughness (around 25 km/h for the D-E class). In the case of road profiles with lower roughness, the conversion efficiency appears to be more influenced by the speed and smoothly increases with it. It has to be underlined that the range of conversion efficiencies, as can be observed in the plot, comprises values from 17% to 51%, and the interval is much narrower as the road roughness increases.

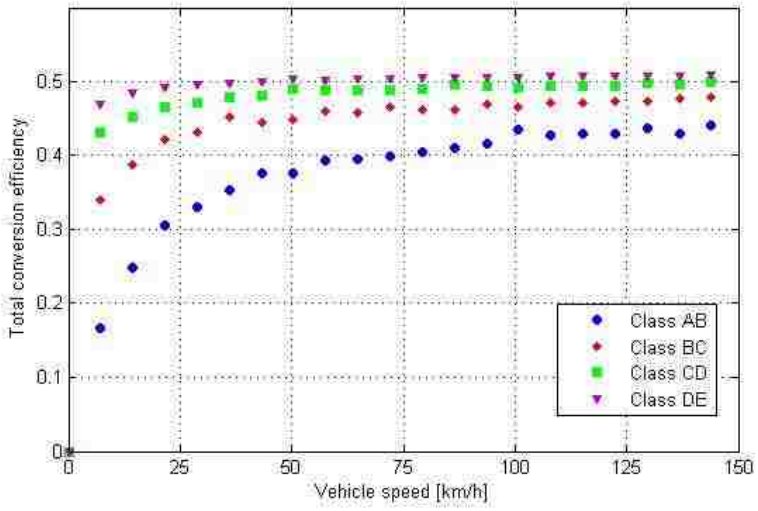

Figure 4.1-20: Total conversion efficiency as a function of vehicle speed for four classes of road roughness

In order to assess the amount of power that does not need to be produced by the alternator with the implementation of the system studied in this work, the amount of recovered power is plotted in Figure 4.1-21 as a function of vehicle speed for the four classes considered. As expected, and in accordance with the literature, the power harvested in the battery increases with the increment of forward speed as well as with the increase of the road roughness.

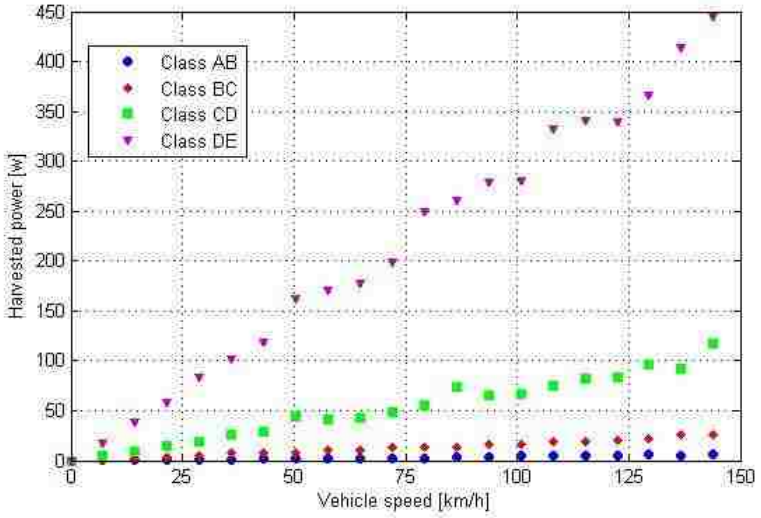

Figure 4.1-21: Harvested power as a function of vehicle speed for four classes of road roughness

As can be noticed from the plot, passing from a class to the next (higher) one, the amount of harvested power is four times the one observed for the previous class. The reason for this trend of the recovered power has to be attributed to the fact that the power spectral

density of vertical displacement used in the generation of the road profiles are scaled of a factor of four, as it is clear looking at Table 3.2-1 of Section 3.2.

The results obtained applying the procedure for the calculation of the CO_2 emission reduction presented in Section 3.5 are now shown. The plot in Figure 4.1-22 shows the estimated amount of carbon dioxide not emitted into the environment due to the implementation of regenerative shock absorbers on a vehicle equipped with a gasoline turbocharged engine for the four classes of road considered. It has to be noted that all the values of CO_2 savings reported either in the plot or in the following tables are referred to four shock absorbers, in order to have the assessment of the possible savings for the entire vehicle (the parameters shown so far were referred to a single shock absorber).

Although the harvested power is directly related to vehicle speed, the CO_2 emission reduction is independent from it, as can be notice in Figure 4.1-22. As a matter of fact, the amount of CO_2 is expressed in g/km, thus the increase of speed, which causes the recovery of a higher amount of power, has no effect of the on the CO_2 savings. This happens because the higher the vehicle speed, the lower amount of time is needed to drive over a fixed distance.

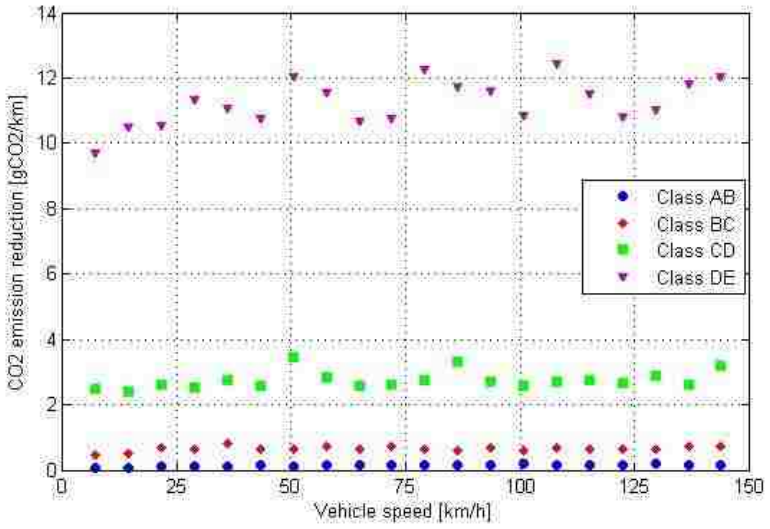

Figure 4.1-22: CO_2 savings as a function of vehicle speed for the four classes considered for a gasoline turbocharged engine (four shock absorbers)

The oscillations of the values of CO_2 are thus mainly due to the randomness of the generated road profile. For each simulation, a new random road profile is generated according to the class selected by the user; so even choosing the same road class, the

generated profiles will be always different, causing the slight variability in the output values, as can be noticed in Figure 4.1-22.

For sake of clarity, the obtained CO_2 values are reported in the tables below for the four classes of road considered. As already mentioned, the calculations are performed for a gasoline, a turbocharged gasoline, and a diesel engine.

Looking at the reported values, it is clear that the same considerations done for the harvested power are valid also in this case. As a matter of fact, the CO_2 saving basically increases by a factor of four going from a certain class to a higher one.

Table 4.1-4: CO_2 savings for a gasoline engine equipped vehicle for the four classes considered

CO_2 emission reduction (4 dampers) – Gasoline engine				
Road class	**Min. value**	**Max. value**	**Average**	**Unit**
A-B	0.06	0.18	0.13	gCO_2/km
B-C	0.45	0.78	0.62	gCO_2/km
C-D	2.28	3.25	2.59	gCO_2/km
D-E	9.14	11.71	10.61	gCO_2/km

Table 4.1-5: CO_2 savings for a gasoline turbocharged engine equipped vehicle for the four classes considered

CO_2 emission reduction (4 dampers) – Gasoline turbocharged engine				
Road class	**Min. value**	**Max. value**	**Average**	**Unit**
A-B	0.06	0.19	0.13	gCO_2/km
B-C	0.47	0.82	0.65	gCO_2/km
C-D	2.42	3.45	2.75	gCO_2/km
D-E	9.70	12.42	11.25	gCO_2/km

Table 4.1-6: CO_2 savings for a diesel engine equipped vehicle for the four classes considered

CO_2 emission reduction (4 dampers) – Diesel engine				
Road class	**Min. value**	**Max. value**	**Average**	**Unit**
A-B	0.05	0.17	0.12	gCO_2/km
B-C	0.42	0.73	0.58	gCO_2/km
C-D	2.15	3.07	2.45	gCO_2/km
D-E	8.63	11.06	10.02	gCO_2/km

Considering the magnitude of the average savings for each class, it is clear that the on-vehicle application of this type of system might be worthwhile in particular for vehicles

that are meant to be driven on roads that belong to the classes C-D and D-E. For these two classes, if an average CO_2 emission of 190 g/km is considered, the savings obtained are in the order of 1.4% and 5.4% respectively.

4.2 SUV application

The outcomes shown in the last three sections are now proposed in the case of the application of the electromagnetic shock absorber on a SUV. Some of the input parameters listed in Section 4.1.1 are modified according to the considered application and are presented in Table 4.2-1.

Table 4.2-1: Parameters used for the quarter car model for the SUV application

Main parameters of the quarter car model		
Sprung mass	625	kg
Unsprung mass	30	kg
Spring stiffness	42	kN/m
Tire stiffness	300	kN/m

The natural frequencies of the system with the parameters indicated in the previous table are: 1.0653 Hz and 13.345 Hz.

The equivalent resistance of the electric charging circuit has to be changed to be adapted to the new application. In order to obtain the desired damping of 5000 Ns/m, which is a usual value for vehicles of the chosen category [16], referring to the plot in Figure 4.1-1, the selected equivalent resistance is 5.5 Ω. With this value of resistance, considering the equivalent circuit of the electrical generator in Figure 3.4-1 and the value of the internal resistance of the machine (3.65 Ω), it is clear that the electrical efficiency will be lower with respect to the previously considered case.

Considering these changes in the model setup, in the following sections the desired outcomes, i.e. road handling, ride comfort, and CO_2 emissions reduction as a function of vehicle speed and road roughness, are reported.

4.2.1 Road handling index

The same type of analysis is performed for this new case in order to evaluate the road handling performance of the suspension with the modified parameters. The simulations are run for the same speed interval and road roughness classes. The results, shown in

Figure 4.2-1, show values of the road handling index very similar to those calculated for the medium passenger car application. Nevertheless, the comparison performed between the road handling of the electromagnetic shock absorber and the conventional linear damper with a constant damping coefficient of 5000 Ns/m shows that the worsening of the performance for this new application is much lower with respect to the previous one. The plots with the comparison of the RHI for the road classes considered are reported in Appendix B. They show an average increase of the RHI for the electromagnetic damper case of 7.3% with respect to conventional damper RHI. The reason for this result clearly lies in the fact that the effect of the inertia of the rotating parts of the shock absorber is reduced with respect to the previous case due to the higher value of the sprung mass selected for this simulation.

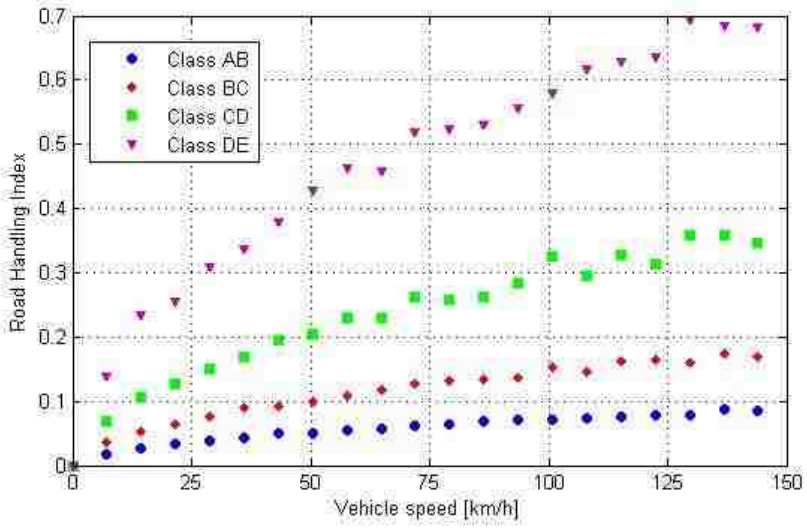

Figure 4.2-1: Road handling index as a function of vehicle speed for four classes of road roughness

4.2.2 Ride comfort

The ride comfort performance analysis for the suspension now considered is performed considering the same parameters shown in Section 4.1.5. The acceleration of the sprung mass weighted with the human vibration sensitivity curves is plotted in Figure 4.2-2 as a function of speed for different classes of road roughness. The obtained values are slightly higher than in the medium size passenger car case, as can be also noticed by looking at the plot in Figure 4.2-3 that represents the same quantities in "g" units. As for the case of the road handling index, also for the ride comfort, analyzing the plots presented in

Appendix B, it can be stated that the worsening of the performance due to the replacement of the conventional damper with the proposed system is reduced to 5.1%.

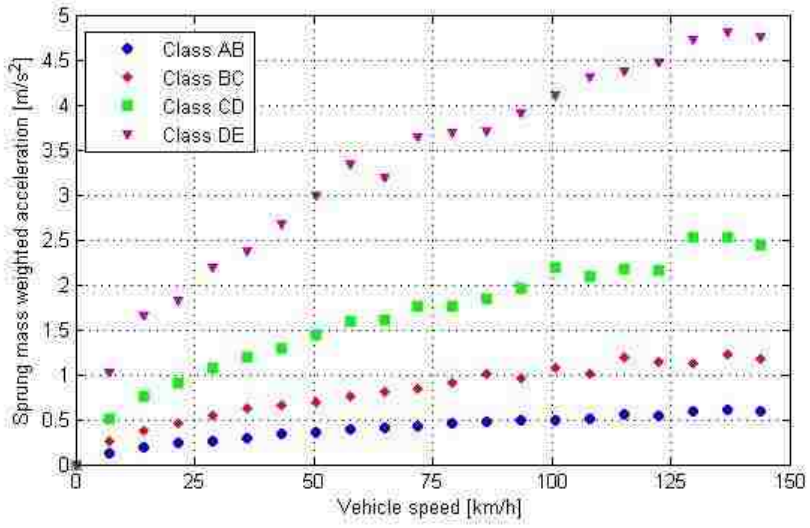

Figure 4.2-2: Sprung masses weighted acceleration as a function of vehicle speed for four classes of road roughness

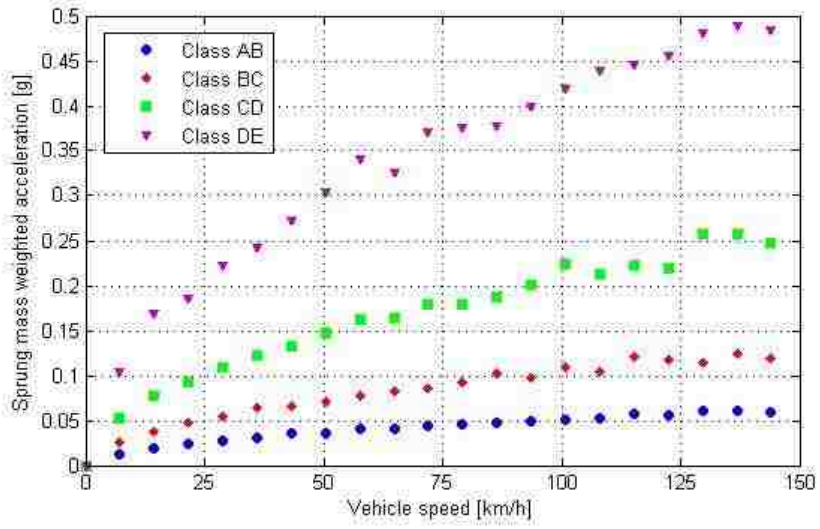

Figure 4.2-3: Sprung mass acceleration expressed in g units as a function of vehicle speed for four classes of road roughness

4.2.3 Conversion efficiency, harvested power and CO_2 saving

In the section, the results obtained for total conversion efficiency, harvested power, and CO_2 emission reduction for the SUV application are presented.

Considering the conversion efficiencies plotted in Figure 4.2-4, it is clear that they follow the same trend of the efficiencies shown in Figure 4.1-20 for the first case. However it must be noted that the maximum value in this application is 36%, 30% lower than the

maximum value obtained for the previous case. The reason for the decreased efficiency is to be addressed to the magnitude of the equivalent resistance selected in this case (almost ¼ of the previous one), which strongly affects the electrical efficiency.

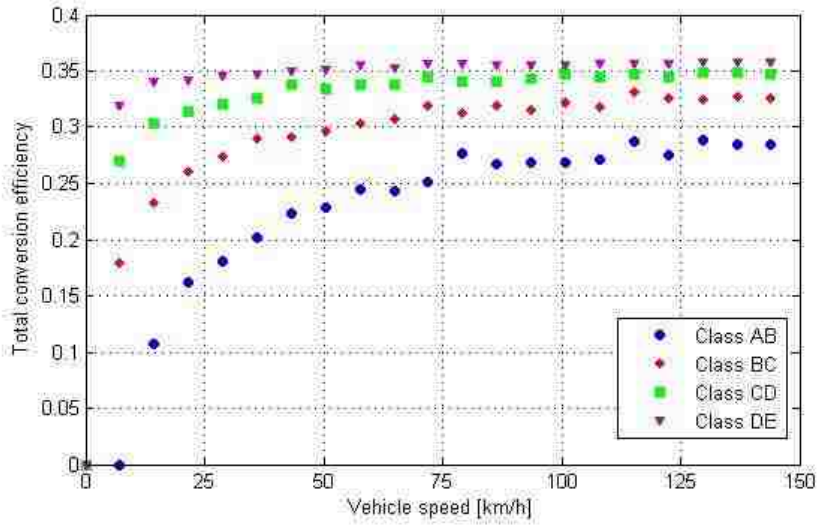

Figure 4.2-4: Total conversion efficiency as a function of vehicle speed for four classes of road roughness

The power recovered into the battery for the usual conditions of speed and roughness is plotted in Figure 4.2-5. It can be noticed that the harvested power is almost doubled with respect to the medium size passenger car case. This result can be explained by the fact that the value of tire stiffness inserted in the model for this case is doubled with respect to the previous case.

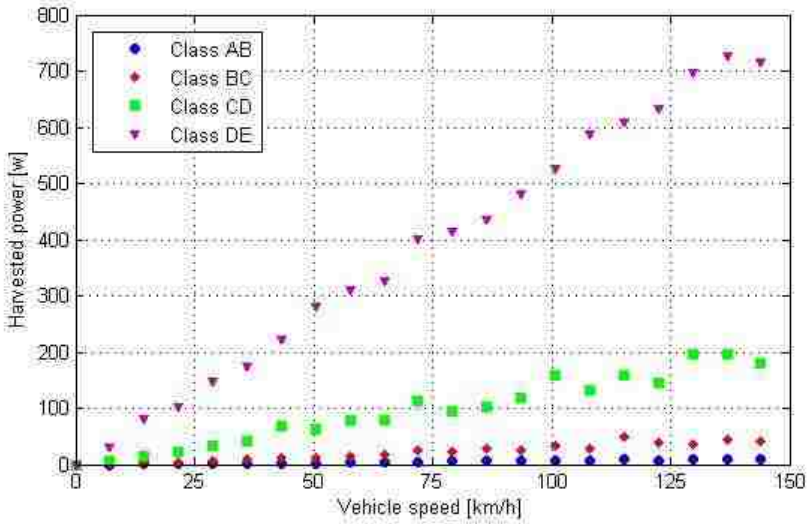

Figure 4.2-5: Harvested power as a function of vehicle speed for four classes of road roughness

The tire stiffness indeed strongly influences the harvestable power; as a matter of fact, the higher is it, the higher is the power that can be recovered [1].

According to the obtained outcomes in terms of harvested power, the CO_2 emission reduction can be computed for the three type of engine considered, as in the previous case in Section 4.1.6. The results of this calculation are reported in the tables below. It has to be noted that, in the case now taken into consideration, the savings obtained for a vehicle moving on a B-C class road also have relevant values. Moreover, considering 200 g/km as an average value of CO_2 emission for the class of vehicle under investigation, the emission reduction is in the order of 10% for the D-E road class.

Table 4.2-2: CO_2 savings for a gasoline engine equipped vehicle for the four classes considered

CO_2 emission reduction (4 dampers) – Gasoline engine				
Road class	**Min. value**	**Max. value**	**Average**	**Unit**
A-B	0.08	0.30	0.20	gCO_2/km
B-C	0.56	1.54	1.04	gCO_2/km
C-D	3.20	5.82	4.68	gCO_2/km
D-E	17.01	25.60	19.76	gCO_2/km

Table 4.2-3: CO_2 savings for a gasoline turbocharged engine equipped vehicle for the four classes considered

CO_2 emission reduction (4 dampers) – Gasoline turbocharged engine				
Road class	**Min. value**	**Max. value**	**Average**	**Unit**
A-B	0.09	0.31	0.21	gCO_2/km
B-C	0.59	1.63	1.10	gCO_2/km
C-D	3.39	6.18	4.96	gCO_2/km
D-E	18.04	27.15	20.96	gCO_2/km

Table 4.2-4: CO_2 savings for a diesel engine equipped vehicle for the four classes considered

CO_2 emission reduction (4 dampers) – Diesel engine				
Road class	**Min. value**	**Max. value**	**Average**	**Unit**
A-B	0.08	0.28	0.19	gCO_2/km
B-C	0.52	1.45	0.98	gCO_2/km
C-D	3.02	5.50	4.42	gCO_2/km
D-E	16.06	24.17	18.66	gCO_2/km

5 CONCLUSIONS AND RECOMMENDATIONS

5.1 Conclusions

In this thesis the model of a regenerative electromagnetic vehicle suspension, which can generate electric power from the road-induced vibrations, has been developed. The aim of the project is to provide a tool capable to predict the CO_2 emissions reduction and the dynamic performance of the suspension due to the on-vehicle installation of the analyzed system. For the first time, a complete assessment of the harvesting and ride filtering performances is provided. Moreover, the influence of vehicle speed and road roughness on the aforementioned outcomes is also investigated. Average parameters of two types of vehicle are taken into consideration for the simulations: a medium size passenger car and a SUV.

In particular, the shock absorber is composed of a permanent magnet brushless DC generator that is driven by a ball screw mechanism that converts the linear motion of the suspension into rotational motion. The generated electricity is then regulated by the proper power electronics and recharges the battery.

The model is entirely developed using Matlab in order to allow the maximum software flexibility. A quarter car model approach is used for the analysis as it is considered sufficient to guarantee the reliability of the results. The dynamic model of the electromagnetic shock absorber is integrated with the main suspension model. The model is intended to have as inputs random road profiles generated according to the classification proposed by the ISO 8608 Standard.

The simulations can provide an estimation of the CO_2 saving due to the power recovered and thus no longer requested from the engine. The evaluation is based on average value of efficiency of the alternator and of the engine. The results show that the amount of CO_2 not emitted expressed in g/km strongly depends on the road roughness but the vehicle speed does not have significant influence. Two different values of tire stiffness are considered, one for each application, but the influence of this parameter on the model outcomes is not investigated, as it is considered given for each car segment.

The results show that the application on a medium size passenger car of a suspension equipped with the proposed system allows a reduction of CO_2 emission of approximately 2.5 g/km on a C-D class road and 10.5 g/km on a D-E class road. This harvesting performance does not come without drawbacks: with respect to a conventional damper, the use of the proposed suspension introduces an average 14.4% decrease in ride comfort and an average 13.3% worsening of the road handling performance.

The simulations run to predict the CO_2 saving in a SUV application of the suspension show that the harvesting capability is almost doubled with respect to the previous case. In particular the emission of 19.8 g/km of CO_2 can be avoided considering a D-E class road. Moreover, the suspension in the current application features better ride filtering capabilities than in the previous one. The road handling index is calculated to be only 7.3% worse with respect to a conventional shock absorber and the ride comfort only 5.1% worse than the reference performance.

5.2 Recommendations

In order to improve the accuracy of the model and increase the reliability of the results, the modeling of the friction occurring in the ball screw mechanism could be performed to evaluate its influence on the dynamic behaviour of the apparatus.

In addition, an accurate analysis of the electrical charging circuit has to be added to this research in order to exactly define the efficiency of the system under the operating conditions imposed by the application.

An active control could be a feasible solution in order to enhance the dynamic performance of the system while exploiting the possibilities offered by the electromagnetic nature of the damper, which is more suitable for this type of application with respect to conventional hydraulic damping.

The construction of a prototype of the shock absorber might be the next step of the research in order to validate the results obtained by the simulation verifying the performance and the harvesting capability of the system. Moreover an estimation of the production cost of the electromagnetic regenerative shock absorber is fundamental in order to assess the performance-to-cost ratio of the system and thus its applicability on production vehicles.

6 APPENDICES

6.1 Appendix A

6.1.1 EoM input file

In this appendix, it is described how the single elements of the system are defined and assembled in the input file for the EoM code. They are assembled using a structured variable, named 'the_system', which contains a one dimensional cell array of items of predefined types. Each item is itself a structured variable with defined set of fields. The data structure of each item contains a field 'type', with a string that is the name of one of the item types defined (body, spring, link, rigid point, flex point, load, actuator, sensor, etc.). Several other fields must be included in the definition of an item, according to the type of item, and several optional fields may be added.

The 'body' type item is the main building block and it allows the user to add a rigid body to the system. All the other item types have to be attached to one or more rigid bodies. The other items, that can be both rigid and flexible connectors, may be divided in:

- Point connectors, whose geometry is defined at a single point (like 'rigid_point' and 'flex_point');
- Line connectors, which require two points to be defined (like 'link' and 'spring').

In order to apply loads, the 'actuator' type item is used. Every addition of an 'actuator' item to the system corresponds to the addition of a column in the input matrix u of the state space equations described in Section 3.3. The 'sensor' item types are used in order to measure displacements, velocities and accelerations, as it will be explained later on. The addition of a 'sensor' item corresponds to the addition of a row in the output matrix y, thus also in the sensor matrix C and in the feedthrough matrix D.

According to the guidelines that have been shown so far, the system described in Section 3.1 is built and the input file for the EoM code is assembled.

6.1.1.1 Definition of 'body' type item

In Figure 6.1-1 is shown an example of how a 'body' type item is defined, in particular the definition of the chassis is reported. The different fields needed for the definition of the element are reported:

- Item type: it is a string that specify the type of the item that it is going to be defined;
- Item name: it is a string that specify the name (that is required for 'body' type item and must be unique) of the element to be defined;
- Item mass: specify the mass of the element;
- Item moments of inertia: specify the xx, yy, and zz moments of inertia of the element;
- Item products of inertia: specify the xy, yz, and zx cross products of inertia of the element;
- Item location: specify the location of the center of mass of the element.

Then the element is added to the system.

```
item.type='body';
item.name='Chassis';
item.mass=450;
item.momentsofinertia=[1;1;1];
item.productsofinertia=[0;0;0];
item.location=[0.5;0;0.5];
the_system.item{end+1}=item;
the_system.item{end+1}=weight(item,g);
item={};
```

Figure 6.1-1: Example of the definition of a 'body' type item: chassis

Using the same procedure and the same fields, the other elements of the system are defined: upright, wheel and hub, lower A-arm, and upper A-arm.

6.1.1.2 Definition of 'spring' type item

The way in which the spring is defined is now explained and shown in Figure 6.1-2.

In addition to the fields previously used in the definition of the 'body' type item, in this case the location of the ends of the spring is added using the field 'item.location1' and 'item.location2' and the correspondent bodies to which the ends are attached are defined

('item.body1' and 'item.body2'). The name of the item is specified even if it is necessary only for 'body' type items. Additionally stiffness, damping, and inertia of the element are added using the proper fields. The preload, which is not specified in the definition of the item, is not assumed to be zero but it will be calculated from stiffness and statics.

```
item.type='spring';
item.name='Suspension spring';
item.location1=[0.5;0.6;0.7];
item.location2=[0.5;0.75;0.2];
item.body1='Chassis';
item.body2='Lower A-arm';
item.stiffness=42000;
item.damping=1000;
item.inertia=28.1;
the_system.item{end+1}=item;
item={};
```

Figure 6.1-2: Definition of the 'spring' type item

6.1.1.3 Definition of 'rigid_point' type item

For what concerns the connection between the defined bodies, it is done by rigid or flexible connections. In Figure 6.1-3, it is shown an example of how a rigid connection can be defined. The location and the names of the two bodies that are connected have to be specified. Moreover the properties to be defined include the number of forces that are carried and the number of moments. Acceptable choices for the number of forces and moments are 0, 1, 2, or 3. If there are either 1 or 2 forces or moments carried, a direction vector must be included; this is not necessary in the cases in which the forces or moments carried are 0 or 3. When 1 force or moment is carried, the direction axis of the force or moment has to be defined, while for 2 forces or moments (the case of 2 moments is shown in Figure 6.1-3), the axis defines the normal to the plane in which the forces or the moments lie.

```
item.type='rigid_point';
item.name='Wheel bearing';
item.body1='Wheel+hub';
item.body2='Upright';
item.location=[0.5;0.9;0.3];
item.forces=3;
item.moments=2;
item.axis=[0;1;0];
the_system.item{end+1}=item;
item={};
```

Figure 6.1-3: Examples of the definition of 'rigid_point' type item: wheel bearing

All the rigid connections of the system are defined according to the procedure just described. In Figure 6.1-8, they can be seen colored in yellow, ball shaped if they carry 3 forces and 0 moment and cylindrical shaped in the case in which one axis is defined due to the previously mentioned guidelines (the defined axis corresponds with the cylinder axis).

6.1.1.4 Definition of 'flex_point' type item

The tire-ground contact is modeled using 'flex_point' type item, as shown in the example in Figure 6.1-4. It is basically a flexible version of the rigid point already described, with the possibility to add the stiffness (also torsional, zero in the shown example) and its direction.

```
item.type='flex_point';
item.name='Tire, vertical';
item.body1='Wheel+hub';
item.body2='ground';
item.location=[0.5;0.9;0];
item.forces=1;
item.moments=0;
item.stiffness=[150000;0];
item.axis=[0;0;1];
item.rolling_axis=[0;1;0];
the_system.item{end+1}=item;
item={};
```

Figure 6.1-4: Example of the definition of 'flex_point' type item: tire

6.1.1.5 Definition of 'actuator' type item

In order to insert the input forces that act on the system, two actuators are defined:

- One that represents the force acting on the tire due to the changing in the road profile (shown in Figure 6.1-5);
- One that represents the force exerted by the shock absorber on the two points where it is attached to the chassis and the lower arm respectively.

It is similar to the 'spring' item, but the force is determined from an input; as the 'spring' item the locations of the two ends of the actuator and the names of the two bodies to which it is attached are defined. Additionally, the field 'gain' is present, that represents the ratio of force to input value. By so doing, for the case of the wheel actuator shown in Figure 6.1-5, it is possible to convert the vertical displacement of the road profile into a force acting vertically on the tire.

```
item.type='actuator';
item.name='wheel actuator';
item.location1=[0.5;0.9;0];
item.location2=[0.5;0.9;-0.1];
item.body1='Wheel+hub';
item.body2='ground';
item.gain=150000;
item.travel=0;
the_system.item{end+1}=item;
item={};
```

Figure 6.1-5: Example of the definition of 'actuator' type item: wheel actuator

6.1.1.6 Definition of 'sensor' type item

The sensors allow the user to obtain the data needed as output. Several sensors are defined in order to have the following outputs:

- Relative displacement between the two ends of the shock absorber;
- Relative velocity between the two ends of the shock absorber;
- Vertical displacement between the center of mass of the chassis and the ground;
- Vertical acceleration between the center of mass of the chassis and the ground;
- Vertical displacement between the center of the wheel hub and the road profile.

In Figure 6.1-6 it is shown how a sensor is defined, in particular the one that allows to obtain the relative displacement between the chassis and the ground. Properties include location and name of the two bodies to which the sensor is attached. The field 'order' specifies the type of output desired: 1 for displacement (as in Figure 6.1-6), 2 for velocity, 3 for acceleration.

```
item.type='sensor';
item.order=1;
item.name='body sensor';
item.location1=[0.5;0;0.5];
item.location2=[0.5;0;0];
item.body1='Chassis';
item.body2='ground';
the_system.item{end+1}=item;
item={};
```

Figure 6.1-6: Example of the definition of 'sensor' type item: body sensor

```
item.type='sensor';
item.order=1;
item.name='tire sensor';
item.location1=[0.5;0.9;0.3];
item.location2=[0.5;0.9;0];
item.body1='Wheel+hub';
item.body2='ground';
item.actuator='wheel actuator';
item.gain=150000;
the_system.item{end+1}=item;
item={};
```

Figure 6.1-7: Definition of the sensor to measure the dynamic force between the tire and the ground

The system build with the procedure explained in this section is shown in Figure 6.1-8.

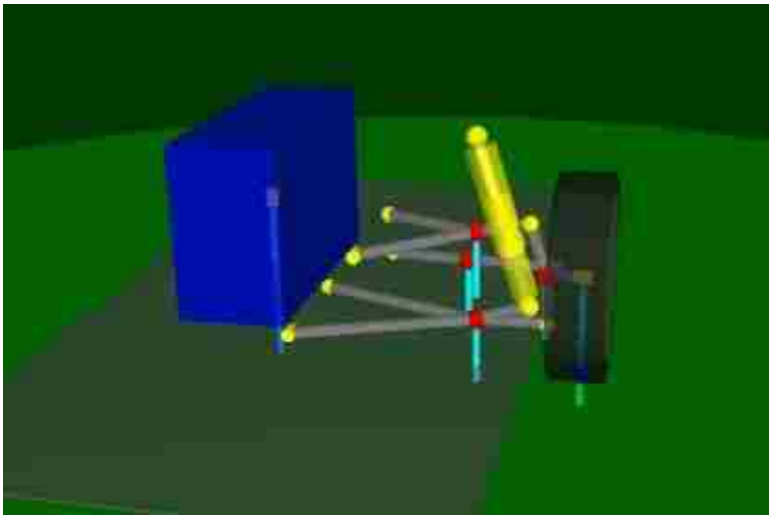

Figure 6.1-8: Complete model of the suspension in EoM

6.2 Appendix B

6.2.1 Road handling index and ride comfort

In this appendix, the plots of the road handling index obtained considering the SUV application of the electromagnetic damper compared with the same quantities computed considering a conventional linear damper (with a constant damping coefficient 5000 Ns/m) are shown. The same comparison is shown for the values of the sprung mass weighted acceleration.

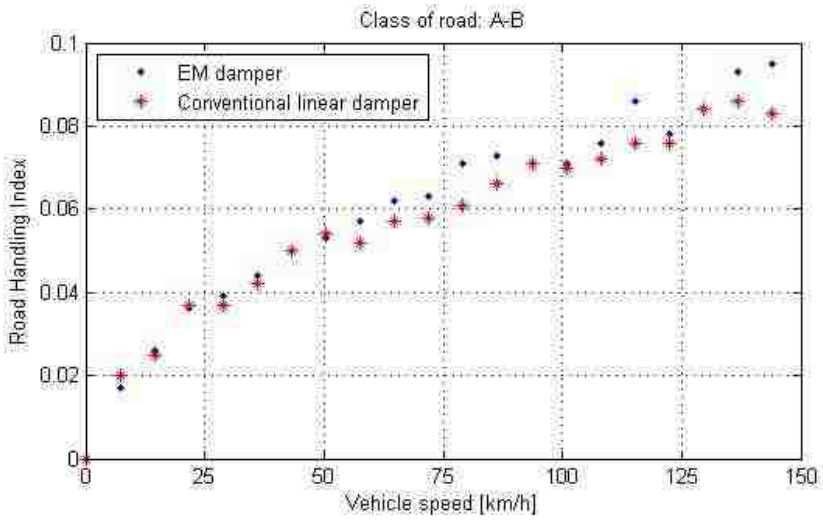

Figure 6.2-1: Road handling index as a function of vehicle speed for A-B class road: comparison between the values obtained with the electromagnetic damper and a conventional one (5000 Ns/m)

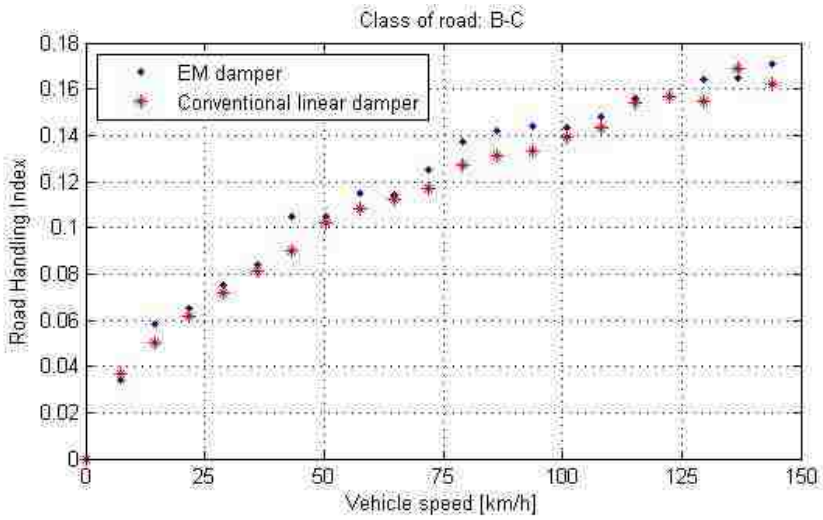

Figure 6.2-2: Road handling index as a function of vehicle speed for B-C class road: comparison between the values obtained with the electromagnetic damper and a conventional one (5000 Ns/m)

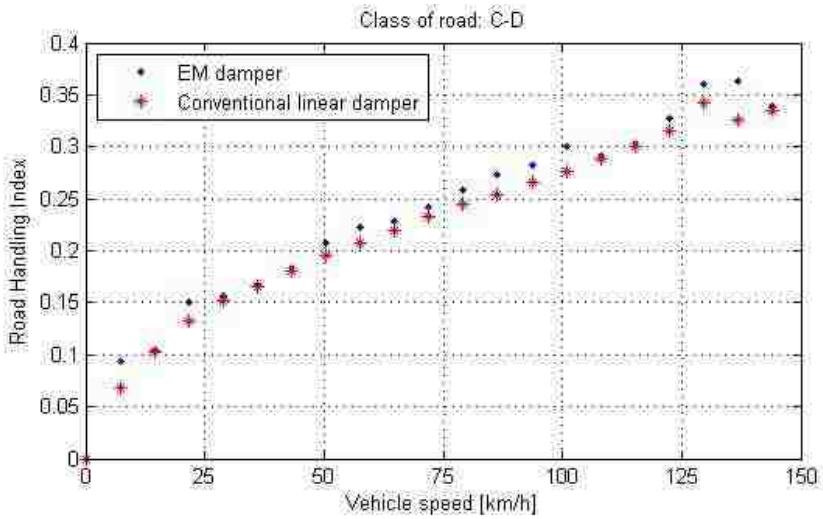

Figure 6.2-3: Road handling index as a function of vehicle speed for C-D class road: comparison between the values obtained with the electromagnetic damper and a conventional one (5000 Ns/m)

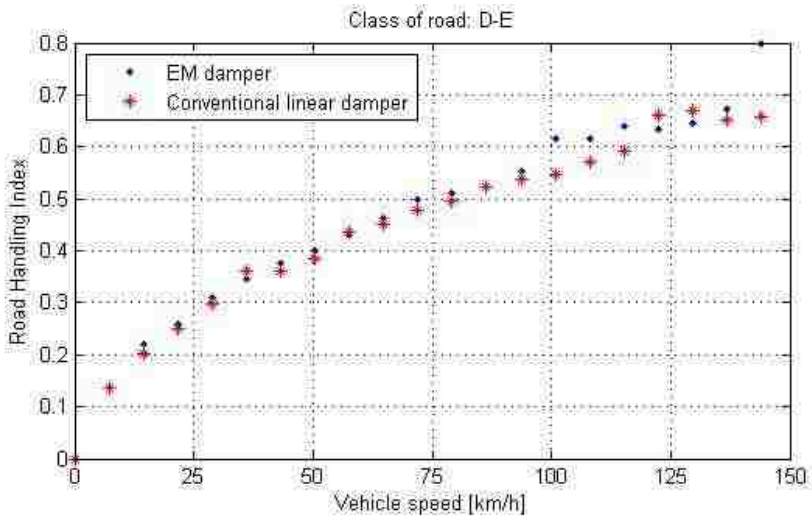

Figure 6.2-4: Road handling index as a function of vehicle speed for D-E class road: comparison between the values obtained with the electromagnetic damper and a conventional one (5000 Ns/m)

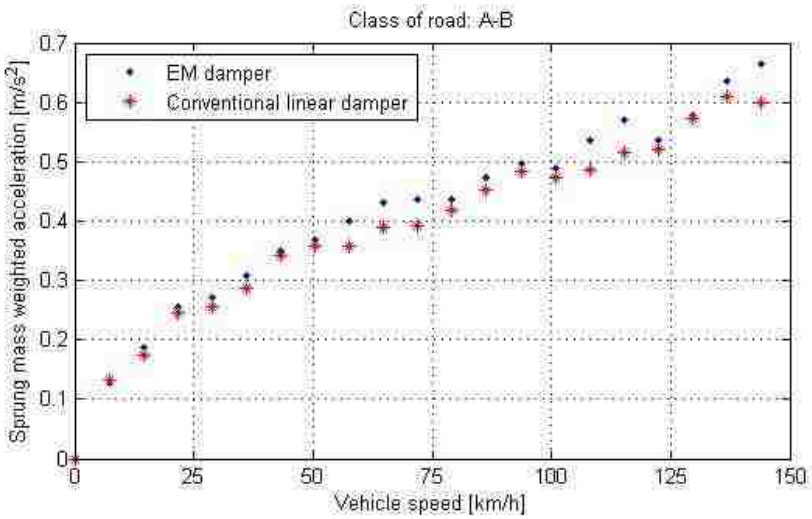

Figure 6.2-5: Sprung masses weighted acceleration as a function of vehicle speed for A-B class road: comparison between the values obtained with the electromagnetic damper and a conventional one (5000 Ns/m)

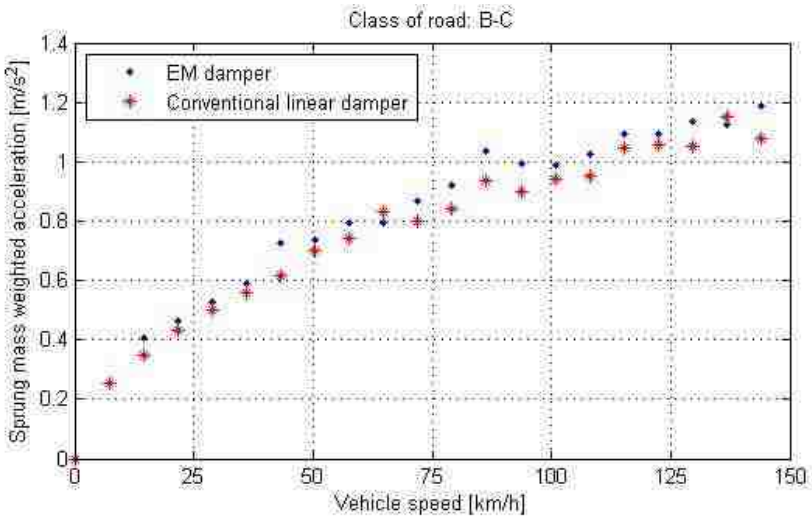

Figure 6.2-6: Sprung masses weighted acceleration as a function of vehicle speed for B-C class road: comparison between the values obtained with the electromagnetic damper and a conventional one (5000 Ns/m)

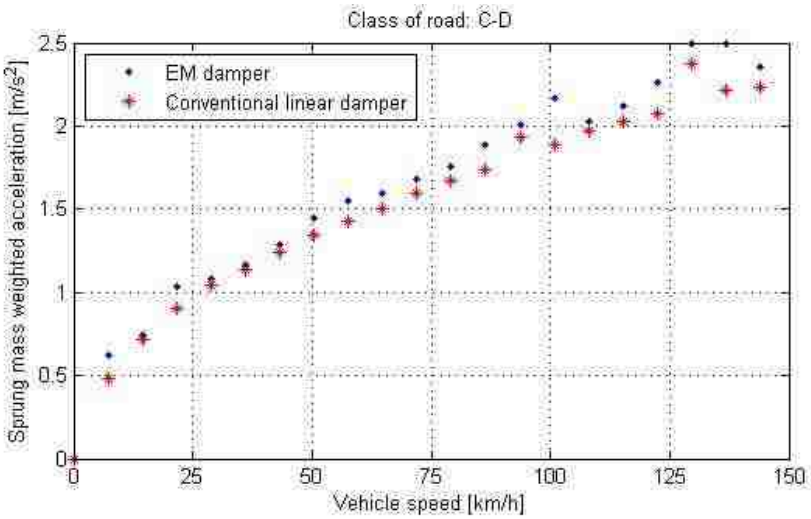

Figure 6.2-7: Sprung masses weighted acceleration as a function of vehicle speed for C-D class road: comparison between the values obtained with the electromagnetic damper and a conventional one (5000 Ns/m)

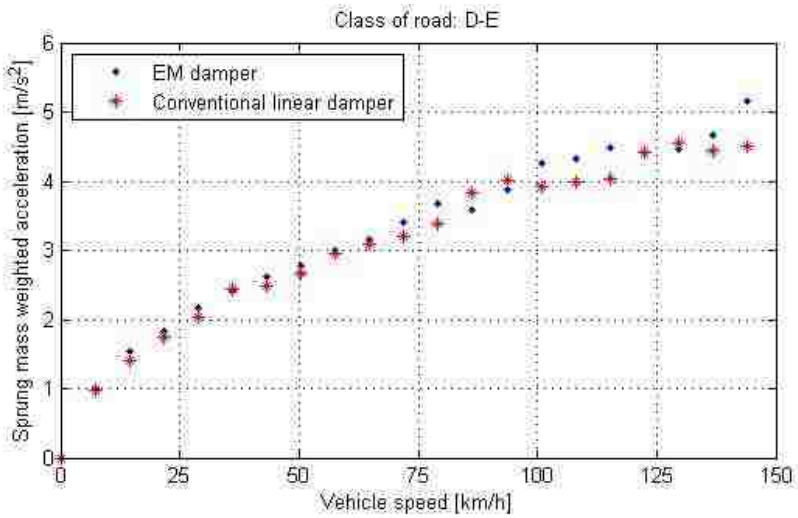

Figure 6.2-8: Sprung masses weighted acceleration as a function of vehicle speed for D-E class road: comparison between the values obtained with the electromagnetic damper and a conventional one (5000 Ns/m)

REFERENCES

[1] L. Zuo and P. Zhang, "Energy Harvesting, Ride Comfort, and Road Handling of Regenerative Vehicle Suspension," *Journal of Vibration and Acoustics*, vol. 135, 2013.

[2] N. Amati, A. Festini and A. Tonoli, "Design of electromagnetic shock ansorber for automotive suspensions," *Vehicle System Dynamics*, pp. 1913-1928, 2011.

[3] G. Genta and L. Morello, The Automotive Chassis: Volume 2: Components Design, Berlin: Springer, 2009.

[4] O. D. Paz, "Design and Performance of Electric Shock Absorbers," Master Thesis, Lousiana State University, Baton Rouge, Louisiana, 2004.

[5] J. Reimpell, H. Stoll and J. W. Betzler, The Automotive Chassis: Engineering Principles, Second Edition, Butterworth-Heinemann, 2001.

[6] K. Huang, F. Yu and Y. Zhang, "Active controller design for an electromagnetic energy-regenerative suspension," *International Journal of Automotive Technology*, vol. 12, pp. 877-885, 2011.

[7] Greco, Ippolito, Nepote, van Grootveld and Martini, "Kinetic energy to electric energy conversion using shock absorbers," Monograph, 2013.

[8] L. Zuo, B. Scully, J. Shestani and Y. Zhou, "Design and characterization of an electromagnetic energy harvester for vehicle suspensions," *Smart Materials and Structures*, 2010.

[9] A. Tonoli, N. Amati, J. G. Dentoni, R. Galluzzi and E. Gasparin, "Modelling and validation of electromechanical shock absorbes," *Vehicle System Dynamics*, vol. 51, pp. 1186-1199, 2013.

[10] A. Gupta, A. J. Jendrzejczyk, M. Mulcahy and J. Hull, "Design of electromagnetic shock absorbers," *Int. J. Mech. Mater. Design*, vol. 3, pp. 285-291, 2006.

[11] X. Lin, Y. Bo, G. Xuexun and Y. Jun, "Simulation and Performance Evaluation of Hydraulic Transmission Electromagnetic Energy-regenerative Active Suspension,"

in *Second WRI Global Congress on Intelligent Systems,* 2010.

[12] S. Avadhany, P. Abel, V. Tarasov and Z. Anderson, "Regenerative shock absorber". Patent US 8376100 B2, 19 February 2013.

[13] C. Tucker, R. Wendell, Z. Anderson, E. Moen, J. Schneider, Z. Jackowski and S. Morton, "Integrated energy generating damper". Patent US 20130147205 A1, 13 January 2013.

[14] Y. Zhang, X. Zhang, M. Zhan, K. Guo, F. Zhao and Z. Liu, "Study of a novel hydraulic pumping regenerative suspension for vehicles," *Journal of the Franklin Institute,* 2014.

[15] G. Zhang, J. Cao and F. Yu, "Design of active and energy-regenerative controllers for DC-motor-based suspension," *Mechatronics*, pp. 1124-1134, 2012.

[16] Z. Li, L. Zuo, G. Luhrs, L. Lin and Y. Qin, "Electromagnetic Energy-Harvesting Shock Absorbers: Design, Modeling, and Road Tests," *IEEE Transaction on Vehicular Technology,* vol. 62, pp. 1065-1073, 2013.

[17] Z. Li, L. Zuo, J. Kuang and G. Luhrs, "Energy-harvesting shock absorber with a mechanical motion rectifier," *Smart Materials and Structures,* 2012.

[18] Z. Li, Z. Brindak and L. Zuo, "Modeling of an electromagnetic vibration energy harvester with motion magnification," in *Proc. ASME Int. Mech. Eng. Congr.* , Devner, 2011.

[19] Y. Zhang, K. Huang, F. Yu, Y. Gu and D. Li, "Experimental Verification of Energy-regenerative Feasibility for an Automotive Electrical Suspension System," *IEEE,* 2007.

[20] N. Mohan, Electric Drives, Minneapolis: Mnpere, 2003.

[21] E. Mendrela, M. Lukaniszyn and K. Macek-Kaminsta, "Dis-Type Brushless DC Motors," *Polish Academy of Science,* 2002.

[22] J. Gieras and Z. Piech, Linear Synchronous Motors, CRC Press, 1999.

[23] P. Sen, Principles of electric machines and power electronics, John Wiley & Sons, 1989.

[24] A. Tonoli, "Dynamic characteristics of eddy current dampers and couplers," *Journal*

of Sound and Vibration, pp. 576-591, 2007.

[25] D. Karnopp, "Permanent magnets linear motors used as variable mechanical dampersfor vehicle suspensions," *Vehicle System Dynamics,* pp. 187-200, 1989.

[26] N. Amati, A. Canova, F. Cavalli, S. Carabelli, A. Festini and A. Tonoli, "Electromagnetic shock absorbers for automotive suspensions: electromechanical design," in *Proceedings of the ASME-ESDA2006 Conference,* Torino, IT, 2006.

[27] J. Lundstrom, *Road roughness estimation using available vehicle sensors,* 2009.

[28] C. Dodds and J. Robson, "The description of road surface roughness," *Journal of Sound and Vibration,* pp. 175-183, 1973.

[29] M. Agostinacchio, D. Ciampa and S. Olita, "The vibrations induced by surface irregularities in road pavements - a Matlab approach," *Eur. Transp. Res. Rev.,* 2013.

[30] F. Tyan, Y. Hong, S. Tu and W. Jeng, "Generation of Random Road Profiles," *Journal of Advanced Engineering* , vol. 4, pp. 151-156, 2009.

[31] S. Park, A. Popov and D. Cole, "Influence of soil deformation on off-road heavy vehicle suspension vibration," *J Terramech,* pp. 41-68, 2004.

[32] T. Kenjo and S. Nagamori, Permanent-Magnet and Brushless DC Motors, Oxford: Clarendon Press, 1985.

[33] P. S. Crovetti, *Electric and electronic systems in vehicle, course material,* Turin: Politecnico di Torino, 2014.

[34] E. Lefeuvre, D. Audigier, C. Richard and D. Guyomar, "Buck-Boost Converter for Sensorless Power Optimization of Piezoelectric Energy Harvester," *IEEE Transaction on Power Electronics,* vol. 22, pp. 2018-2025, 2007.

[35] P. Li, C. Zhang, J. Kim, L. Yu and L. Zuo, "Buck-boost Converter for Simultaneous Semi-active Vibration Control and Energy Harvesting for Electromagnetic Regenerative Shock Absorber," *Active and Passive Smart Structures and Integrated Systems,* vol. 9057, 2014.

[36] X. Tang and L. Zuo, "Simultaneous energy harvesting and vibration control of structures with tuned mass dampers," *Journal of Intelligent Material Systems and Structures,* vol. 23, pp. 2117-2127, 2012.

[37] *Ball & acme lead screw technical information,* Stock Drive Products/Sterling Instrument, New York.

[38] *Technical Guidelines for the preparation of applications for the approval of innovative technologies pursuant to Regulation (EC) No 443/2009 of the European Parliament and of the Council,* February 2013.

[39] A. Gimeno and G. Friedrich, "Application of the VDA standard for the comparison and losses reduction of high efficiency car alternators," *IEEE*, pp. 547-553, 2008.

[40] M. J. Johnston, *Development and Evaluation of Vehicle Suspension Tuning Metrics,* Master Thesis, University of Windsor, Canada, 2010.

[41] L. Zuo and S. Nayfeh, "Low order continuous-time filters for approximation of the ISO 2631-1 human vibration sensitivity weightings," *Journal of Sound and Vibration*, pp. 459-465, 2003.

VITA AUCTORIS

NAME:	Fabio Tarantini
PLACE OF BIRTH:	San Pietro Vernotico, Italy
YEAR OF BIRTH:	1991
EDUCATION:	Politecnico di Torino, B.Sc in Automotive Engineering, Torino, Italy, 2013
	Politecnico di Torino, Master in Automotive Engineering, Torino, Italy, 2015
	University of Windsor, M.A.Sc. in Mechanical Engineering, Windsor, ON, 2015